UNIVERSITY OF CALIFORNIA SAN DIEGO

Computational Methodologies for Cardiac Signal Applications: Arrhythmia Classification, Biometric Identification, and Blood Pressure Estimation

A dissertation submitted in partial satisfaction of the
requirements for the degree
Doctor of Philosophy

in

Computer Science

by

Po-Ya Hsu

Committee in charge:

Professor Chung-Kuan Cheng, Chair
Professor Garrison W. Cottrell
Professor Tzyy-Ping Jung
Professor Darren John Lipomi
Professor Steven James Swanson

2021

The dissertation of Po-Ya Hsu is approved, and it is acceptable in quality and form for publication on microfilm and electronically.

University of California San Diego

2021

DEDICATION

To my family.

TABLE OF CONTENTS

LIST OF FIGURES

LIST OF TABLES

ACKNOWLEDGEMENTS

First, I like to thank my advisor, Professor Cheng, for his sincere advice throughout my whole Ph.D. study, as well as the opportunities to collaborate with top-notch researchers. I would also like to express my appreciation to the Cheng family for their supports.

My sincere thanks also go to my thesis committee members Professor Garrison Cottrell, Professor Steven Swanson, Professor Tzyy-Ping Jung, and Professor Darren Lipomi for their time, encouragement and insightful comments.

I like to express my special appreciation to Instructor Martha Stacklin, Professor Lawrence Saul, and Professor Mia Minnes, who tutored me for language and improved my paper writing skills. Their supports and life wisdom are also tremendously helpful.

To whoever is reading this dissertation, I would like to thank you for your time, and I sincerely hope that you enjoy reading this dissertation!

Finally, I appreciate the consistent supports from my family. I also appreciate all the supports from other family members and my friends.

The material in this dissertation is based on the following publications.

Chapter 2, in part, contains reprints of P.-Y. Hsu, P.-H. Hsu, H.-L. Liu, C.-T. Lin, H.-T. Chou, Y.-F. Tseng, and T.-H. Lee, "Star-ECG: Visualization of Electrocardiograms for Arrhythmia and Heart Rate Variability", *Annual International Conference of the IEEE Engineering in Medicine and Biology Society (EMBC)*, 2021; P.-Y. Hsu, P.-H. Hsu, T.-H. Lee, and H.-L. Liu, "Heart Rate and Respiratory Rate Monitoring Using Seismocardiography", *Annual International Conference of the IEEE Engineering in Medicine and Biology Society (EMBC)*, 2021; and P.-Y. Hsu, and C.-K. Cheng, "R-peak Detection Using a Hybrid of Gaussian and Threshold Sensitivity", *Annual International Conference of the IEEE Engineering in Medicine and Biology Society (EMBC)*, 2020. The dissertation author was the primary

researcher and author of these papers.

Chapter 3, in part, contains reprints of P.-Y. Hsu, P.-H. Hsu, H.-L. Liu, C.-T. Lin, H.-T. Chou, Y.-F. Tseng, and T.-H. Lee, "Star-ECG: Visualization of Electrocardiograms for Arrhythmia and Heart Rate Variability", *Annual International Conference of the IEEE Engineering in Medicine and Biology Society (EMBC)*, 2021; P.-Y. Hsu, P.-H. Hsu, T.-H. Lee, and H.-L. Liu, "Multi-label Arrhythmia Classification From 12-Lead Electrocardiograms", *IEEE Computing In Cardiology Conference*, 2020; and P.-Y. Hsu and C.-K. Cheng, "Arrhythmia classification using deep learning and machine learning with features extracted from waveform-based signal processing", *Annual International Conference of the IEEE Engineering in Medicine and Biology Society (EMBC)*, 2020. The dissertation author was the primary researcher and author of these papers.

Chapter 4, in part, contains reprints of P.-Y. Hsu, P.-H. Hsu, T.-H. Lee, and H.-L. Liu, "Motion Artifact Resilient SCG-based Biometric Authentication Using Machine Learning", *Annual International Conference of the IEEE Engineering in Medicine and Biology Society (EMBC)*, 2021; P.-Y. Hsu, P.-H. Hsu, and H.-L. Liu, "Exploring Seismocardiogram Biometrics with Wavelet Transform", *IEEE International Conference on Pattern Recognition*, 2021; and P.-Y. Hsu, P.-H. Hsu, and H.-L. Liu, "Fold Electrocardiogram Into a Fingerprint.", *Proc. IEEE/CVF Conference on Computer Vision and Pattern Recognition Workshops*, 2020. The dissertation author was the primary researcher and author of these papers.

Chapter 5, in part, contains a reprint of P.-Y. Hsu, P.-H. Hsu, H.-L. Liu, K.-Y. Lin, and T.-H. Lee, "Motion Artifact Resilient Cuff-Less Blood Pressure Monitoring Using a Fusion of Multi-Dimensional Seismocardiograms", *Annual International Conference of the IEEE Engineering in Medicine and Biology Society (EMBC)*, 2021. The dissertation author was the primary researcher and author of these papers.

My co-authors (Professor Chung-Kuan Cheng, Mr. Po-Han Hsu, Mr. Tsung-Han Lee, Professor

Chi-Te Lin, Professor Kuan-Yu Lin, Professor Hsin-Li Liu, and Ms. Yu-Fang Tseng, listed in alphabetical order) have all kindly approved the inclusion of the aforementioned publications in my dissertation.

VITA

2016	B.S., Electrical Engineering, National Taiwan University, Taipei, Taiwan
2019	M.S., Computer Science, University of California San Diego
2021	Ph.D., Computer Science, University of California San Diego

Papers titled "Cuff-Less Blood Pressure Monitoring with a 3-Axis Accelerometer" and "Empirical study on sufficient numbers of minimum cuts in strongly connected directed random graphs" have authors listed in alphabetical order.

(*) stands for the corresponding author. (+) stands for the co-first author.

- **P.-Y. Hsu***, P.-H. Hsu, H.-L. Liu, K.-Y. Lin, and T.-H. Lee, "Motion Artifact Resilient Cuff-Less Blood Pressure Monitoring Using a Fusion of Multi-Dimensional Seismocardiograms", *Annual International Conference of the IEEE Engineering in Medicine and Biology Society (EMBC)*, 2021. [*in press*]

- **P.-Y. Hsu***, P.-H. Hsu, H.-L. Liu, C.-T. Lin, H.-T. Chou, Y.-F. Tseng, and T.-H. Lee, "Star-ECG: Visualization of Electrocardiograms for Arrhythmia and Heart Rate Variability", *Annual International Conference of the IEEE Engineering in Medicine and Biology Society (EMBC)*, 2021. [*in press*]

- **P.-Y. Hsu**, P.-H. Hsu, T.-H. Lee, and H.-L. Liu*, "Motion Artifact Resilient SCG-based Biometric Authentication Using Machine Learning", *Annual International Conference of the IEEE Engineering in Medicine and Biology Society (EMBC)*, 2021. [*in press*]

- **P.-Y. Hsu**, P.-H. Hsu, T.-H. Lee, and H.-L. Liu*, "Heart Rate and Respiratory Rate Monitoring Using Seismocardiography", *Annual International Conference of the IEEE Engineering in Medicine*

and Biology Society (EMBC), 2021. [*in press, contribution to combating the COVID-19*]

- D. L. Harrington, **P.-Y. Hsu**$^{+}$, R. J. Theilmann, A. Angeles-Quinto, A. Robb-Swan, S. Nichols, T. Song, L. Le, C. Rimmele, S. Matthews, K. A. Yurgil, A. Drake, Z. Ji, J. Guo, C.-K. Cheng, R. R. Lee, D. G. Baker, M. Huang*, "Detection of Chronic Blast-related Mild Traumatic Brain Injury with Diffusion Tensor Imaging and Support Vector Machines"[*under submission*]

- B. Polat, L. L. Becerra, **P.-Y. Hsu**, V. Kaipu, P. P. Mercier, C.-K. Cheng, and D. J. Lipomi*, "Epidermal Graphene Sensors and Machine Learning for Estimating Swallowed Volume", *ACS Applied Nano Materials* 4, no. 8 (2021): 8126-8134. [*Editor's Choice*]

- **P.-Y. Hsu***, P.-H. Hsu, and H.-L. Liu, "Exploring Seismocardiogram Biometrics with Wavelet Transform", *IEEE International Conference on Pattern Recognition*, 2021, pp. 4450-4457.

- **P.-Y. Hsu***, P.-H. Hsu, T.-H. Lee, and H.-L. Liu, "Multi-label Arrhythmia Classification From 12-Lead Electrocardiograms", *IEEE Computing In Cardiology Conference*, 2020, pp. 1-4. [*challenge rank 16 / 217*]

- **P.-Y. Hsu**, K.-Y. Lin, P.-H. Hsu, W.-F. Kao, Y.-C. Hsu, and H.-L. Liu*, "Prediction of acute kidney injury during the prerace stage of a 48-hour ultramarathon", *Translational Sports Medicine*, vol. 6, 2020, pp. 599-606.

- **P.-Y. Hsu***, P.-H. Hsu, and H.-L. Liu, "Fold Electrocardiogram Into a Fingerprint", *Proc. IEEE/CVF Conference on Computer Vision and Pattern Recognition Workshops*, 2020, pp. 828-829.

- **P.-Y. Hsu*** and C.-K. Cheng, "Arrhythmia classification using deep learning and machine learning with features extracted from waveform-based signal processing", *Annual International Conference of the IEEE Engineering in Medicine and Biology Society (EMBC)*, 2020, pp. 292-295.

- **P.-Y. Hsu**[*] and C.-K. Cheng, "R-peak Detection Using a Hybrid of Gaussian and Threshold Sensitivity", *Annual International Conference of the IEEE Engineering in Medicine and Biology Society (EMBC)*, 2020, pp. 4470-4474.

- E. Chang, C.-K. Cheng[*], A. Gupta, **P.-Y. Hsu**, A. Moffitt, A. Ren, I. Tsaur, and S. Wang, "Empirical study on sufficient numbers of minimum cuts in strongly connected directed random graphs", *Networks*, vol. 76, 2020, pp. 106-121.

- **P.-Y. Hsu**[*], and C. Holtz, "A Comparison of Machine Learning Tools for Early Prediction of Sepsis from ICU Data", *IEEE Computing In Cardiology Conference*, 2020, pp. 1-4.

- E. Chang, C.-K. Cheng[*], A. Gupta, P.-H. Hsu[*], **P.-Y. Hsu** [*+], H.-L. Liu, A. Moffitt, A. Ren, I. Tsaur, and S. Wang, "Cuff-Less Blood Pressure Monitoring with a 3-Axis Accelerometer", *Annual International Conference of the IEEE Engineering in Medicine and Biology Society (EMBC)*, 2019, pp. 6834-6837. [*UC San Diego 2019 CSE Open House Unicorn Award*]

- **P.-Y. Hsu**[*], C.-H. Yao[*], Y. Wang, and C.-K. Cheng[*], "Adaptive sensitivity analysis with nonlinear power load modeling", *Proc. ACM/IEEE International Workshop on System-Level Interconnect Prediction*, 2018, pp. 1-6.

ABSTRACT OF THE DISSERTATION

Computational Methodologies for Cardiac Signal Applications: Arrhythmia Classification, Biometric Identification, and Blood Pressure Estimation

by

Po-Ya Hsu

Doctor of Philosophy in Computer Science

University of California San Diego, 2021

Professor Chung-Kuan Cheng, Chair

Cardiovascular diseases have been the leading cause of death over the world for the last two decades. In the United States, the cost for heart diseases is around $363 billion from year *2016* to *2017*, including the consumption from health care services, medicines, and lost productivity due to death. To prevent heart diseases and further deterioration, real-time cardiovascular monitoring and early detection of abnormal cardiac activities are critical. With the advance of wearable sensor technology and maturity of machine learning models, researchers have gradually adopted such techniques in a great number of computing cardiology problems. This dissertation aims to continue the success through advancing

signal processing techniques for wearable sensors and devising machine learning methods motivated by applications to cardiovascular problems.

To this end, we provide computational methodologies for heartbeat detection and three relevant applications: arrhythmia classification, biometric identification, and blood pressure estimation. Heartbeat detection is the primary step to complete the three aforementioned and a majority of cardiac signal applications; therefore, high quality heartbeat detection algorithm is required for promising outcome. Successful automated arrhythmia classification program can achieve early diagnosis of heart diseases and reduce the manual arrhythmia labeling workload. Cardiology-based biometric has attracted attention in the last few years due to its great privacy preserving property and cardiac activity indicator. Portable blood pressure monitor can substantially improve the healthcare environment since blood pressure is able to infer the cardiovascular functioning.

We organized this dissertation as follows. First, we exhibit high quality heartbeat detection algorithms for normal electrocardiograms (ECG), abnormal ECG, and seismocardiograms (SCG). In addition, we present *Star-ECG*, a ECG visualization tool for non-experts to easily identify heartbeats and compute heart rate variability. Next, we present competitive computer-aided arrhythmia diagnosis programs for both one-channel and 12-lead ECG. Subsequently, we demonstrate ECG and SCG biometric authentication models. Finally, we provide a wearable blood pressure monitoring approach that is capable of capturing a person's blood pressure during normal walking motion.

Chapter 1

Introduction

Cardiovascular disease has been the leading cause of death over the world for the last two decades. In the United States, the cost for heart diseases is around $363 billion from year *2016* to *2017*, including the consumption from health care services, medicines, and lost productivity due to death. To prevent heart diseases, both real-time cardiovascular monitoring and early detection of abnormal cardiac activities are critical. With the advance of wearable sensor technology and maturity of machine learning models, researchers have gradually adopted such techniques in a great number of computing cardiology problems. However, several proposed solutions hinder the cardiologists from adopting the artificial intelligence models, and the main reason lies in the lack of physiology interpretation from the proposed models.

This dissertation proposes potential solutions to the challenges through building physiologically reasonable computational models motivated by applications to cardiovascular problems. We discuss the computational methodologies for heartbeat detection and three relevant applications: arrhythmia classification, biometric identification, and blood pressure estimation. In Chapter 2, we visit the heartbeat detection challenges and provide our solutions for normal and abnormal electrocardiograms and seis-

mocardiograms. In Chapter 3, we discuss the arrhythmia classification challenges and demonstrate our arrhythmia classification algorithms that have been tested on seven open datasets with data collected from over 40,000 patients. In Chapter 4, we explore the cardiac signal-based biometric challenges and present our electrocardiogram-based and seismocardiogram-based authentication models, which have been verified on both the open and our own datasets. In Chapter 5, we investigate the blood pressure estimation challenges and present our solution to real-time motion artifact resilient cuff-less blood pressure monitoring.

1.1 Emerging Heartbeat Detection Challenges

Heartbeat detection is the primary step in various cardiovascular problems [41]. Therefore, sufficiently high sensitivity heartbeat detection algorithms are necessary. When the motion artifact is large or the sensor contact is loose, heartbeat detection becomes challenging due to the corrupted signal and low signal-to-noise ratio (SNR) [7] [55]. For electrocardiograms (ECG), which is a continuous measure of electrical depolarization and repolarization throughout cardiac activities, researchers target at positioning the R-peaks during heartbeat detection, and multiple methods have been proposed by the researchers [19] [22] [23] [33] [83]. The most popular ECG R-peak detection algorithm goes to the Pan-Tompkins algorithm, which searches R-peaks in a threshold-based fashion [83]. For seismocardiograms (SCG), which is a continuous measure of mechanical motion induced by the beating heart, few studies have reported leveraging SCG for heartbeat detection due to the large motion artifact and unusually low SNR in SCG [102] [106].

This dissertation focuses on detecting heartbeats in low SNR cardiac signals. In Chapter 2, we discuss such challenges and propose solutions to both ECG from the arrhythmia patients and SCG from the healthy people.

1.2 Emerging Arrhythmia Diagnosis Challenges

Arrhythmia is a serious cardiovascular disease, and early diagnosis of arrhythmia can substantially improve the healthcare environment due to its high prevalence and associated high mortality [9]. In this end, ECG arises as a great arrhythmia diagnostic tool, given that ECG is non-invasive and easily accessible. Numerous ECG arrhythmia classification programs have thus been proposed to reduce manual labeling workload, but most rely on hand-crafted feature extraction or deep learning-based approaches lacking physiology interpretability [2] [25] [76] [113] [115].

This dissertation aims at developing fully automated ECG arrhythmia diagnosis programs that incorporate physiological reasoning. We propose the algorithms for single lead and 12-lead ECG arrhythmia classification in Chapter 3. Both algorithms have been tested on open datasets, and our 12-lead ECG arrhythmia classification algorithm was ranked top 7% (16/217) in the global *2020 Computing in Cardiology Competition*.

1.3 Emerging Cardiac Signal-Based Biometric Identification Challenges

Today, biometric systems have been largely applied to human identity verification for high level security. Some well-known biometrics are human face, fingerprint, and iris. The technique of characterizing these biometrics has become mature and commonly seen in our daily life [63]. However, these external biometrics are susceptible to spoofing attacks [47] [119]. For instance, fingerprints can be left on an object and facial recognition can be hacked by high-resolution photos. To circumvent the privacy issue of external biometrics, ECG biometrics have been increasingly studied in recent years [15] [18] [47] [78] [111]. Nevertheless, making cardiac signals a reliable biometric remains challenging because of data availability and noisy data [87].

This dissertation focuses on leveraging ECG and SCG as biometrics. In Chapter 4, we propose solutions to both ECG and SCG biometric identification systems. The ECG data is from the open dataset, and the SCG is from both the open dataset and our self-collected one.

1.4 Emerging Continuous Blood Pressure Monitoring Challenges

Blood pressure (BP) can indicate a person's cardiovascular health status, and real-time BP monitoring is highly required in people with hypertension or hypotension or other cardiovascular disease [5]. Nowadays, frequently adopted BP monitoring methods rely on the usage of an inflatable cuff and the person staying still during measurements, which indicates the need of improvements in the techniques [8] [52] [86]. Some cuff-less strategies have been proposed, for example, ballistocardiograms are leveraged to estimate BP in Chang's and Kim's teams [20] [60]. Pulse transit time together with ECG are adopted to compute BP in Poon's and Zheng's teams [88] [120]. Unfortunately, all the aforementioned cuff-less BP monitoring methods are prone to motion artifacts.

This dissertation proposes a solution to motion artifact resilient cuff-less BP monitoring in Chapter 5. Our proposed methodology has been verified with the data collected from 20 healthy young individuals during their walking motions.

1.5 Contribution of this Dissertation to Meet the Challenges

A powerful tool to take up these challenges is the use of combining *cardiac signal processing methods* together with *machine learning* (ML) techniques. We state in this dissertation that biologically reasonable computational models can meet the challenges.

The chapters of this dissertation are organized as follows. Chapters 2-5 contain the cardiac sig-

nal challenges of and our proposed solutions to heartbeat detection, arrhythmia classification, biometric identification, and blood pressure estimation. Chapter 6 concludes the theme of this dissertation.

- Chapter 2 presents three heartbeat detection methods, in which physiology is considered to leverage the performance of the state-of-the-arts. The first approach is our *Star-ECG*, a novel ECG visualization tool for non-experts to easily detect heartbeats and compute heart beat information such as heart rate and heart rate variability. Next, we showcase our waveform-based heartbeat detection algorithm targeted for low SNR ECG data of arrhythmia patients. Last, we exhibit our competitive heartbeat detection algorithm for SCG data of healthy people.

- Chapter 3 presents three fully automated biologically reasonable machine learning-based ECG arrhythmia classification models, two for single lead and the other for 12-lead. Both single lead algorithm were verified on the MIT-BIH data, and the 12-lead model was tested on six datasets with over 40,000 patients across Asia, Europe and the North America continents.

- Chapter 4 presents three cardiac signal-based biometric identification systems. The first system leverages ECG as the biometric, whereas the other two systems are oriented for SCG data. Of the two SCG biometric authentication systems, one is for healthy people in supine position, and the other is for healthy people in positions susceptible to motions, including sitting post-exercise, standing, and walking.

- Chapter 5 presents a wearable, low-cost, and ultra-convenient BP monitoring methodology. This method requires no cuff and is able to perform continuous BP monitoring when the person is walking. Such approach enhances both signal processing techniques and machine learning algorithms to properly select the physiological features correlated to BP values.

- Chapter 6 concludes the dissertation with a brief look toward the future.

Chapter 2

Computational Methodologies for ECG and SCG Heartbeat Detection

This chapter presents three heartbeat detection methods, two for ECG and one for SCG. First, we demonstrate *Star-ECG*, a novel ECG visualization tool that promisingly enhances heartbeat detection and heart rate variability computation for general people. Next, we showcase a waveform-based ECG heartbeat detection algorithm, which was verified on MIT-BIH Arrhythmia dataset [36] [79] along with the state-of-the-art performance. Last, we present our SCG heartbeat detection strategy, which is leveraged by motion artifact resilient cardiac signal processing techniques.

2.1 Challenge in ECG Heartbeat Detection for Non-experts

Cardiovascular diseases are the leading cause of global death due to its high prevalence and associated high mortality [9] [11]. Given its severity, real time monitoring and early diagnosis of abnormal cardiac activities are critical in clinical practice. In this end, electrocardiogram (ECG) has become a

popular arrhythmia diagnostic tool, as ECG is non-invasive and easily accessible. ECG is a recording of the electrical activity of the heart [56]. Each cardiac cycle is identified by the periodic characteristic points. It is widely known that variations of the ECG signal are associated with changes in cardiac dynamics. Most of the time, ECG is examined through simple visual inspection of the one-dimensional (1D) temporal ECG waveform [51].

However, abundant information remains hidden to human observation in 1D ECG, especially to people without the domain knowledge. To effectively improve the healthcare environment, easy-to-read ECG is highly required. It is reasonable that arrhythmia patients are eager to learn how to read their abnormal heart rhythms. More importantly, once the patients can read the abnormality in their cardiac activities, they can make effective conversations with the cardiologists and improve health outcomes throughout the treatment [3]. In addition to arrhythmia patients, people around the globe can also benefit from a user-friendly ECG reading tool to monitor their cardiovascular health. A different ECG visualization method is desired since 1D ECG waveform is difficult for general public to interpret.

In an effort to improve ECG rhythm readability, we present a novel ECG visualization technique along with an integrated convolutional neural network (CNN) arrhythmia classifier. We proposed Star-ECG, a novel ECG visualization tool that generates a star-like image and reflects the ECG waveform in a circular form. Such visualization enhances the readability of heart rate (HR) and heart rate variability (HRV) without the requirement of heavy computation. Moreover, we integrate deep learning into Star-ECG to classify arrhythmia, and we demonstrate that Star-ECG achieves satisfying classification performance with experts' approval.

2.1.1 Related Works

Various ECG visualization tools have been designed for different usages, including interactive ECG tools for cardiologists, supportive large ECG data visualization, and static ECG visualization. Regarding interactive methods, some widely used desktop applications have been developed by AMPS [121], ECGSoft [28], and OFFIS [122]; other proposed interactive web-based applications are bECG [73] and a similar tool designed by Oefinger *et al.* based on the open source programs [82]. For supportive large ECG data usage, Acharya *et al.* presented a thirteen types arrhythmia detection tool through monitoring 24-hour ECG data [1]. Xu *et al.* exhibited ECGLens for cardiologists to examine arrhythmia [112].

For static ECG visualization, researchers have proposed several techniques based on mathematically transforming or remapping ECG signals. In the 1970s and 1980s, vectorcardiogram (VCG) had been largely studied to extract spatial ECG information [31], [74]. However, Rubel *et al.* point out the drawback that the technique requires three orthogonal leads to record ECG [93]. Another approaches are based on frequency analysis. Fourier transform, time-frequency analysis, and wavelet transform have been applied in Kamath and Fallen's study [58], Stridh *et al.*'s work [100], and Addison's research [4], respectively. Illane *et al.* proposed a phase-portrait approach to visualize ECG [51], but it has been criticized to be difficult to read [112]. These frequency-oriented techniques reveal more information on HRV; however, they require costly computation and are difficult for people without technical expertise to comprehend.

2.1.2 Methodology and Experimental Design

Experimental Design

To ease the reading of ECG for people without expertise, we aim at designing an intuitive ECG visualization method. Such method is expected to meet below the five requirements:

- **Easy-to-read visualization:** The designed visualization should deliver ECG information in a fashion that relies on no expertise, which enables the users to learn how to visualize the new ECG in a short time.
- **Fast heartbeat regularity identification:** The visualization approach should make the users feel comfortable on determining the regularity of ECG heartbeats.
- **Straightforward heart rate computation:** The visualization strategy should allow the users to easily compute the HR without any additional computing resources such as a calculator or a computer.
- **Simple heart rate variability computation:** The visualization technique should ease the users' burden on figuring out the HRV.
- **Accurate arrhythmia classification:** The visualization tool should include an accurate automated arrhythmia classification program.

Star-ECG Generation

To fulfill the design requirements, we propose **Star-ECG**, a visualization technique that represents ECG like a ninja star and incorporates arrhythmia classification into the system. We elaborate on the design of Star-ECG by first explaining the transformation from 1D ECG to Star-ECG, introducing

the visual features of Star-ECG, then describing the integrated arrhythmia classification function, and last demonstrating how to read Star-ECG.

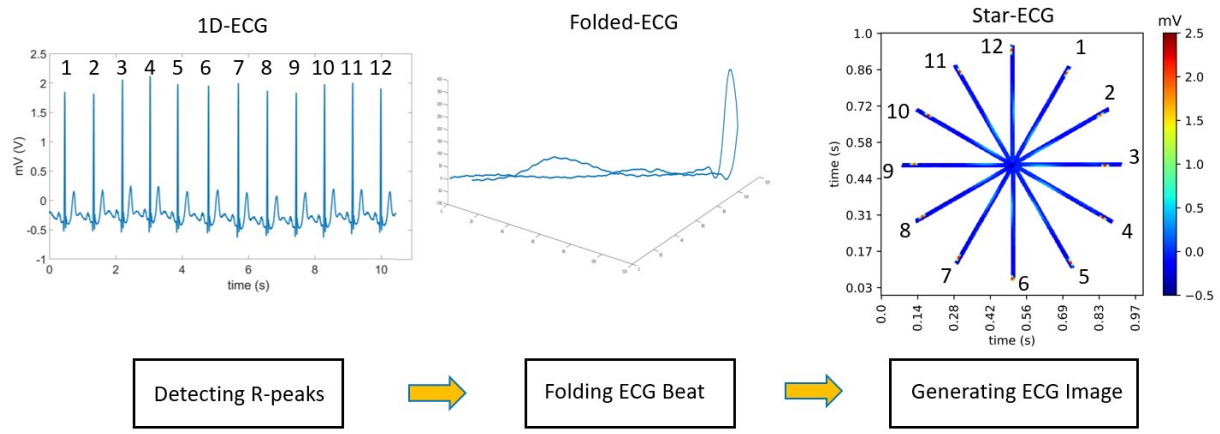

Figure 2.1: Demonstration of the Star-ECG generation technique. We label the sequence of heartbeats with Arabic numbers 1-12 on both the 1D-ECG signal and Star-ECG. The sequential order on Star-ECG is the same as the Arabic numbers on a clock.

Intuitive Visualization Design

To generate the intuitive Star-ECG visualization, we devise a procedure containing three steps as illustrated in Fig. 2.1 to transform traditional 1D ECG into Star-ECG.

- **Step 1:** Detecting ECG Heartbeats;
- **Step 2:** Folding ECG Heartbeats;
- **Step 3:** Rotating ECG Heartbeats.

The primary step is to identify all the heartbeats in 1D ECG, and as displayed in Fig. 2.1, each recognized heartbeat is labeled with an Arabic number above. To accomplish this task, we run the famous Pan-Tompkins algorithm to recognize the highest voltage peak in each heartbeat [83], which is known as the *R-peak* in conventional ECG. The Pan-Tompkins algorithm is one of the state-of-the-art real-time

ECG R-peaks detection techniques, and it possesses the advantages of high R-peaks detection sensitivity and fast computation time [41].

In the second step, we fold each ECG heartbeat into two halves. To perform this task, we first compute the positions of the two endpoints in each heartbeat. For searching the endpoints of one heartbeat, we need three consecutive R-peaks positions, with the middle one being the heartbeat that we want to fold. Subsequently, we acquire the two endpoints by computing the midpoints of the positions of each two consecutive R-peaks. Once we have the two endpoints, we fold the ECG heartbeat into two equal halves. To explain the folding process, let's denote the timing positions of the two midpoints as M_1, M_2, the original ECG data as $D(t)$, and the folded ECG data as $F(x,y)$. Our ECG heartbeat folding then follows the mathematical expressions:

$$F(1 : \lfloor \frac{M_1+M_2}{2} \rfloor - M_1 + 1, 2) = D(M_1 : \lfloor \frac{M_1+M_2}{2} \rfloor),$$
$$F(1 : M_2 - \lfloor \frac{M_1+M_2}{2} \rfloor, 1) = D(M_2 : -1 : \lfloor \frac{M_1+M_2}{2} \rfloor + 1).$$

We project the 1D ECG onto a 2D matrix with the first half ECG directly assigned to the first row and the second half mapped reversely to the second row of the matrix.

Finally, we rotate the folded ECG heartbeats to produce Star-ECG. Given N number of folded ECG heartbeats, we project them onto an image in a circular form with equally split angle. To be more specific, we demonstrate the rotation in the following Algorithm 1:

Algorithm 1 Star-ECG Image Generation

Input: Folded ECG Data $\{F_1, F_2, ..., F_N\}$, Starting Angle θ, Sampling Rate f_s
Output: Star-ECG Image Im

$Im = zero(f_s + 1, f_s + 1)$ // Create an image of zeros
for $i = 1 : N$ **do**
    $C = Coordinate(F_i)$
    $rx = C(x) \times \cos(-2\pi \times (i-1)/N + \theta)$
    $ry = C(y) \times \sin(-2\pi \times (i-1)/N + \theta)$
    $Im[rx + f_s, ry + f_s] = F_i$
end for
return Im

The inputs to Algorithm 1 are the folded ECG matrices along with a specified starting angle θ and sampling rate f_s; the output is a two-dimensional Star-ECG image *Im* representing *N* ECG heartbeats. The algorithm consists of a for loop, and in each iteration, it projects data matrix F onto image *Im* with an increase in the angle of rotation by $2\pi/N$ rad. In Fig. 2.1, we illustrate an example of 12 heartbeats case.

Read a Clock: Star-ECG displays 12 ECG heartbeats in a clockwise fashion as illustrated in Fig. 2.1. When designing the number of ECG heartbeats to display in Star-ECG, we consult both experts in cardiology and visualization. Experts in cardiology suggested the range of ECG heartbeat number being 10 to 15. Experts in visualization recommended to present 12 ECG heartbeats clockwise because then reading Star-ECG is like reading a clock. Based on the advice from the experts, we decide to exhibit 12 consecutive ECG heartbeats clockwise on Star-ECG. Moreover, to align with the clock reading, we set the starting angle θ as $\pi/3$, so the first heartbeat on Star-ECG is consistent with number *1* on the clock. Star-ECG is anticipated to provide intuitive perception since reading the Star-ECG is analogous to reading a clock.

Color-coded ECG Voltage: Star-ECG colors the voltage with a Jet colormap to enhance the image readability for the users. While painting Star-ECG, we also consult the experts in cardiology for

the range of voltages to plot. The experts suggested a range from -0.5 to 2.5 milli-volts (mVs). Therefore, we took the advice and set Jet colormap to span from -0.5 mV to 2.5 mV. We map the lowest voltage to color dark blue and the highest voltage to color dark red. Moreover, to intensify the contrast of R-peaks to other parts in ECG waveforms, we assign white color to the background. We depict an example of the contrast in the rightmost plot in Fig. 2.1. The R-peak regions are short and in red-orange color compared to the long and blue-colored low voltage segments.

Heart Rate Features

To enhance visualizing heart rate related information, we add three features to Star-ECG. The first feature assists on determining the regularity of heartbeats. The second feature accelerates the speed of HR computation. The third feature speeds up the calculation of HRV. We will discuss each feature in the following paragraphs.

View Heartbeat Regularity: As depicted in Fig. 2.2, we use light purple colored circles to aid visualizing the heartbeat regularity. The origin of this circle lies in the center of Star-ECG, and the diameter is equal to the HR of the 1D ECG. To derive the HR, we discussed with the expert on the HR computation. The expert recommended computing the HR of 20 consecutive ECG heartbeats using the following algorithm:

Algorithm 2 Star-ECG Heart Rate Computation

Input: 20 Consecutive R-peaks Positions $\{R_1, R_2, ..., R_{20}\}$, Sampling Rate f_s
Output: Star-ECG Heart Rate HR

$DR = []$ // Create an empty array
for $i = 2 : 20$ **do**
    $DR[i-1] = R_i - R_{i-1}$
end for
$HR_1 = mean(DR[1:9])$ // R-R intervals 1 - 10
$HR_2 = mean(DR[6:14])$ // R-R intervals 6 - 15
$HR_3 = mean(DR[11:19])$ // R-R intervals 11 - 20
$HR = (HR_1 + HR_2 + HR_3)/(3f_s)$
return HR

The inputs to this algorithm are 20 R-peaks positions and the sampling rate f_s; the output of Algorithm 2 is the computed HR. According to the expert, the more accurate HR computation should be the average of the heart rates of the overlapping heartbeats; therefore, we adopt this computation strategy in Star-ECG. For the 12 ECG heartbeats on Star-ECG, they are the middle 12 ECG beats of the 20 consecutive heartbeats.

View Heart Rate: We utilize the horizontal and vertical ticks as the scale of the HR. To derive the HR from Star-ECG, the users only have to refer the diameter of the circle to either the horizontal or vertical ticks for the answer. Since Star-ECG is pictured as a squared image of one-second side length, we leverage the usage of the ticks by stretching the scale from 0 to 1 for both horizontal and vertical axes (Fig. 2.2).

View Heart Rate Variability: To disclose the HRV on Star-ECG, we portray two additional circles on top of the HR circle as displayed in Fig. 2.2. We first compute the HRV with the standard deviation R-R interval (SDRR) metric defined in the study written by Shaffer and Ginsberg [97], and following the HRV computation, we illustrate two circles on Star-ECG with both origins at the center and diameters of $HR - HRV$ and $HR + HRV$, respectively. As a result, we arrive at the Star-ECG shown in Fig. 2.2.

Integration of Arrhythmia Classification

To meet the last design requirement, we leverage the CNN model to carry out the arrhythmia classification mission. We will cover the details of the arrhythmia classification topic in the next chapter.

Visualizing Star-ECG

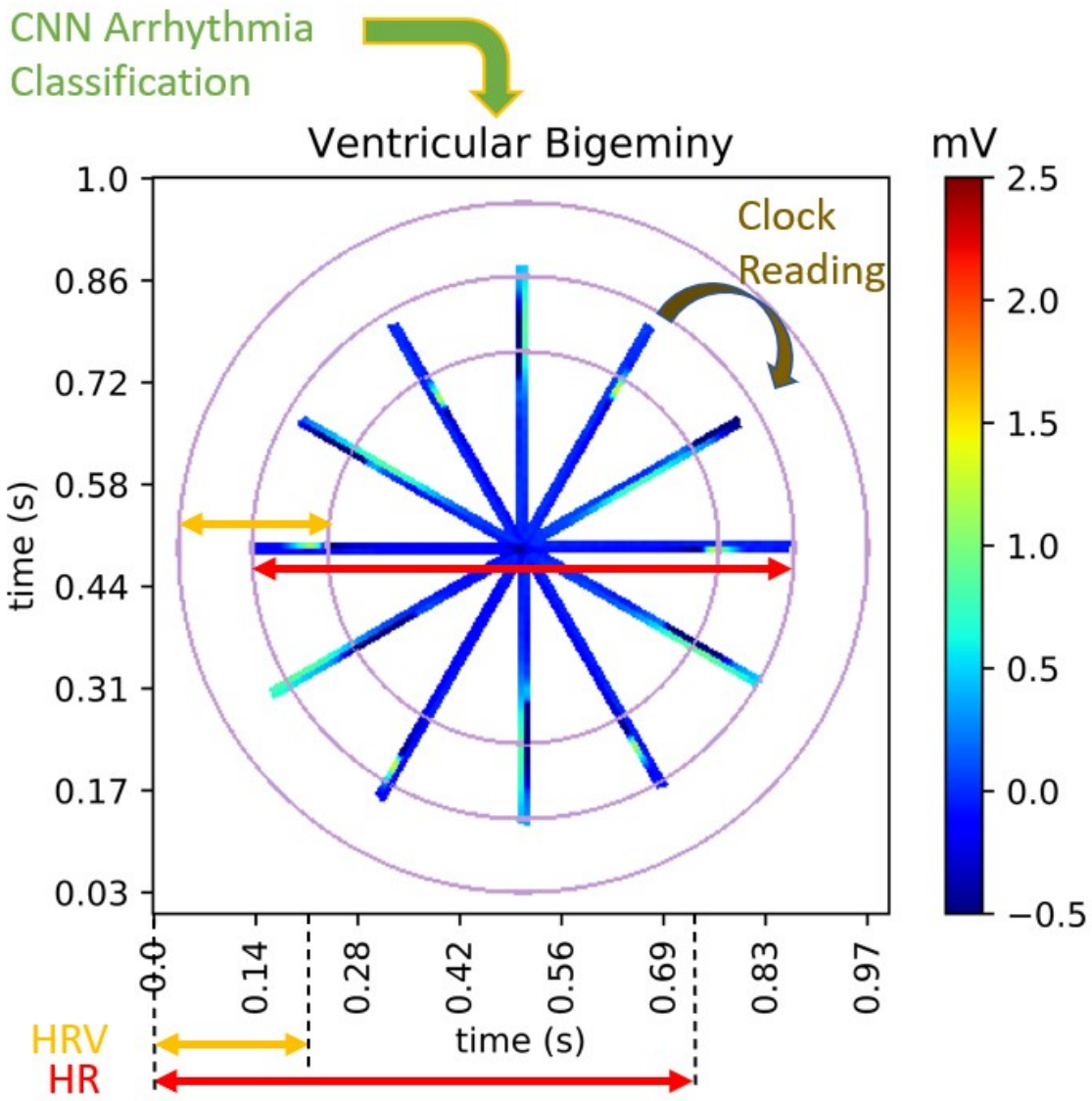

Figure 2.2: Guide of reading Star-ECG. Reading Star-ECG is analogous to reading a clock. The voltages of ECG are shown on the right colorbar. The HR is readable from the middle purple circle along with the scale on the tick, and the HRV is comprehensible from the inner and outer purple circles. The CNN arrhythmia classifier is integrated.

Star-ECG aims at encouraging non-experts and arrhythmia patients to easily visualize and monitor their ECG data. Learning to read Star-ECG is expected to be simple and requires no domain knowledge. A complete Star-ECG should contain a ninja star-like color-coded ECG with a color bar, three purple-colored circles, scale on the ticks, and the arrhythmia classification result displayed as text in the title. Below we describe the reading instructions of Star-ECG with the help of Fig. 2.2 as guidance:

How To Read Heartbeat Regularity: Reading Star-ECG is similar to reading a clock, and the users can perceive the heartbeat regularity through observing the lengths and colors of the star blades. Regular ECG heartbeats have nearly equal lengths and the same color distribution of star blades, and the users should visualize that all star blades' endpoints are close to the middle circle. Conversely, irregular ECG heartbeats possess variant lengths or differentiated colors among the star blades, and their endpoints are far away from the middle circle. We provide an example of regular versus irregular ECG heartbeats in Figures 2.3 and 2.4.

How To Read Heart Rate: The users can straightly compute the HR on Star-ECG. To arrive at the HR, the users should first measure the diameter of the middle circle and succeedingly refer its length to the scale labeled on the ticks. The approach is analogous to calculating the distance from the start point to the destination on a map.

How To Read Heart Rate Variability: To obtain the HRV, the users can refer the distance between the inner circle and the outer circle to the scale on the ticks. The method is very similar to obtaining the HR on Star-ECG.

How To Read Arrhythmia Type: The users can read the arrhythmia type classified by the CNN model in the title of Star-ECG. In addition, the users can perceive the existence of arrhythmia through observing the patterns of the star blades. According to the cardiology experts, arrhythmia can be abnormal HR, abnormal waveform, or abnormal intervals of some characteristic points in ECG. Thus, the users can

perceive the arrhythmia by visualizing the consistency of the colors, the lengths, and the positions of R-peaks in the 12 star blades. A healthy user should observe 12 consistent star blades in length, color, and fiducial points' position. While for users having abnormal cardiac activities, they will cognize the inconsistent patterns across the 12 star blades. We present the examples of normal and arrhythmia Star-ECG in Figures 2.3 and 2.4.

Participants and Dataset

We recruited 13 volunteers in our study with the approved consent form. All the volunteers did not have color vision deficiency. Ten volunteers do not have any cardiology expertise, while three volunteers do. They are aged 22 - 62 (mean: 38) and from different technical backgrounds. All the participants conducted the experiments through visualizing the data on the screen.

We used the MIT-DB dataset to run on Star-ECG. MIT-DB dataset is a popular publicly available arrhythmia dataset and has been employed in over thousands of studies relevant to cardiac abnormalities [36] [79].

Tasks

We designed four tasks for the participants to complete. In all the four tasks, the participants were asked to complete with both traditional 1D-ECG and Star-ECG. The four tasks were:

- **T1:** Identify Heartbeat Regularity
- **T2:** Compute Heart Rate
- **T3:** Compute Heart Rate; Variability
- **T4:** Classify Arrhythmia Type.

For tasks T1-T3, every volunteer was invited to accomplish. For task T4, only the experts were invited to participate since it requires the domain knowledge.

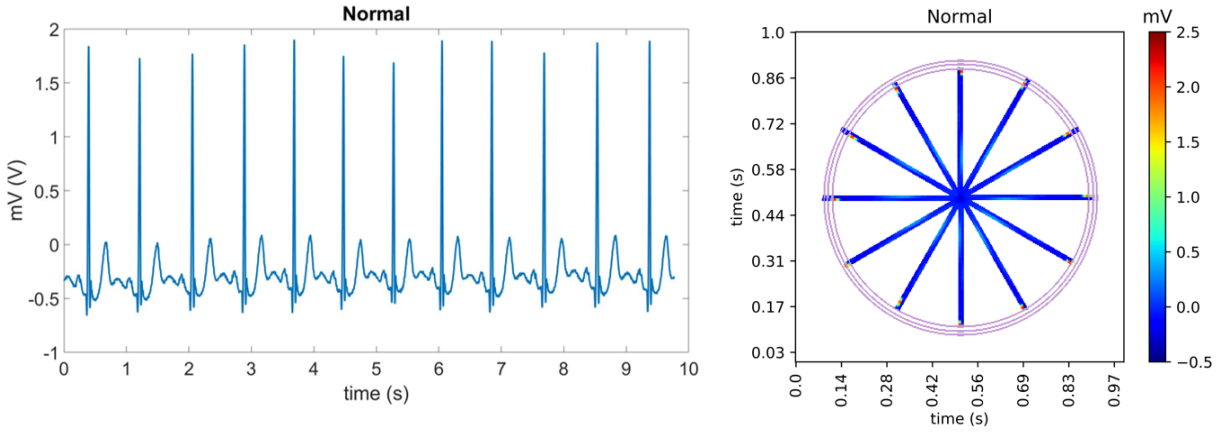

Figure 2.3: Normal Heartbeat on 1D-ECG (left) and Star-ECG (right).

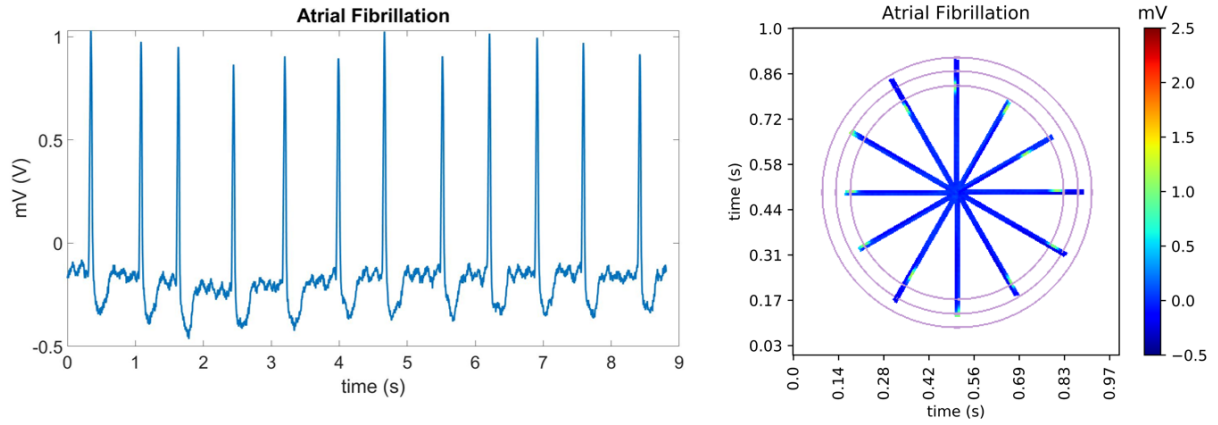

Figure 2.4: Abnormal Heartbeat on 1D-ECG (left) and Star-ECG (right).

Procedure

The study started with a brief tutorial to the participants about reading 1D-ECG and Star-ECG. We showed the participants how regular and irregular heartbeats looked on 1D-ECG and Star-ECG. Moreover, we demonstrated how to compute the HR and HRV with 1D-ECG and Star-ECG to the participants. Next,

we asked the participants to complete the four tasks and timed the completion time. For tasks T1-T3, we asked the participants to carry out the tasks with the cases illustrated in Figures 2.3 and 2.4. For task T4, we had the experts classify the 12 arrhythmia types as displayed in the supplementary files. After the participants finished the tasks, we conducted an interview with each participant to collect their feedback. In the interview, we asked the participants about their choice between the two visualization tools to perform the given tasks. Besides, the participants were encouraged to provide reasons over their choices and criticisms on Star-ECG.

2.1.3 Experiment Results

We present the results in the order of the numbering of the tasks. In each task, we will first exhibit the time of completion and next the categorized feedback from our participants.

Table 2.1: Results of the tasks. The users choose their preferences between Star-ECG and 1D-ECG to complete the tasks. X stands for the scenario that the participants can observe regularity easily on both.

ID	Heartbeat Regularity Observation	Heart Rate Computation	Heart Rate Variability Computation
E1	X	Star-ECG	Star-ECG
E2	X	Star-ECG	Star-ECG
E3	X	Star-ECG	Star-ECG
N1	Star-ECG	Star-ECG	Star-ECG
N2	X	Star-ECG	Star-ECG
N3	Star-ECG	Star-ECG	Star-ECG
N4	Star-ECG	Star-ECG	Star-ECG
N5	Star-ECG	Star-ECG	Star-ECG
N6	Star-ECG	Star-ECG	Star-ECG
N7	Star-ECG	Star-ECG	Star-ECG
N8	X	Star-ECG	Star-ECG
N9	Star-ECG	Star-ECG	Star-ECG
N10	Star-ECG	Star-ECG	Star-ECG

T1 Time of Completion: All the participants successfully identified the regular and irregular ECG patterns on 1D-ECG and Star-ECG. The participants spent an average time of 12 seconds (SD = 3.4) to complete T1 using Star-ECG and 31 seconds (SD = 5.2) using 1D-ECG. Based on the results, visualizing heartbeats regularity on Star-ECG is 2.58x faster than on 1D-ECG.

T1 Interview Feedback: As exhibited in Table 2.1, we received positive feedback on Star-ECG from most participants (80%) and neutral responses from all three experts. The participants voting for Star-ECG enjoyed the ease of visualizing 12 ECG heartbeat lengths. Participant N3 said *" I like the idea of an auxiliary circle plus the ninja star blades. I can quickly notice the irregular heartbeats on a circular plot but not the 1D wave."* Participant N6 said *" I like the color-coded ECG because I have difficulty interpreting the ups and downs on a one-dimension ECG. The colors definitely enhance the readability of ECG."*As for the experts and two non-experts, they mentioned that they encountered no difficulties visualizing ECG regularity on both 1D-ECG and Star-ECG.

T2 Time of Completion: All the participants successfully figured out the HR on Star-ECG, but not on 1D-ECG. Participants N9 and N10 did not complete T2 on 1D-ECG. We considered all the successful cases and found out that the participants spent an average time of 6 seconds (SD = 2.2) to complete T2 using Star-ECG and 454 seconds (SD = 63) using 1D-ECG. Based on the results, computing the HR is 75.7x faster on Star-ECG than on 1D-ECG.

T2 Interview Feedback: We received 100% positive feedback on Star-ECG from our participants upon finishing task T2 as listed on Table 2.1. We summarized the interview talks from all the participants and concluded with the mainly two supportive reasons:

1. Ease of use: Users of Star-ECG can directly compute the HR instead of tracing the whole 1D-ECG, which takes several minutes to complete. Every recruited participant agreed with it.

2. Transferable skill: Users can apply their knowledge on computing the distance on the map to cal-

culating the HR on Star-ECG. Participants N2, N4, N5, N7, N9 approved such transferable knowledge. Participant N7 reported *"Star-ECG is really interesting! I didn't realize we can measure time distance in this way as we do on Google Map until now!"*

For the two non-experts who were unable to complete T2 on 1D-ECG, they complained that 1D-ECG required complicated computations that they could not afford.

T3 Time of Completion: All the participants successfully figured out the HRV on Star-ECG, but not on 1D-ECG. Only the experts and participants N2, N8 complete T3 on 1D-ECG; the rest of the participants did not arrive at the HRV with 1D-ECG. We considered all the successful cases and found out that the participants spent an average time of 8 seconds (SD = 4.3) to complete T3 using Star-ECG and 632 seconds (SD = 101) using 1D-ECG. Based on the results, computing the HR is 79x faster on Star-ECG than on 1D-ECG.

T3 Interview Feedback: We also received 100% positive feedback on Star-ECG (Table 2.1). More importantly, all the experts endorsed the HRV visualization on Star-ECG. Expert E1 said, *"The straightforward HRV visualization is great. I am willing to use it to monitor the patients' health status."* Expert E2 mentioned, *"The HRV idea is good. I hope you keep doing the great work."*Expert E3 stated, *"The HRV is doable, really really exciting! It can bridge the communication gap between the patients and us."* For other participants without the expertise, they mentioned the concept of HRV was difficult to comprehend and that the computation loading was even heavier than computing the HR on 1D-ECG. Therefore, they would favor Star-ECG over 1D-ECG for task T3.

Qualitative Results of Arrhythmia Classification T4

Validation with Experts: We interviewed with the experts about their opinions on arrhythmia classification and received helpful feedback. Every expert liked the CNN model of Star-ECG, especially

the sufficiently high classification accuracy. However, the experts were concerned about reading arrhythmia directly through Star-ECG visualization. According to expert E1, *"I like the way combining CNN together with Star-ECG. It helps me to make accurate arrhythmia diagnosis. However, if I were to classify arrhythmia through reading the star blades only, I would still go with 1D-ECG."* Expert E2 said, *"CNN is great, but I would suggest visualizing multiple ECG-leads on Star-ECG instead of a single lead for arrhythmia decision. It is easy to visualize specific types of arrhythmia on Star-ECG, such as ventricular bigeminy and trigeminy, but not those relative to abnormal P-wave segments."* Expert E3 mentioned, *"I would still choose 1D-ECG because some detailed waveform information is not obvious to read on Star-ECG. Nevertheless, I would recommend showing Star-ECG to the patients instead of 1D-ECG for basic understanding of cardiac abnormalities."* In summary, the experts believed that Star-ECG would be a good visualization tool for non-experts, and CNN was a brilliant idea. Nevertheless, the experts would like to view additional physiology information on Star-ECG in order to have confidence on making precise arrhythmia diagnosis.

2.1.4 Conclusions

Discussion

Based on the results, Star-ECG has showcased its effectiveness over conventional 1D-ECG in visualizing heartbeat regularity, heart rate, and heart rate variability, especially for people without the cardiology expertise. Furthermore, the integrated CNN model enhances the functionality of Star-ECG.

Visualization Tasks: Star-ECG succeeded in providing easy visualization in terms of the heartbeat regularity, heart rate, and its variability. For the heartbeat regularity, the circular star-blades, auxiliary circle, and color-coded ECG were pointed out to be helpful in the judgment. With respect to HR and HRV, Star-ECG was favored due to its readability. What's more significant, the experts approved the HRV vi-

sualization and are willing to put into clinical practice.

Arrhythmia Classification: The integration of CNN model won positive feedback from the experts, and the developed CNN model has achieved state-of-the-art performance. Although some detailed physiology information is difficult to read due to its simplicity, Star-ECG is recommended by the experts to provide the fundamental learning of arrhythmia to users without the domain knowledge.

Limitations: Based on the collected feedback from both experts and non-experts, we have discovered certain limitations of the current Star-ECG:

- **Demand for detailed physiology:** Star-ECG provides friendly visualization of certain features due to its simplicity, but such simplicity hinders the detailed physiology information from display. In addition, one of the experts mentioned that visualizing multiple ECG leads could strengthen the confidence in arrhythmia diagnosis.

- **Constraints on the user's activity:** The experts pointed out that Star-ECG might not function as expected if the users are performing extreme physical exercise. Therefore, to manage such scenario, Star-ECG should integrate advanced ECG signal processing technology.

Summary and Future Work

In this paper, we present Star-ECG, a novel ECG visualization tool. We describe the procedure to transform a traditional one-dimensional ECG into Star-ECG and showcase the effectiveness of Star-ECG in visualizing the heartbeat regularity, heart rate, and heart rate variability. Besides the innovative visualization, we also integrate deep learning technology and deliver a state-of-the-art arrhythmia classifier. Moreover, we receive positive feedback on Star-ECG visualization from both the experts and people without the medical expertise.

In our future work, we aim at addressing the limitations of the current Star-ECG. We plan to add

more physiological features into a new version of Star-ECG. Furthermore, we intend to investigate the visualization techniques for multiple ECG leads.

2.2 Challenge in Heartbeat Detection of Abnormal ECG

Electrocardiogram (ECG) is one of the most essential bio-signals. ECG can represent the heart activity and is used for monitoring human's health status [110]. Heartbeat detection is the primary step in ECG analysis, and in particular, researchers target at detecting the positions of R-peaks. Since the R-peak is the most perceptible in a heartbeat, researchers aim at searching the distance between two consecutive R-peaks, which can be further applied to monitoring heart rate variation [110].

We present the waveform-based R-peak detection method and the strategy of combining both waveform-based and threshold-based approach in subsection (2.2.2). In subsection 2.2.3, we exhibit the results of R-peaks detection and conclude in subsection 2.2.4.

2.2.1 Related Works

R-peak detection strategies can be divided into two categories: threshold-based and waveform-based [33]. Threshold-based approach extracts R-peaks with a threshold determination. Many researchers have proposed different pre-processing techniques and statistical analysis for noise-tolerant threshold to enhance the performance of threshold-based methods. Among threshold-based approach, Pan-Tompkins algorithm is the most popular [83]. Waveform-based method includes using autocorrelation [23] or template matching tactics [19]. It does not require adaptive threshold computation process as threshold-based method does. In addition, ECG waveform simulation has been studied to generate synthetic ECG. For example, McSharry *et al.* demonstrated a synthetic ECG by using mixture of Gaussians [77]. It is logical to make use of synthetic ECG in waveform-based strategy [77].

2.2.2 Methodology and Experimental Design

Database

MIT–BIH arrhythmia database [79] from publicly available PhysioNet [36] was chosen to test our waveform-based ECG R-peaks detection algorithm. The data includes a total of 48 records sampled at 360 Hz, and all 48 records contain ECG data of 30 minutes duration. For all the records, lead II signal was selected for analysis if available; otherwise, the signal from the first channel was adopted for experiments.

Waveform-based Signal Processing

There were four steps in waveform-based signal processing (WBSP) procedure as demonstrated in Figure 2.5: low-pass filtering, local minima search, removal of drift, and curve fitting. First, we passed the raw ECG signal into a low-pass filter with 35 Hz cutoff frequency. Next, we searched the local minima of the filtered ECG signal. To be more precise, the start and the end of the signal were both considered as local minima. Subsequently, we used cubic spline to connect the local minima found in the previous step, and we subtracted the piece-wise cubic spline curve from the filtered ECG signal so as to remove the drift. Every local minima data-point became zero after the drift removal, and we refer these zero valued local minima as *knots* in the rest of the paper. Last, we fit each curve between every two neighboring knots with a Gaussian model as expressed in (2.1).

$$G(t) = a \cdot e^{-((t-b)/c)^2} \tag{2.1}$$

We recorded the determination of coefficient R^2, the area and the ratio of the curve as defined in (2.2) and (2.3) for R-peak detection.

$$area := \sqrt{|a|} \cdot |c| \tag{2.2}$$

$$ratio := |\frac{a}{c}| \tag{2.3}$$

According to McSharry *et al.* [77], Gaussian curves are suitable to model the P, QRS, and T waves of ECG signals; therefore, we chose Gaussian curves to parameterize the curve between each two neighboring knots.

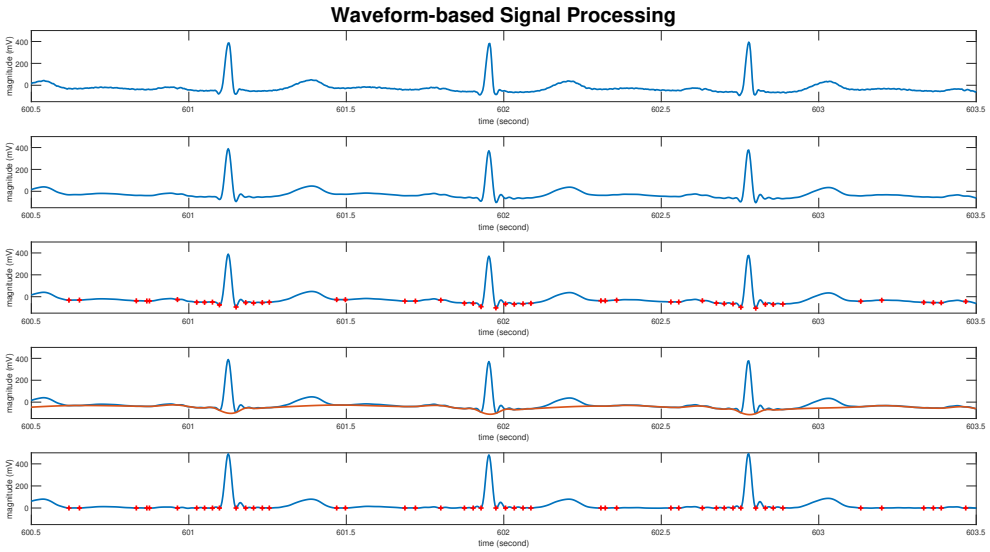

Figure 2.5: Demonstration of Waveform-based Signal Processing Method. Top row shows the raw ECG signal. Intermediate rows display the low-pass filtered results, searched local minima annotated in red cross, and drift removal in orange. Bottom row displays the processed signal for Gaussian fitting.

ECG R-Peaks Detection Procedure

Our proposed *Waveform-based R-peaks Detection Procedure* is performed in three steps: 1) shape recognition, 2) R-peaks sifting, and 3) search back for missed peaks. The inputs are raw ECG data and

products of WBSP; the output is R-peak positions.

First step - Shape Recognition: We developed an R-peak shape recognition method by combining WBSP procedure and sliding window technique. The idea was to identify the curve within the current window as a valid QRS wave if the following four conditions were all satisfied:

1. The ratio of the curve, $|\frac{a}{c}|$, is the largest in the window.

2. The summation of the areas in the center of the window is larger than 50%. Given window length T, the summation of the areas from length $0.25T$ to $0.75T$ should occupy more than half of the areas over the entire window.

3. The curve should lie in the first half of the window (between $0T$ to $0.5T$).

4. The coefficient of determination R^2 of the Gaussian curve fitting result should be at least 0.95.

Such approach made use of the shape of QRS wave and the quasi-periodicity of ECG signal. The shape of a QRS wave was represented by the parameters of the Gaussian model; the periodicity was handled with a moving window of appropriate length.

The length of the window was computed through curve fitting with Fourier basis terms in linear regression. Eq (2.4) shows the least square method optimization that the current study adopts to determine the window length.

$$\arg\min_{w} = ||y(t) - (w_0 + \sum_{n=1}^{15} w_n \, cos(2\pi(0.5 + 0.1n)t))||_2 \tag{2.4}$$

The selected Fourier basis terms consisted of a constant and cosines ranging from 0.6Hz to 2.0 Hz with 0.1Hz increment. The first 30-second long WBSP processed ECG signal was fed into the Fourier basis curve fitting model, and the cosine term with the largest magnitude represented the period of the ECG signal. The window length was set as half of the period.

After setting the length of the sliding window, we performed recognizing the existence of an R-peak and sliding the window iteratively. The iteration ended when the window slid to the end of the processed ECG data. If an R-peak existed in the current window, we recorded the R-peak's position, and slid the window until the two knots enclosing the R-peak were outside the window; otherwise, we slid the window by the distance of the length between the first two knots.

Algorithm 3 Shape Recognition

Input: Parameters and Processed ECG data using WBSP method
Output: R-peaks indices

```
Initialize the size of the sliding window
while not reaching the endpoint of the data do
    if valid QRS curve exists in the window then
        Mark the peak of the QRS wave as R-peak
        Shift the sliding window until the curve with the identified R-peak is out of view
    else
        Shift the sliding window by the distance of the first two knots
    end if
end while
```

Second step - R-peaks Sifting: We ran R-peaks sifting after *shape recognition* algorithm was performed because two issues could remain in the identified R-peaks: false positives (FP) and false negatives. To resolve these two issues, we designed an R-peaks sifting algorithm based on a data thresholding approach. In false negative cases, we marked the peak lying between two neighboring R-peaks as a valid R-peak if its magnitude exceeds 0.8 of the average of the two identified R-peaks and was separated by at least 200ms away from both R-peaks (physiological refractory time [83]). In false positive cases, we identified the R-peak with magnitude less than 0.8 of the average of its two neighboring R-peaks as a false positive R-peak. The sifting process, false negative identification and false positive removal, was repeated 20 times. In our experiments, we found that 20 sifts were sufficiently large to reach the stable state, which is defined as the differences of R-peaks found between two consecutive sifts.

Algorithm 4 R-Peaks Sifting

Input: R-peaks Identified by Shape Recognition and Raw ECG data
Output: R-peaks indices

// R_i denotes the index of the i^{th} R-peak
for $i = 1 : 20$ **do**
    Run Add False Negatives Procedure
    Run Remove False Positives Procedure
end for
/* Add False Negatives Procedure */
for every two neighboring R-peaks (R_i, R_{i+1}) **do**
    if $R_{i+1} - R_i > 0.4s$ **then**
        ECG_chunk = ECG$[R_i + 0.2s : R_{i+1} - 0.2s]$
        max_peak = max(ECG_chunk)
        threshold = $0.8 \times (ECG(R_i) + ECG(R_{i+1}))/2$
    end if
    if $max\_peak > threshold$ **then**
        Mark max_peak as R-peak
    end if
end for
/* Remove False Positives Procedure */
for every 3 neighboring R-peaks (R_i, R_{i+1}, R_{i+2}) **do**
    threshold = $0.8 \times (ECG(R_i) + ECG(R_{i+2}))/2$
    if $R_{i+1} < threshold$ **then**
        Unmark max_peak as R-peak
    end if
end for

Third step - Search Back for Missed R-peaks: The last step in R-peaks detection procedure was to search the missed R-peaks. Most false positive R-peaks had been removed in the second step (*R-peaks Sifting*); however, some low magnitude R-peaks were also mistakenly marked as false positives. Therefore, we devised a search back algorithm to find the missed R-peaks.

The concept was to mark the missed R-peaks on the basis of both waveform similarity and the duration between two neighboring identified R-peaks. We first estimated the period of the subject by averaging the R-R interval less than 1.2s. Subsequently, we investigated the R-R interval larger than the estimated period, and employed the floor of the ratio of R-R interval over period as the number of missed R-peaks, which is denoted as K.

For data similarity quantification, we first fed the raw ECG data into a bandpass filter ranging from 5 to 15 Hz. Then, we computed the ensemble average of 1 second long filtered data with the identified R-peaks as centers. Next, for every R-R interval larger than the period, we sought the first K maximum peaks between the two R-peaks, which were the K candidate R-peaks. Last, we conducted cross-correlation analysis between the ensemble average and the 1 second long data centered at the candidate R-peak. If the correlation coefficient was larger than 0.5, we considered the candidate R-peak as a valid R-peak.

Algorithm 5 Search Back for Missed R-Peaks

Input: R-peaks Identified by R-peaks Sifting and Raw ECG data
Output: R-peaks indices

// R_i denotes the index of the i^{th} R-peak
Bandpass filter ECG with frequencies ranging from 5 to 15 Hz
Initialize $N = 0$, $period = 0$
// Seek the ECG Period of the subject
for every two neighboring R-peaks (R_i, R_{i+1}) **do**
  if $R_{i+1} - R_i < 1.2s$ **then**
    period = period + $R_{i+1} - R_i$
    N = N + 1
  end if
end for
period = period / N
// Find the missed R-peaks in R-R Interval $>$ Period
eaECG = Ensemble average 1 second long bandpass filtered data with R-peaks as center alignment
for every 2 neighboring R-peaks (R_i, R_{i+1}) **do**
  if $R_{i+1} - R_i > period$ **then**
    K = floor($(R_{i+1} - R_i)$ / period)
    Find K maximum peaks
  end if
  for k=1:K **do**
    C_k = cross-correlation coefficient of (fECG[$R_k - 0.5s : R_k + 0.5s$], eaECG)
    if $C_k > 0.5$ **then**
      Mark R_k as R-peak
    end if
  end for
end for

Combining Waveform-based & Threshold-based Methods

Waveform-based R-peaks detection method relied on the quality of ECG signal; thus, we suggested another R-peaks detection technique to overcome the low ECG quality problems such as highly noisy data and excessively large baseline drift. The suggested R-peaks detection method combined our proposed waveform-based technique and Pan-Tompkins algorithm, which is a widely used threshold-based ECG R-peak detection technique [83].

The majority of the *combined R-Peaks Detection Algorithm* was similar to waveform-based approach except the last step. The last step in the combining method identified the missed R-peaks by running the Pan-Tompkins algorithm. For every R-R interval larger than the expected period, which was calculated by the third step of the waveform-based procedure, we ran the Pan-Tompkins algorithm to seek the missed R-peaks instead. Such approach was expected to address the low signal quality issue.

2.2.3 Experiment Results

Performance Evaluation

We evaluated the performance of the proposed waveform-based and combined R-peaks detection methods with accuracy, precision, and recall. Precision is defined as the ratio of correctly detected R-peaks (true positives) over all the detected R-peaks (true positives + false positives). Recall is defined as the ratio of correctly detected R-peaks (true positives) over the correct R-peaks (true positives + false negatives). Accuracy is shown in Eq (2.5), and is defined as correctly detected R-peaks divided by the summation of the numbers of correct R-peaks and false positive peaks.

$$accuracy = \frac{TP}{TP+FN+FP} \tag{2.5}$$

Moreover, we compare our results with the widely used Pan-Tompkins algorithm. The tolerance window is 10% of the subject's averaged R-R interval, which is the metric adopted by Lourenco *et al.* [70].

Table 2.2: Performance of the Waveform-based, the Pan-Tompkins, and the Combined Algorithms on Normal Rhythm Group

Record	Waveform-based			Pan-Tompkins [83]			Combined		
Normal	Precision	Recall	Accuracy	Precision	Recall	Accuracy	Precision	Recall	Accuracy
100	100	100	100	100	99.96	99.96	99.96	99.96	99.91
101	100	99.41	99.25	99.89	99.47	99.47	99.73	99.57	99.31
103	100	100	100	100	99.62	99.62	100	99.67	99.67
105	98.33	94.17	92.68	98.31	93.56	93.56	96.87	95.43	92.57
108	90.77	91.12	83.39	83.82	81.38	81.38	78.1	96.77	76.11
109	100	100	100	100	99.68	99.68	99.96	99.84	99.8
111	91.66	97.94	89.93	99.95	98.97	98.97	91.64	99.2	90.97
112	100	100	100	100	99.57	99.57	100	99.53	99.53
113	100	100	100	100	99.94	99.94	99.83	99.94	99.78
115	100	100	100	100	99.54	99.54	100	99.54	99.54
116	98.9	81.41	80.68	99.83	98.47	98.47	98.76	98.88	97.67
117	100	100	100	100	99.74	99.74	99.93	99.68	99.61
118	100	99	98.83	99.96	98.96	98.96	99.78	99	98.79
121	100	99.15	99.04	100	99.2	99.2	100	99.2	99.2
122	100	100	100	100	99.88	99.88	100	99.88	99.88
123	100	99	99	100	99.74	99.74	100	99.87	99.87
212	100	99.42	99.42	100	99.46	99.46	100	99.46	99.46
Average	98.73	97.61	96.47	98.86	97.98	97.98	97.91	**99.14**	97.16

Table 2.3: Performance of the Waveform-based, the Pan-Tompkins, and the Combined Algorithms on Abnormal Rhythm Group, same color-code as Table 2.2

Record	Waveform-based			Pan-Tompkins [83]			Combined		
Abnormal	Precision	Recall	Accuracy	Precision	Recall	Accuracy	Precision	Recall	Accuracy
102	100	93.89	93.59	99.95	99.68	99.68	99.59	99.68	99.27
104	99.3	92.3	91.7	98.16	93.15	93.15	97.59	96.32	94.08
106	99.2	88.51	87.88	99.95	96.43	96.43	99.36	96.52	95.93
107	97.49	96.03	93.71	99.91	98.93	98.93	97.47	98.97	96.49
114	100	98.68	98.47	100	99.37	99.37	99.79	99.42	99.21
119	97.5	94.5	92.4	99.95	94.84	94.84	99.95	94.89	94.84
124	100	98.1	98.1	100	98.41	98.41	100	99.08	99.08
200	98.91	84.81	84.03	99.81	92.81	92.81	92.79	93.05	86.77
201	90	90.49	82.22	100	93.04	93.04	91.13	95.78	87.62
202	96.46	98.97	95.5	100	99.07	99.07	96.56	99.3	95.9
203	91.59	76.74	71.69	99.21	92.4	92.4	92.89	94.11	87.79
205	100	96.78	96.56	100	99.14	99.14	99.77	99.21	98.99
207	90	62	58	97.02	87.64	87.64	77.15	90.9	71.62
208	100	87.6	87.25	99.9	95.86	95.86	99.49	96.58	96.1
209	100	98.46	98.46	100	98.49	98.49	100	98.49	98.49
210	100	94.23	93.81	99.69	96.73	96.73	99.39	97.73	97.15
213	99.42	97.81	97.47	99.05	96.78	96.78	98.35	98	96.42
214	100	85.81	85.62	99.96	98.26	98.26	99.78	98.35	98.13
215	100	98.85	98.79	100	98.82	98.82	99.97	98.85	98.82
217	93.09	83.95	79.03	99.95	96.67	96.67	94.24	96.89	91.47
219	100	93.12	93.08	100	93.17	93.17	99.95	93.17	93.13
220	100	98.99	98.99	100	98.99	98.99	100	98.99	98.99
221	100	98.13	97.73	100	98.42	98.42	99.63	98.42	98.06
222	100	85.76	85.7	98.95	92.37	92.37	98.88	93.47	92.49
223	100	97.31	97.28	100	98.11	98.11	100	98.18	98.18
228	98.76	92.95	91.87	99.76	95.53	95.53	98.7	95.98	94.79
230	100	91.48	91.37	100	91.48	91.48	99.96	91.48	91.45
231	100	86.87	86.53	100	78.12	78.12	99.76	83.09	82.93
232	97.11	98.02	95.24	99.94	97.96	97.96	98.02	97.96	96.06
233	100	96.54	96.48	100	97.59	97.59	99.97	97.65	97.62
234	100	99.6	99.6	100	99.49	99.49	100	99.6	99.6
Average	98.35	92.17	90.9	99.71	95.73	95.73	97.75	**96.46**	94.43

Table 2.4: Sensitivities Reported on MIT-BIH Arrhythmia Database

Detector	Tolerance	Cited Recall
Pan and Tompkins (1985) [83]	Not Stated	99.30%
Elgendi *et al.* (2010) [29]	Not Stated	32.53% – 98.31%
Kalidas and Tamil (2017) [57]	Not Stated	22.34% – 99.88%
Luorenco *et al.* (2012) [70]	10% of R-R	96.50%
Pan and Tompkins (Our Implementation)	10% of R-R	96.53%
Ours	10% of R-R	**97.41**%

Performance of the Proposed R-peak Detection Method

We compare the proposed waveform-based and combined R-peak detection methods with Pan-Tompkins algorithm [83] in Tables 2.2 and 2.3. We split the records into two categories based on the rhythm: normal and mixed/abnormal. In addition, we use three different colors to represent the recommended R-peak method for the records: green for waveform-based, red for Pan-Tompkins, and yellow for combined. Recommendations are given to combined method if it leverages the recall of the threshold-based method with less than 1% drop in either precision or accuracy compared to both waveform-based and threshold-based methods. Otherwise, either waveform-based or threshold-based methods is recommended based on the recall.

Recall is the most critical factor to assess R-peak detection method [89]. With recall as the assessment standard, *Combined R-Peaks Detection* displays the best performance, which are 99.41% and 96.46% in records of normal and abnormal rhythms, respectively. The overall recall of Combined R-peak detection method is 97.41%, which beats 96.53% of the Pan-Tompkin's algorithm.

For precisions and accuracies, *Pan-Tompkins Algorithm* outperforms the waveform-based and the combined R-peaks detection methods with the precisions of 98.86% and 99.71% and accuracies of

97.98% and 95.73%. Nevertheless, the proposed waveform-based technique bears the competitiveness to detect R-peaks of normal rhythms records with a precision of 98.73%, a recall of 97.61%, and an accuracy of 96.47%.

Investigation of Individual Records

Besides the general metrics, we also investigate the most suitable algorithm for each record. We divide the recommendations into three groups: waveform-based recommended, Pan-Tompkins recommended, and combined method recommended. Recommendations are given to combined method if it leverages the recall of the threshold-based method with less than 1% drop in either precision or accuracy. Otherwise, either waveform-based or threshold-based methods is recommended based on the recall.

We observe that waveform-based method reveals more satisfactory results in records 108, 213, 231 and 232; it is because these four records have multiform low magnitude ECG and baseline wandering that prevent threshold-based methods from detecting the R-peaks [22]. We display the R-peak detection results of record 231 in Figure 2.6. Clearly, we can visualize that the low magnitude ECG successfully detected by waveform-based method but not threshold-based.

Conversely, we obtain the results of the Pan-Tompkins's algorithm outperforming the waveform-based method in records 107, 200, 201, 202, 203, 207, 217, 228, and 111 recommend Pan-Tompkins algorithm. This is because the threshold sensitivity is larger than the shape of the waveform, which is often observed in records of mixed rhythm types. We demonstrate the statement through the visualization of record 203 in Figure 2.7; since the R-peak is reversed, the waveform-based technique is unable to recognize it as a true positive R-peak.

Finally, the 35 unmentioned records are suggested to have R-peaks detected by the proposed combined algorithm. In summary, 81% of records from MIT-BIH arrhythmia database show superior

R-peak detection results through running the proposed combined and waveform-based R-peaks detection algorithms.

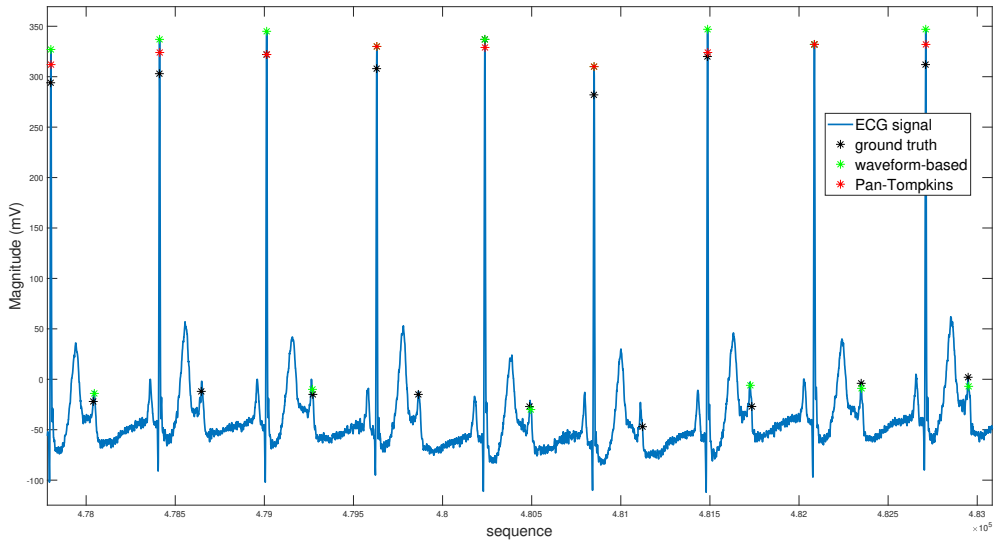

Figure 2.6: Demonstration of ECG (record 231) in favor of Waveform-based R-peak Detection Method; black for ground truth, green for waveform-based method, and red for Pan-Tompkins algorithm

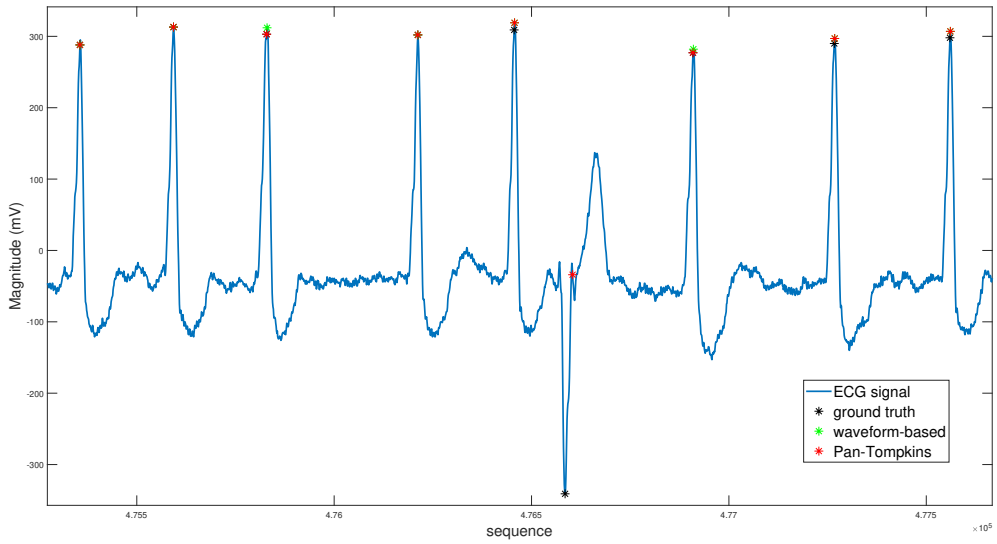

Figure 2.7: Demonstration of ECG (record 203) in favor of Threshold-based R-peak Detection Method; black for ground truth, green for waveform-based method, and red for Pan-Tompkins algorithm

Efficacy of the Proposed R-peak Detection Method

We show the efficacy of the proposed R-peak detection method in Table (2.4). Regarding R-peak detection recall, our proposed method presents the state-of-art performance, a recall of **97.41**%. When we compare our method to other studies with the same metric, a tolerance window of 10% averaged R-R interval, our combined method outperforms Pan-Tompkins' and Lurorenco *et al.*'s by around 1% performance [70] [83].

2.2.4 Conclusions

We describe an R-peak detection technique which leverages both waveform shape recognition and threshold sensitivity. We validate the algorithm with MIT-BIH Arrhythmia Database and demonstrate that the proposed algorithm is a state-of-the-art method with a recall of 97.41%. Also, we observe that the proposed method surpasses the Pan-Tompkins algorithm in **81%** of the records. Since R-peak detection is substantial in various cardiovascular disease diagnosis, we suggest to apply the combined R-peaks detection algorithm onto wearable devices.

2.3 Challenge in Heartbeat Detection of SCG

Vital sign monitoring is essential for health evaluation and enhance early detection of cardiovascular disease. Accessible accurate heart rate monitoring has the potential to decrease the global mortality rate and reduce the economic loss [14]. In addition to heart rates, real-time respiratory rate monitoring is substantial for the preventive care of the COVID-19.

In this study, we demonstrate adopting SCG data for both heart rate and respiratory rate monitoring. Our strategy allows the person to sit normally in a chair during monitoring. We show the efficacy of the proposed methodology in 20 young healthy adults.

2.3.1 Related Works

Numerous techniques have been proposed to monitor heart rates, including electrocardiography (ECG), photoplethysmography (PPG), ballistocardiography (BCG), and seismocardiography (SCG). ECG has been known to be challenging for an untrained user to implement in a domestic environment. Plus, ECG is not suitable for long-term usage due to the irritation caused by the electrodes. PPG is relatively easy to use, but intra-beat information is difficult to be extracted from PPG [24]. Additionally, PPG is easily corrupted by motion artifacts [30]. While BCG captures the morphology of the mechanical cardiac activity, it cannot be measured by a portable device [54]. SCG records the dorsal-ventral motion induced by the heart's contraction and ejection of the blood from the ventricles to the vascular tree. More importantly, SCG can be detected by placing an accelerometer on the chest. Nevertheless, removing the motion artifacts from SCG still remains as a challenging task.

Few studies report promising results using SCG to monitor heart rates [24] [102] [106]. In Wahlstrom *et al.*'s study [106], hidden Markov models (HMM) are applied. While in Tadi *et al.*'s research, Hilbert transform is performed on the SCG signal for heart rate estimation. State-of-the-art achievement

has been made by DMellos *et al.* with leveraging both SCG and gyrocardiography (GCG). Although successful heart rate monitoring is achieved, all require the humans lying on the bed during measurement.

2.3.2 Methodology and Experimental Design

We start with the description of our data collection method. Subsequently, we dive into the sensor data processing step. Following that, we present our heartbeat labeling and respiratory rate computation algorithm. Finally, we elaborate on how we quantify the performance of the proposed methodology.

Data Collection

This study was approved by the Jen-Ai Hospital-Joint Institutional Review Board. We recruited 20 young healthy volunteer to undergo the data acquisition process. All 20 subjects provided the written informed consent to participate in the study on their own will. The age of the recruited participants lies within $25-32$ years, and the gender distribution is 6 females and 14 males.

Table 2.5: Design of Experiments

Activities	sitting before & after a 3-minute exercise
Duration	each activity lasts for 3 minutes
Sensor Placement	at the bottom of the sternum
Description	participants wear the sensor throughout the whole experiment
Sensor	one tri-axial accelerometer
Measurements	accelerations, heart and respiratory rates

We summarize the experimental design in Table 2.5. All the participants went through two activities: sitting before and right after a 3-minute walking exercise. For each activity, the participant stays as still as possible in the same posture for three minutes with the wearable sensor placed on the body. As

for the walking exercise, the participants are asked to walk consistently and continuously at their normal pace for three minutes.

The collected data include body acceleration, heart rate, and videoed respiratory rate. Throughout the whole experiment, the acceleration data are measured with the sensor placed on the participant's sternum (as shown in Fig. 2.8). The acceleration sensor is MPU-6050 [20], and the data sampling rate is 150Hz. During the two sitting activities, the heart rate is measured using Rossmax MG150f. This blood pressure monitor was certified by European Society of Hypertension and clinically validated by British Hypertension Society with an A/A grade. All the data acquisition was completed by the same person, who was well trained by an experienced registered nurse to perform the measuring. Moreover, before the start of each activity, the same person inspected all the sensor to be well-functioning. The referenced respiratory rate was collected through video-recording the subject's normal breathing while sitting still in the chair.

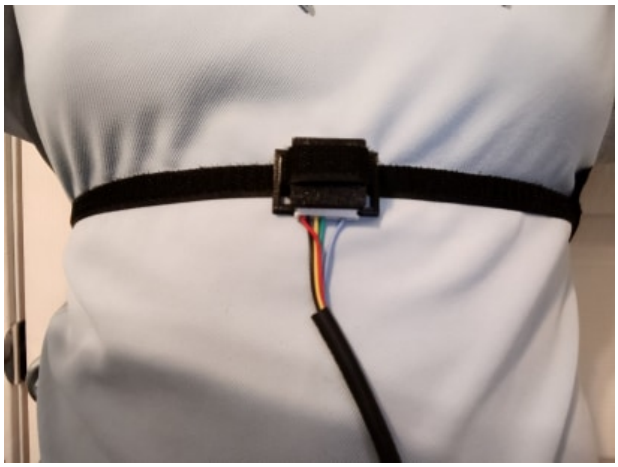

Figure 2.8: Accelerometer placed on the sternum.

Sensor Data Processing

We process and decompose the raw acceleration signals into two datasets - one set for heart rate and the other for respiratory rate computation. For heart rate, we develop a three-step signal processing

procedure. First, for vertical and dorsal-ventral acceleration, we remove the low-frequency motion artifact with a third-order Savitzky-Golay filter of 100ms span, which has been shown effective in removing running motion artifact in [84]. Next, we clean the high-frequency noise with a sixth-order low-pass Butterworth filter. We set the cut-off frequency at 35Hz, which is often used in ballistocardiogram and SCG extraction [20]. Finally, we smooth the data through interpolation with spline cubic curves at 750Hz. We demonstrate the raw and processed acceleration signals in Figures 2.9 and 2.10.

For breathing rate data generation, our proposed strategy is similar to the heart rate data processing. Different from heart rate dataset, we utilize only the dorsal-ventral acceleration signal for respiratory rate computation. In the first step, we take the residual of the Savitzky-Golay filtered heart rate data, which is a byproduct in the first step of the heart rate dataset construction. Subsequently, we remove the data offset, which is caused by the gravity and other constant motion effect. Next, we pass the processed data into a sixth-order low-pass Butterworth filter with a 0.5 Hz cutoff frequency. Eventually, we perform interpolation at 750Hz to smooth the data.

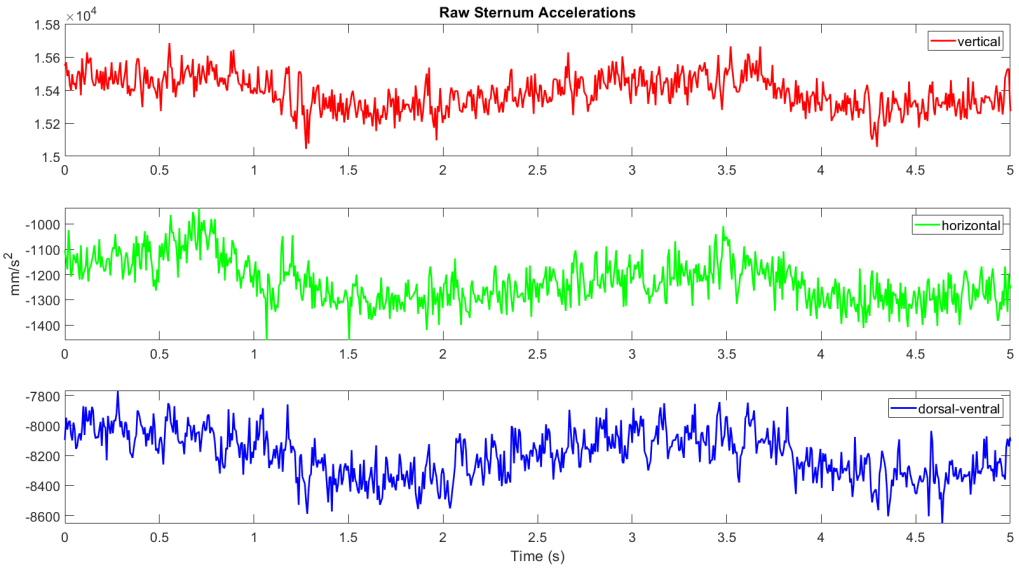

Figure 2.9: Demonstration of the raw acceleration data. Red: Vertical; Green: Horizontal; Blue: Dorsal-ventral

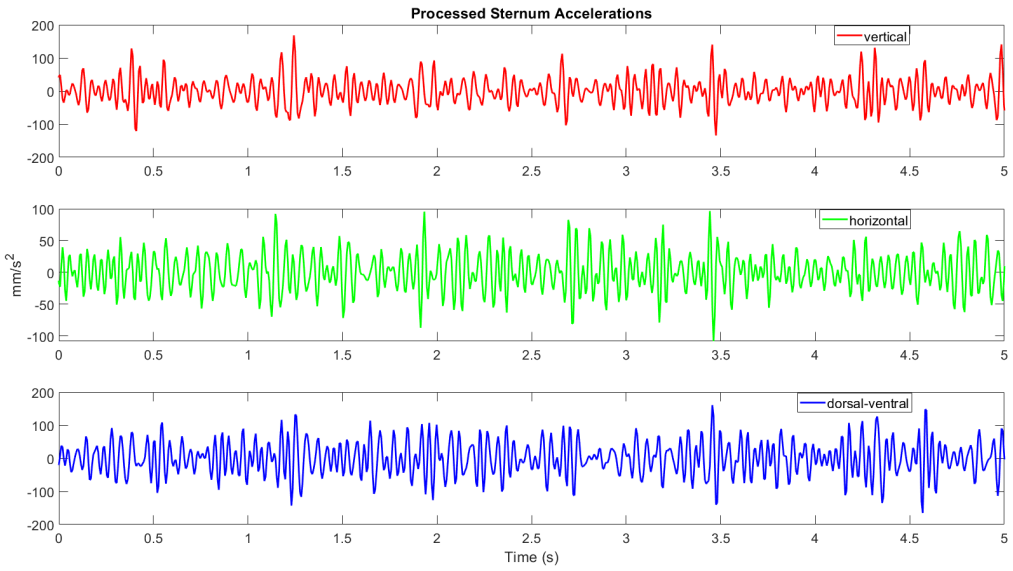

Figure 2.10: Demonstration of the processed acceleration data. Red: Vertical; Green: Horizontal; Blue: Dorsal-ventral

Heart Rate Computation

There are mainly five steps in our heart rate computation algorithm: 1) initial heartbeat labeling, 2) waveform-based heartbeat detection, 3) false positive heartbeat removal, 4) search-back for the missing heartbeat, and 5) heart rate estimation.

Initial heartbeat labeling: We first input the vertical and dorsal-ventral accelerations into our Heartbeat Labeling Algorithm (6) separately, and then we sift the peaks that deviate less than 10ms between vertical and dorsal-ventral accelerations as the valid heartbeats. The concept behind the algorithm is to identify the maximum peak in each empirically reasonable time window, which is also used in other heartbeat detection studies [20] [84].

Algorithm 6 Heartbeat Labeling Algorithm

Input: One-dimensional Acceleration Data D
Output: Heartbeat Peaks indices

```
Initialize the size of the sliding window
peaks = [ ]
current = 1s
delay = 0.5s
window = sampling_rate
while current + window < D.size do
    if peaks.is_empty then
        start = 1
        last = window
    else
        start = current + delay
        last = current + window
    end if
    current = start + D[start:last].max_index
    peaks.push(current-1)
end while
```

Waveform-based heartbeat detection: In this step, we utilize the waveform to correct the potential erroneous or miss-labeled heartbeats from Step 1, which is an approach shown to be effective in [41]. Based on the fact that noise-removed SCG is a quasi-periodic signal, we derive the envelope of the dorsal-ventral acceleration to capture the signal's intrinsic quasi-periodicity. Such envelope is determined using spline interpolation over local maxima separated by at least samples of 200ms. If there exists no heartbeat peak in an envelope, we mark the maximum peak as heartbeats. In another case, if there are multiple heartbeats detected in an envelope, we remove heartbeats inside this envelope.

False positive heartbeat removal: In this process, we remove the false positive heartbeats. We compute the heartbeats' intervals and consider only the interval lying within $0.5s - 1.2s$ as reasonable period. Subsequently, we calculate the mean and standard deviation (STD) of the selected intervals. Last, we remove the false positive heartbeats, which are those with intervals being less than $mean - STD$.

Search-back for the missing heartbeat: Some heartbeat peaks could have been falsely removed

in the previous process, and in this procedure, we search the missing heartbeats back. We identify the heartbeats as missing when we detect an interval of two consecutive heartbeats being longer than 1.2s. Next, we compute the number of heartbeats to be detected through peak-to-peak length estimation as we did in the previous step. Eventually, we enforce the number of heartbeats and label the missing heartbeats within the selected interval using Algorithm 6.

Heart rate estimation: We average out the interval length between every two consecutive heartbeats and round the number to obtain the heart rate of a subject.

Respiratory Rate Computation

We apply Fourier Transform and spectrum peak detection to conduct respiratory rate estimation. Once we acquire the respiration-oriented processed dorsal-ventral acceleration, we use Fourier Transform directly on the processed signal. Following that, we search the peak near 0.2 - 0.4 Hz on the frequency spectrum. Eventually, we treat the frequency that produces the largest peak near the specified range as the respiratory rate.

Performance Evaluation

We compare the estimations with the ground truth to evaluate the performance of the proposed algorithms. For heart rate, we calculate the accuracy by using the expression $\frac{estimation}{real\,heart\,rate} \times 100\%$. For respiratory rate, we first compute the true respiratory rate through the video-recording, and then adopt the accuracy metric to evaluate the algorithm. Moreover, we will visualize the different respiratory rates of the same subject in two different activities: sitting still pre-exercise versus post-exercise.

2.3.3 Experiment Results

We first exhibit the heart rate and respiratory rate accuracy of the 20 participants in Table 2.6. Following that, we present the visualization of the combined signals and respiratory rate in different activities. Finally, we compare the averaged accuracy with other existing SCG-based methods in Table 2.7.

Table 2.6: Results of the heart rate and respiratory rate estimation models

Subject	Accuracy of sitting heart rate (%)	Accuracy of post-exercise heart rate (%)	Accuracy of sitting respiratory rate (%)
1	98.9	98.9	≈ 100
2	100	78.7	≈ 100
3	98.6	98.7	≈ 100
4	95.7	90.3	≈ 100
5	96.6	99.0	≈ 85
6	100	98.6	≈ 100
7	100	100	≈ 100
8	100	96.8	≈ 100
9	100	98.7	≈ 100
10	100	98.7	≈ 80
11	100	100	≈ 100
12	91.7	100	≈ 100
13	98.6	100	≈ 85
14	93.0	93.1	≈ 100
15	100	98.7	≈ 100
16	98.8	96.7	≈ 85
17	98.5	100	≈ 100
18	98.7	100	≈ 100
19	100	98.8	≈ 100
20	96.5	100	≈ 100
overall	98.3	97.3	≈ 96.8

Efficacy of Heart Rate Estimation

According to the accuracy numbers in Table 2.6, we observe higher heart rate accuracy in sitting still compared to sitting after walking. In sitting still activity, every estimated heart rate reaches

an accuracy greater than 90%, and overall, the model accomplishes an accuracy of 98.3%. Conversely, sitting post-exercise generates larger error in average. One subject appears to have a badly estimated heart rate ($< 80\%$). Nevertheless, the heart rate estimation model still achieves an accuracy of 97.3% in post-exercise heart rate estimation. In addition, we display an example of labeled heartbeats in Fig. 2.11. From the figure, we can perceive the quasi-periodic heartbeat peaks labeled in the SCG with the devised algorithm.

Efficacy of Respiratory Rate Estimation

We present the accuracy of respiratory rate in Table 2.6, exhibit combined heartbeats and breathing acceleration in Fig. 2.11, and display the respiratory rates of two activities in Fig. 2.12. Promising results are observed from both the table and the figures. From the table, we are able to showcase that the model has successfully estimated sixteen out of twenty participants with nearly 100% accuracy. When comparing post-exercise respiratory rate to sitting still, we observe sharp increase in 95% of the participants in Fig. 2.12. Subject 4's respiratory rate does not surge in post-exercise activity, and it might be due to the fact that Subject 4 jogs on a regular daily basis.

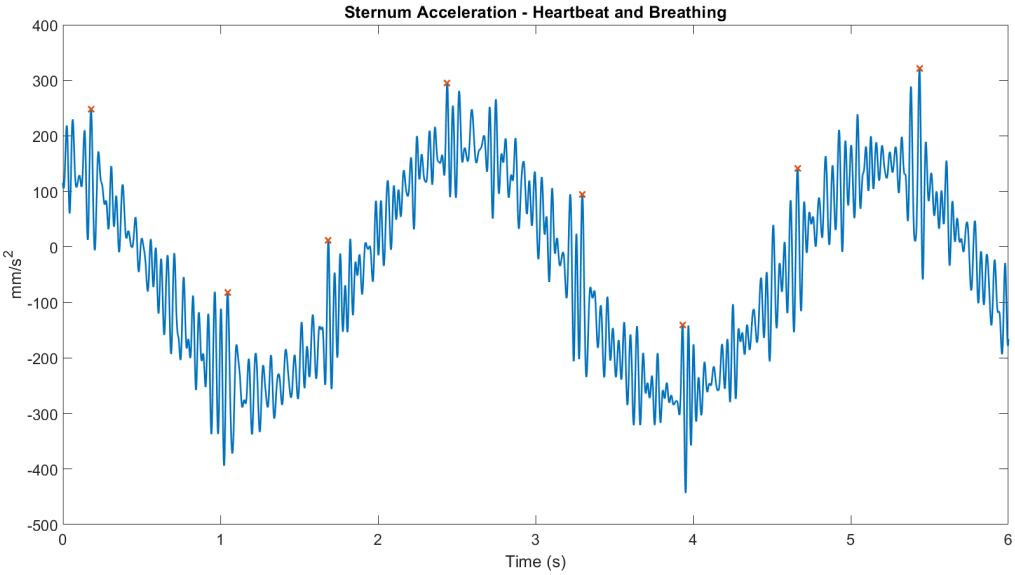

Figure 2.11: Visualization of both labeled heartbeats and breathing data. Red asterisks are the heartbeat peaks labeled by our algorithm.

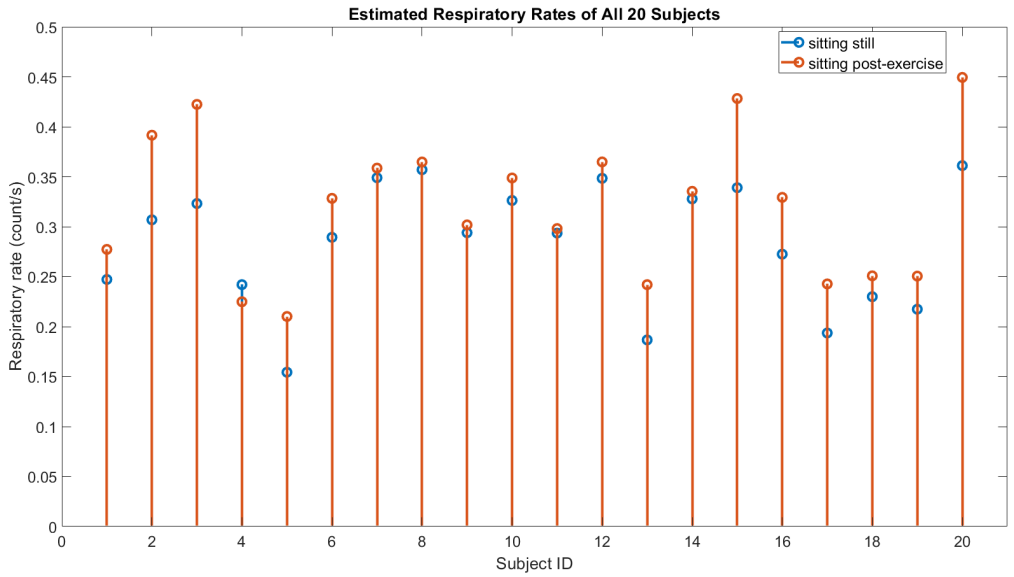

Figure 2.12: Visualization of respiratory rate in before versus after exercise. Blue circle stands for pre-exercise, and red circle for post-exercise.

Comparison with State-of-the-Art Works

Table 2.7: comparison of heart rate accuracy to state of the art

Method	Accuracy	Posture
Hidden Markov Model SCG [106]	98.5	Supine
Hilbert Transform SCG [102]	99.4	Supine
SCG + GCG [24]	99.8	Supine
Ours - multi-channel SCG	98.3	**Sitting still**
Ours- multi-channel SCG	97.3	**Sitting post-exercise**

We demonstrate the competitiveness of the proposed heart rate estimation model by comparing the results with the state-of-the-art works that also utilize SCG to compute heart rates. The highest accuracy is achieved by D'Mello *et al.* using SCG and gycocardiography together to estimate the heart rate [24]. However, all the existing studies require the participants to stay in a supine position. Such posture restricts the subjects from performing normal activity. In our proposed methodology, we successfully achieve $> 97\%$ accuracy in the sitting posture. More importantly, it does not matter whether the person is sitting still or panting in the chair due to the exercise.

2.3.4 Conclusions

We devise a seismocardiogram-based methodology that can accurately monitor the heart rate and respiratory rate. We demonstrate that such method is both ultra-convenient and cost-efficient in 20 young healthy participants, which requires only one sensor placing on the sternum. More importantly, the person can sit normally in a chair during monitoring. Based on the results, wearable SCG may be promising to apply in both daily and clinical monitoring.

2.4 Acknowledgments

Chapter 2 contains reprints of P.-Y. Hsu, P.-H. Hsu, H.-L. Liu, C.-T. Lin, H.-T. Chou, Y.-F. Tseng, and T.-H. Lee, "Star-ECG: Visualization of Electrocardiograms for Arrhythmia and Heart Rate Variability", *Annual International Conference of the IEEE Engineering in Medicine and Biology Society (EMBC)*, 2021; P.-Y. Hsu, P.-H. Hsu, T.-H. Lee, and H.-L. Liu, "Heart Rate and Respiratory Rate Monitoring Using Seismocardiography", *Annual International Conference of the IEEE Engineering in Medicine and Biology Society (EMBC)*, 2021; and P.-Y. Hsu, and C.-K. Cheng, "R-peak Detection Using a Hybrid of Gaussian and Threshold Sensitivity", *Annual International Conference of the IEEE Engineering in Medicine and Biology Society (EMBC)*, 2020.

I would like to thank my coauthors Chung-Kuan Cheng, Hung-Tao Chou, Po-Han Hsu, Tsung-Han Lee, Chi-Te Lin, Hsin-Li Liu, and Yu-Fang Tseng for their suggestions and clarifications on our published works.

Chapter 3

Computational Methodologies for ECG Arrhythmia Classification

This chapter presents three fully automated arrhythmia classification programs. First, we provide a biologically reasonable arrhythmia classification algorithm for single lead ECG, and the program has been tested on the MIT-BIH Arrhythmia Dataset [79]. Subsequently, we exhibit another physiologically reasonable arrhythmia classifier using *Star-ECG*, which is introduced in Chapter 2. Last, we demonstrate a competitive 12-lead ECG arrhythmia classification program, which was verified on six datasets crossing Asia, Europe, and North America continents with a total of over 40,000 arrhythmia patients. The program was ranked top 7% in 2020 Computing in Cardiology Challenge.

3.1 Challenge in Single Lead ECG Arrhythmia Classification

Arrhythmia is a serious cardiovascular disease due to its high prevalence and associated high mortality [9]. Given its severity, real time monitoring and early diagnosis of arrhythmia are critical in

clinical practice. In this end, electrocardiogram (ECG) has become a popular arrhythmia diagnostic tool, as ECG is non-invasive and easily accessible. According to the Association for the Advancement of Medical Instrumentation (AAMI), ECG signal of arrhythmia is classified into five types: non-ectopic (N), supraventricular ectopic (S), ventricular ectopic (V), fusion (F), and unknown (Q). Each class requires different treatment [75], and therefore, correctly identifying the arrhythmia types is essentially important before any treatment administered.

In this section, we present a waveform-based signal processing (WBSP) technique. WBSP is inspired by Gaussian-modeled ECG proposed by McSharry *et al.* [77]; in [77], an ECG beat is constructed with Gaussian mixtures and limit cycle. We demonstrate that WBSP can contribute to achieving:

1. Extracting features for machine learning-based classifiers without explicitly identifying P, Q, R, S, T waves of an ECG beat

2. Allowing balanced arrhythmia labels trained in deep learning-based classifiers and still reaching satisfying results

3. Incorporating limit cycle concept into DNN

4. Providing intrinsic data-oriented interpretation for clinical diagnosis

We organize the structure as follows. In subsection 3.1.2, we first introduce the database used and then elaborate on WBSP. Next, we demonstrate the procedure of training machine learning-based and deep learning-based classifiers. In the end of subsection 3.1.3, we describe how the performance of the classifiers are evaluated. Then in the same subsection, we present our results and compare them with other reported works. Last, we conclude our work in section 3.1.4.

3.1.1 Related Works

Numerous arrhythmia computer-aided diagnosis (CAD) algorithms have been proposed. Most of these CAD tools rely on hand-crafted morphological features extraction such as identification of P-wave, QRS complex, T-wave or frequency analysis [25] [76] [115]. Such approach reveals to be error-prone on separate datasets where ECG fiducial points are difficult to recognize [2].

Unlike morphological feature extraction CAD, deep learning-based approach has become popular recently owing to its self-learning ability. Explicit features are not required to train a deep neural network (DNN) [2] [42] [113]. However, interpretability and imbalanced labels still remain to be challenges in deep learning-based CAD for arrhythmia [39].

3.1.2 Methodology and Experimental Design

Database

We selected MIT–BIH arrhythmia database [79] from publicly available PhysioNet [36] to validate our waveform-based arrhythmia classifiers. The data includes a total of 48 records sampled at 360 Hz, and all 48 records contain ECG data of 30 minutes duration. For all the records, we chose lead II signal for analysis if available; otherwise, we selected the signal from the first channel for experiments.

Waveform-based Signal Processing

There were four steps in WBSP procedure as demonstrated in Figure 3.1: low-pass filtering, local minima search, removal of drift, and curve fitting. First, we passed the raw ECG signal into a low-pass filter with 35 Hz cutoff frequency. Next, we found the local minima of the filtered ECG signal. To be more precise, the start and the end of the signal were both considered as local minima. Subsequently, we used cubic spline to connect the local minima found in the previous step and subtracted the piece-wise

cubic spline curve from the filtered ECG signal so as to remove the drift. Every local minima data-point became zero after the drift removal, and we refer these zero valued local minima as *knots* in the rest of the paper. Last, we fit each curve between every two neighboring knots with a Gaussian model as expressed in (3.1).

$$G(t) = a \cdot e^{-((t-b)/c)^2} \tag{3.1}$$

We recorded the area and the ratio of the curve as defined in (3.2) and (3.3) for R-peak detection.

$$area := \sqrt{|a|} \cdot |c| \tag{3.2}$$

$$ratio := |\frac{a}{c}| \tag{3.3}$$

According to McSharry *et al.* [77], Gaussian curves are suitable to model the P, QRS, and T waves of ECG signals; therefore, we chose Gaussian curves to parameterize the curve between each two neighboring knots.

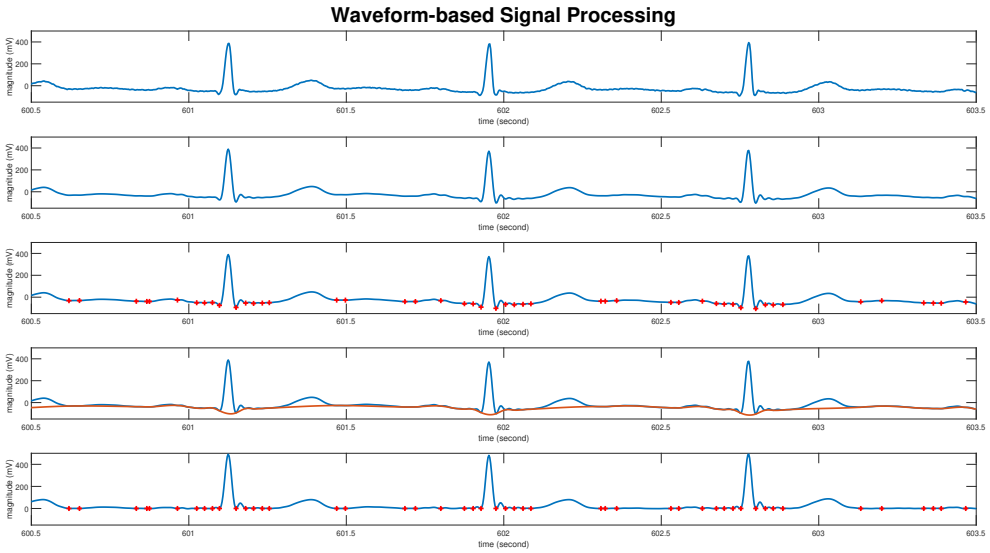

Figure 3.1: Demonstration of Waveform-based Signal Processing Method. Top row shows the raw ECG signal. Intermediate rows display the low-pass filtered signal, searched local minima in red cross, and the cubic spline-connected drift to remove in orange. The last row displays the processed signal for Gaussian fitting.

WBSP for Arrhythmia Classification

We leverage the WBSP processed ECG data to accomplish both machine learning-based and deep learning-based arrhythmia classification tasks.

Machine Learning Classification

We elaborate on the feature extraction and classifiers selection for machine learning-based approach.

Extract Features for Machine Learning: We selected two types of features based on the WBSP method: Gaussian and cubic spline. Gaussian features are the parameters (a, b, c) defined in Eq. (3.1), *area* and *ratio* expressed in Eqs. (3.2) and (3.3), and *coefficient of determination* R^2, which interprets how well the Gaussian model fits the curve. Cubic spline features contain *Values of the two knots*, *integral of the cubic spline*, *the peak value of the cubic spline*, and *the time intervals between the two knots and the*

centered peak. In WBSP, the filtered signal is decomposed into Gaussian parameterized curves and cubic spline drifts. For this reason, we selected the features from these two types of waveform.

Figure 3.2 displays one ECG beat sample to have features extracted from. For each labeled ECG beat, we empirically chose the features from the curves enclosed by twenty knots with the annotated R-peak positioning as the centered curve. That is, each ECG beat has nine curves preceding the R-peak, nine curves succeeding the R-peak, and one center curve, which generates a total of $(6+5)\times(9+1+9)+1=$ 210 features for one ECG beat.

Select the Training Classifiers: The experimented classifiers were optimizable ensemble (ENS), random forests (RF), linear and quadratic kernel support vector machines (SVM), k-nearest neighbors (k-NN), and boosting classifiers.

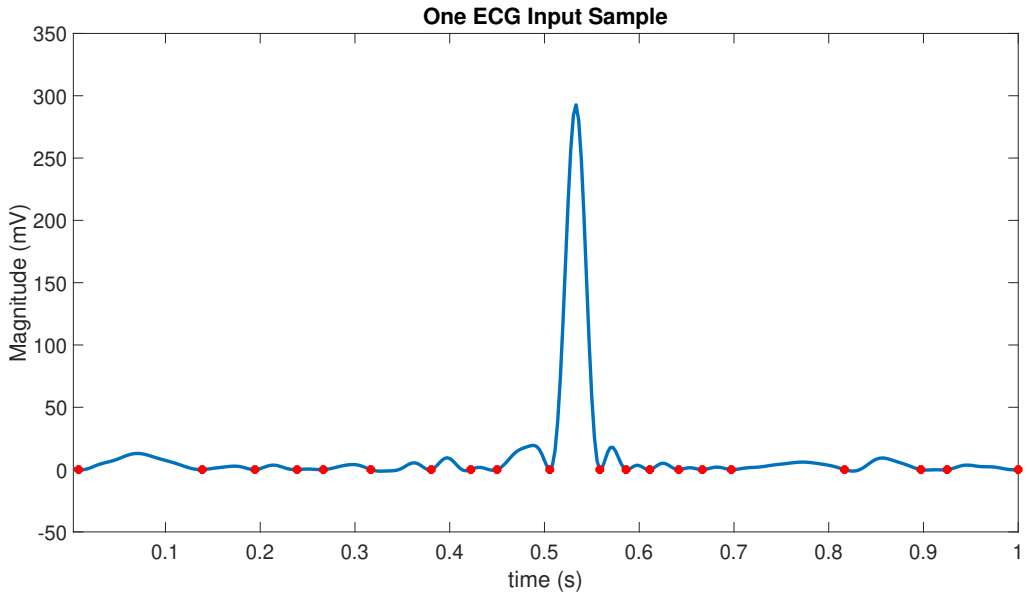

Figure 3.2: Demonstration of one ECG input sample. The blue line is the ECG signal, and the red dots are the knots. QRS complex stands in the center, and each side has nine curves enclosed by ten knots.

Deep Learning Classification

We demonstrate how we construct the input image and neural network architecture for the deep learning-based technique.

Prepare Data for 2D-CNN: As shown in Figure 3.3, we transform 1D ECG data into 2D images for deep learning to incorporate limit cycle and continuity concepts. The scheme is to employ the *knots* generated by WBSP. We also selected each ECG beat with 20 *knots* enclosed as we did in the machine learning approach. Afterwards, we projected the ECG data onto a circle with the two endpoints neighboring each other. That is, we view the ECG beat as a limit cycle, which is also a technique adopted by McSharry *et al.* [77]. For each ECG beat, we generated two circled images: one for WBSP processed curve, and the other for cubic spline drift.

Build the Deep Neural Network: Our DNN architecture is shown in Fig. 3.4. The infrastructure of the proposed DNN is based on AlexNet [64]. AlexNet stacks layers of convolutional neural network (CNN) to enable recognizing patterns of different scales in an image; furthermore, layers of operations such as pooling and normalization are often inserted in between two CNNs.

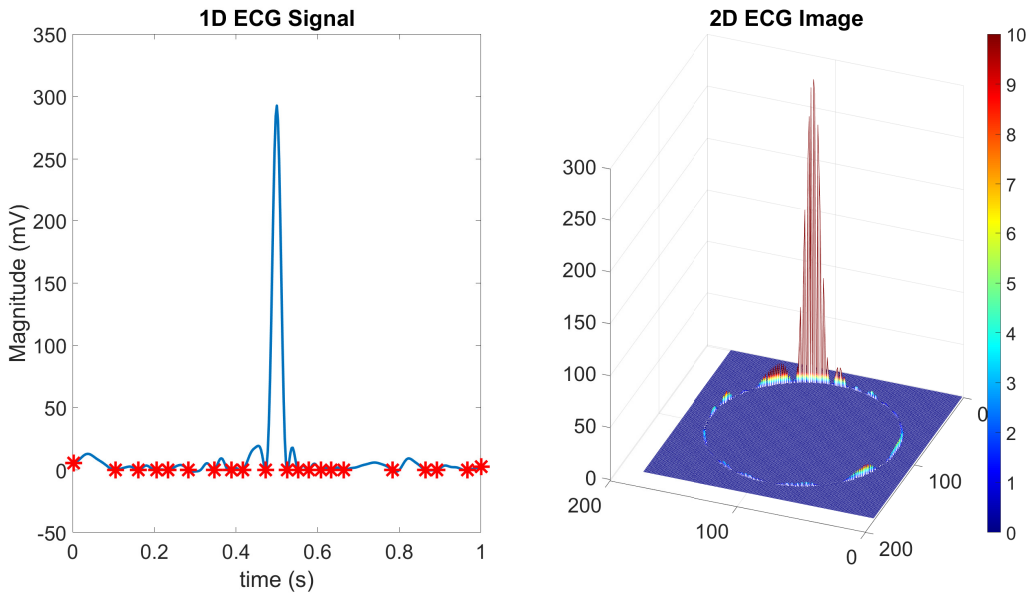

Figure 3.3: Illustration of transforming a 1D ECG signal to a 2D image to train a deep neural network arrhythmia classifier; left subplot displays one ECG beat and marks the knots as red stars; right subplot demonstrates the 2D ECG image as an input sample to the deep neural network

In our design, we have a DNN of 30 layers. The first layer is an input layer of size $73 \times 73 \times 2$, and the last layer is the classification output. As shown in Fig 3.4, the dimensionality of the input changes at the 2^{nd}, 10^{th}, 15^{th}, 22^{nd}, 25^{th}, and 28^{th} layers, at which the former are CNN and the latter are fully connected (FC) layers. Following the input is a CNN layer with 32 filters of size 3×3. From the 2^{nd} to the 10^{th} layers, the operations include ReLU, normalization, max pooling, grouped convolution (GC) of 32 filters, and another repeated procedure exclusive of the GC. The 10^{th} layer is a CNN layer with 48 filters of size 5×5. Subsequently, the operation layers contain ReLU, GC of 48 filters, and another repeated procedure. At the 15^{th} layer, it is a CNN with 48 filters of size 7×7. Starting from the 16^{th} to the 21^{st} layer, it includes a series of operations without changing the activation dimensions: ReLU, GC of 48 filters, ReLU, GC of 48 filters, ReLU, and max pooling. From the 22^{nd} to the 29^{th} layers, they consist of typical classification structures. We design the numbers of activation units of FC at the 22^{nd}, 25^{th}, and 28^{th} layers as 512, 128, and 5. In between each FC layers are ReLU and dropout at 0.6. At the 29^{th} layer,

softmax is used to compute the classification result and generate the output at the 30^{th} layer.

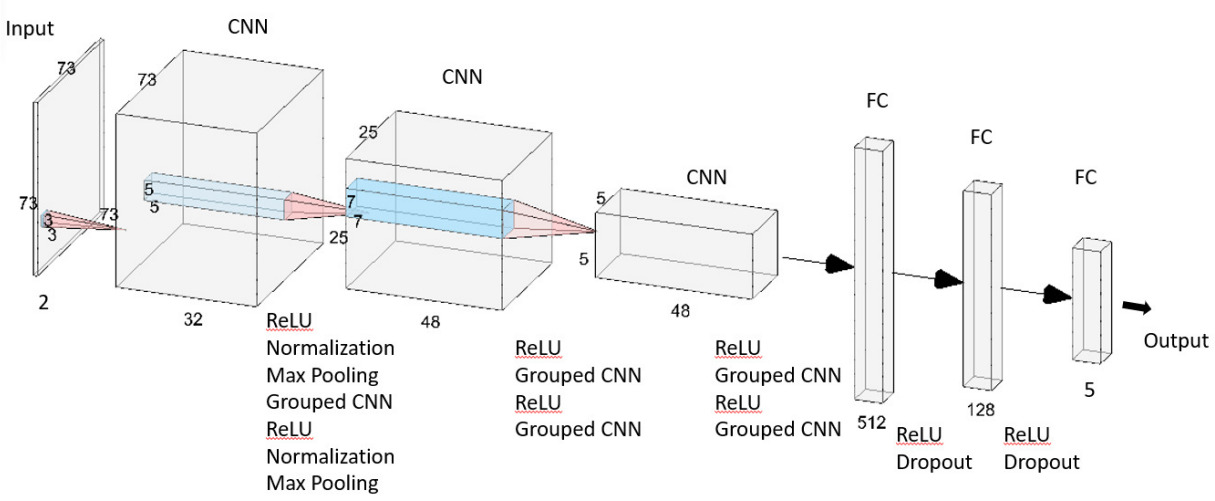

Figure 3.4: Diagram of the architecture of the deep neural network. The numbers represent the dimensions of the data in the network.

We trained the DNN with stacks of transformed ECG images as input and their corresponding classification labels as output. For the input, we set the image size as 73×73. The whole training required twenty epochs and a mini-batch size of 100 in each epoch. Random shuffling was included. The DNN training was run with a single GeForce GTX 1050 graphics card on MATLAB 2019B.

Data Partition and Performance Evaluation

Table 3.1: Summary of Classified Heartbeat Types

Hearbeat Type	AAMI	Total #	Training (%)
Normal	N	74625	10%
Left bundle branch block	N	8037	40%
Right bundle branch block	N	7217	40%
Atrial premature	S	2529	40%
Aberrated atrial premature	S	149	40%
Nodal (junctional) premature	S	83	40%
Premature ventricular contraction	V	7099	40%
Fusion of ventricular and normal	F	800	40%
Ventricular flutter wave	V	472	40%
Atrial escape	N	16	40%
Nodal (junctional) escape	N	229	40%
Ventricular escape	V	106	40%
Paced	Q	6984	40%
Fusion of paced and normal	Q	977	40%
Unclassifiable	Q	33	40%

We conducted experiments by using the proposed machine learning-based and deep learning-based classifiers to classify the 15 ECG beat types into 5 categories N, S, V, F, Q according to ANSI/AAMI EC57 of arrhythmia classification [10]. Table 3.1 lists the 15 beat types and their corresponding categories. Class *N* includes normal, left bundle branch block, right bundle branch block, atrial escape, and nodal (junctional) escape beats; class *S* contains atrial premature, aberrated atrial premature, and nodal (junctional) premature; class *V* consists of premature ventricular contraction, ventricular flutter wave and ventricular escape; class *F* is composed of fusion of ventricular; class *Q* includes paced, fusion of paced and normal, and unclassifiable.

To fulfill the classification task, we split the data by following similar procedure recommended

by [116] to sample the ECG beats due to the imbalance of the data. We randomly sampled 10% of normal beats and 40% of other types of heart beats to train our classifiers. To be more specific, we trained our models with 19.5% of data and run the testing on 80.5% of data.

We evaluated the performance of the proposed waveform-based arrhythmia classification method with accuracy and sensitivity, which are both commonly adopted metrics in classification tasks. For each arrhythmia type, sensitivity is defined as the ratio of the number of the correctly labeled class (true positives) over the total of the specified class (true positives + false negatives). Accuracy is expressed as the number of correctly labeled classes divided by the summation of the evaluated ECG beat number. In addition to the conventional performance evaluation, we observed the feature importance to leverage the application of WBSP.

3.1.3 Experiment Results

Performance of the Classifiers

Table 3.2: Accuracy and Sensitivity of Arrhythmia Classification

work	Acc	S_N	S_S	S_V	S_F	S_Q
Acharya *et al.* [2] 1D-CNN	94.0%	91.6%	**89.0%**	94.1%	**95.2%**	97.4%
Yang *et al.* [113] PCAnet	97.9%	**99.6%**	71.3%	87.5%	75.0%	98.4%
Our ML	**98.8%**	99.3%	86.6%	**96.3%**	75.2%	**98.6%**
Our DL	97.8%	98.6%	76.2%	**95.3%**	70.5%	97.7%

We summarize the classification results of ours and other reported research work evaluating on the same dataset (including paced beats) in Table (3.2). Our best machine learning-based classifier is

the optimizable ensemble classifier, which reaches an overall accuracy of 98.8%. Other experimented machine learning-based classifiers arrive at an accuracy of 97.6% for RF, 96.5% for quadratic SVM, 95.2% for boosting, and 94.2% for kNN. Referring to the deep learning-based method, our classifier achieves an overall accuracy of 97.8%.

Both of our proposed classifiers are competitive with other published works as displayed in Table 3.2. Regarding the overall accuracy, our ensemble classifier has the best performance. As to the sensitivity, both classifiers outperform Yang *et al.* [113] and Acharya *et al.* [2] in class V, and the ensemble classifier even reaches the best sensitivity in class Q. Moreover, both classifiers present fair sensitivities in the other three classes. By fair, we mean the sensitivities achieved surpass (class N, S, and F) one of the two published works.

Important Features in Arrhythmia Diagnosis

Figure 3.5 demonstrates the feature importance of Gaussians computed from our trained ENS classifier, and the resulting features can further support the clinicians in arrhythmia identification. We are able to visualize four features that play significant roles in arrhythmia classification. Two of them originate from QRS curve: goodness-of-fit R^2 and ratio; and the other two features derive from QRS left neighboring curve: the width and area parameterized by a Gaussian. The observations imply that the shapes of possible P-wave (or the wave preceding QRS complex) and QRS complex significantly affect the arrhythmia classification results.

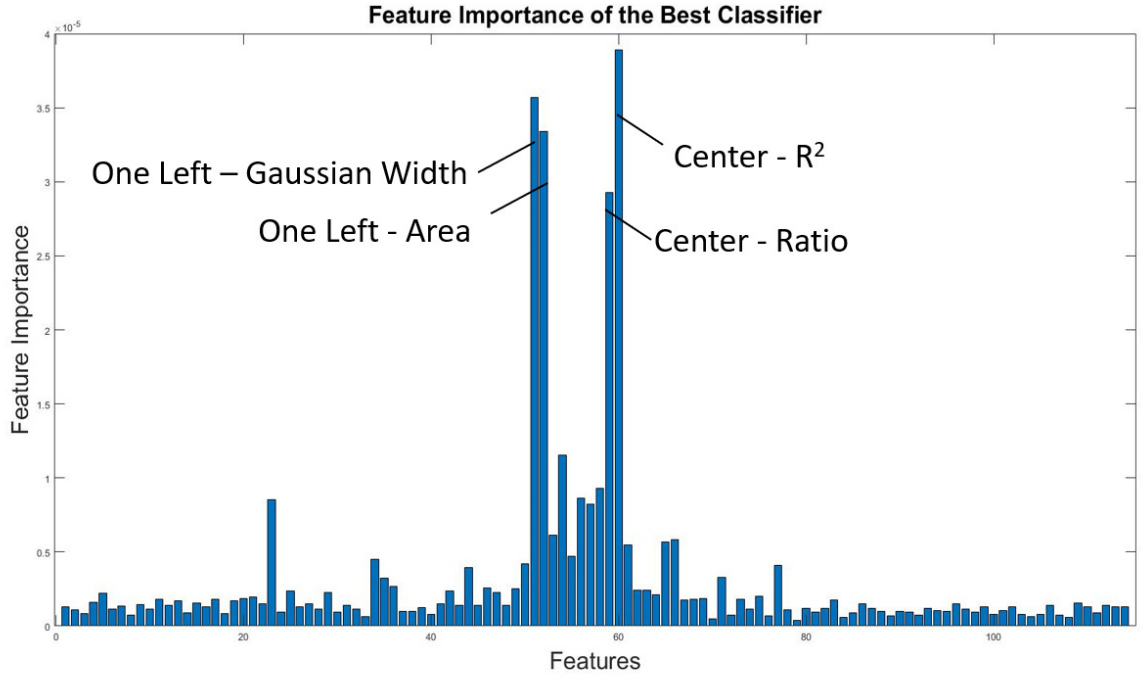

Figure 3.5: Illustration of the feature importances of the best classifier

3.1.4 Conclusions

We propose a waveform-based signal processing method for electrocardiogram. More importantly, we demonstrate how WBSP can be applied to devise machine learning-based and deep learning-based arrhythmia classifiers. In arrhythmia classification tasks, we achieved one of the state-of-the-art performances with an accuracy of 98.8%, sensitivity of 96.3% in class V, and sensitivity of 98.6% in class Q. In addition, we found the key waveform parameters that contribute to arrhythmia classification with the proposed WBSP method. We intend to explore WBSP on different biosignals in the future.

3.2 Challenge in Long Rhythm ECG Arrhythmia Classification

Multiple machine/deep learning-based models have been proposed for ECG data arrhythmia classification [2] [40] [113]. However, most of these models treat single heartbeat as the data input, which can be error-prone due to the loss of beat-to-beat information or low ECG data quality on certain heartbeats [117].

In this end, we leverage our novel ECG visualization tool, *Star-ECG*, to meet this challenge by integrating our trained long rhythm ECG arrhythmia classifier into the tool.

3.2.1 Related Works

A great number of computer-aided diagnosis (CAD) programs have been suggested for arrhythmia classification. The majority of these CAD algorithms rely heavily on hand-crafted morphological ECG waveform features, namely, P-wave, QRS complex, T-wave, or frequency analysis [25] [76] [115]. Such approach reveals to be error-prone since ECG fiducial points are difficult to recognize in several datasets [2].

Unlike hand-crafted feature extraction CAD, deep learning techniques have gained the popularity in recent years owing to its self-learning ability. Training a deep neural network exempts the need of explicit feature construction [2] [40]. Several research studies have shown state-of-the-art arrhythmia classification performance achieved by the CNN models [2] [40] [90]. According to these studies, CNN models can successfully learn and recognize the patterns of differentiated arrhythmia types.

3.2.2 Methodology and Experimental Design

We use neural network models to perform arrhythmia rhythm-type classification. Our neural network architectures include ResNet18 [38] and AlexNet [64]. The inputs of the model are the ECG

images generated by *Star-ECG*; the outputs are the corresponding arrhythmia labels. To address the imbalance issue in the dataset, we increase the data size by performing rotation. For an ECG image of P heartbeats, we augment $P-1$ images by rotating the image with angles $2\pi K/P$ rad, in which $K \in \mathbb{N}, 1 \leq K \leq P-1$. Such technique assumes that the pattern of ECG image is invariant after rotation, which is reasonable because our ECG image is generated in a rotation fashion.

We ran our experiments on the MIT Arrhythmia Database (MITDB) [79], which is publicly available from the PhysioNet database [36]. The MITDB dataset contains 48 two-channel 30-minute recordings of ECG measured from 47 subjects (25 male and 22 female) diagnosed of arrhythmia. Only one subject has two recordings. Every recording is sampled at a frequency of 360 Hz with 11-bit resolution over a 10 mV range. In our experiments, we consider Lead II recording of each subject.

We conduct all the experiments with MATLAB R2019B. For model inputs, we resize all the ECG images to 80×80 to train the models. For training process, we use adam optimizer [61] with learning rate 0.0001 and shuffle data in each epoch. Based on the size of the dataset, we set the mini-batch size to 20. We found that 20 epochs were enough for the models to converge, so we set 20 as the number of the epoch for our experiments.

3.2.3 Experiment Results

We use overall accuracy and sensitivity of each arrhythmia class to evaluate the classification performance as summarized in Table 3.3. We show that the proposed technique is competitive with other published work. Our ResNet18 model achieves the highest overall accuracy. In addition, it outperforms the state of the art in normal rhythm, supraventricular tachycardia, ventricular bigeminy, and ventricular trigeminy classes. Ventricular flutter has been successfully classified by our ResNet18, AlexNet models, and Yildirim *et al.*'s model [117]. Based on the good classification results, we consider the proposed ECG

image technique combining with the ResNet18 model as a promising arrhythmia classification tool.

Table 3.3: Arrhythmia classification performance of the state of the art and the proposed approach. Rhythm type is abbreviated as the annotations used in the MITDB dataset.

Method	Sensitivity (%)												Accuracy
	N	BII	PREX	SVTA	AFL	AFIB	P	B	T	IVR	VT	VFL	(%)
CNN [117]	94.4	**100**	**100**	50	**100**	**94.4**	**100**	66.7	0	**100**	**50**	**100**	89.4
ResNet18 [Ours]	**95.0**	88.2	42.9	**100**	41.2	86.1	98.1	**86.2**	**66.7**	0	33.3	**100**	**92.6**
AlexNet [Ours]	92.7	17.6	0	80.0	5.9	74.8	93.3	20.7	16.7	0	0	**100**	85.8

3.2.4 Conclusions

In this study, we propose *Star-ECG* for visualizing heart rate variation and classifying different arrhythmia types. The proposed arrhythmia classifier shows competency to the state of the art. We believe the easy-to-read *Star-ECG* image can aid both clinicians and patients to carry out early diagnosis of arrhythmia.

3.3 Challenge in 12-Lead Multi-label ECG Arrhythmia Classification

In participation of the PhysioNet/Computing in Cardiology Challenge 2020, we developed a novel computational approach for efficiently identifying cardiac abnormalities from 12-lead electrocardiogram (ECG) data. The developed methodology is composed of three processes: selecting representation, generating features, and predicting outcomes. We proposed a cache-inspired method to select a 12-lead ECG heartbeat representation. Moreover, we devised a physiologically interpretable feature generator for segmented 12-lead ECG signals. For multi-label arrhythmia classification, we innovated an efficient arrhythmia outcome prediction procedure that is adaptable to ECG data of variant lengths. Our team, JuJuRock, received a score of 0.402 using 5-fold cross-validation on the full training data and a score of 0.244 on the final full test data. Team JuJuRock ranked 16^{th} out of the 41 teams that participated in this year's Challenge.

3.3.1 Related Works

Arrhythmia is a substantial cardiovascular disease since it has been reported to correlate with high prevalence and associated mortality [11]. Different arrhythmia types have different mechanisms and require the appropriate interventions for successful treatments. The electrocardiogram (ECG) is an essential tool for screening and diagnosing cardiac electrical abnormalities [62]. Online cardiac activity ECG monitoring and early diagnosis of arrhythmia are critical in clinical practice. To reduce the time-consuming manual arrhythmia labeling, several computer-aided-diagnosis (CAD) tools have been proposed [2] [40].

However, a majority of these CAD tools have not been verified on multiple datasets. Another drawback of these CAD models is their power in diagnosis - they focus on single-label diagnosis instead of multi-label cardiac abnormalities identification.

3.3.2 Methodology

To develop an automated program that addresses the aforementioned issues, we participate the PhysioNet/Computing in Cardiology Challenge 2020, which focused on automated, open-source approaches for classifying multi-label cardiac abnormalities from 12-lead ECGs [6]. Our best entry in the Challenge applied boosting classifier to identify the cardiac abnormalities. Moreover, we deliver the computational approach that contributes to:

- Generating 12-lead ECG heartbeat representation;
- Producing physiologically reasonable feature maps;
- Making efficient cardiac abnormalities identification.

We formulate the multi-label arrhythmia classification problem into diagnosing each arrhythmia class with a binary classifier. The binary classifier's training process is illustrated in Figure 3.6. First, we select the appropriate datasets to include in the training. Next, we process and segment a representative heartbeat from each patient. Subsequently, we generate the amplitude and timing feature maps from each heartbeat segment for classifier training. Following the feature generation, we train the binary classifiers with different deep learning (DL) and machine learning (ML) models. Once the classifiers are trained, we experiment with these models and optimize the parameters in our devised arrhythmia decision algorithm.

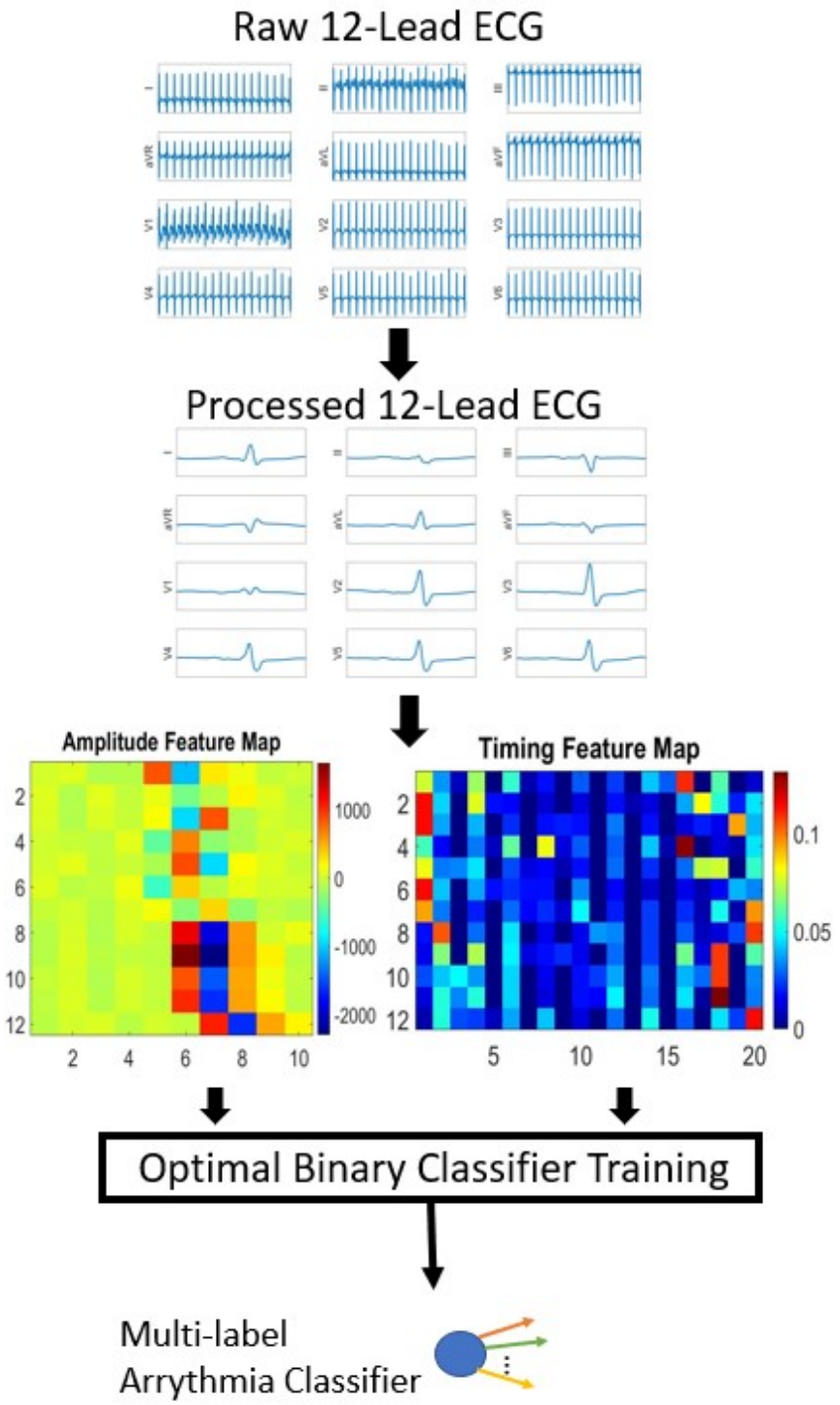

Figure 3.6: Flowchart of training the proposed multi-label arrhythmia classifier.

Dataset Selection

Six datasets are generously provided as the training candidate, and four out of six were chosen to be included in our model training. The four selected datasets are Georgia, CPSC, CPSC_2, and PTB-XL 12-Lead ECG databases. Such dataset selection is made based on three reasons: **1) sample size**, these four datasets cover the majority of the cases and could possibly represent the data distribution in the testing set; **2) data length**, variant data length, from five seconds to several minutes, are lying within the chosen datasets; **3) signal quality**, the signal-to-noise ratio (SNR) is relatively high in the selected four datasets compared to the two unselected ones. Furthermore, given the 27 evaluated classes in the challenge, only the data from the patient diagnosed as at least one of the 27 classes is sifted.

Data Segmentation

We developed a heartbeat segmentation algorithm to transform each patient's raw ECG signal into one representative heartbeat data. Such algorithm consists of four steps: data cleaning, R-peak detection, heartbeat segmentation, and representation selection. In Figure 3.6, we demonstrate the raw and the processed 12-Lead ECG data.

First, we clean the raw ECG data with a Butterworth low-pass filter and a smoothing function channel-wisely. The Butterworth filter has an order of 12 and 50Hz cutoff frequency. The smoothing function adopts the moving average strategy with 10ms window span.

In the second step, we detect the R-peaks in the cleaned ECG data. All the R-peaks detection is carried out on Lead II data. For the majority of patient samples, we run the famous Pan-Tompkins algorithm to identify the R-peaks; for the few corner cases, we take on the heartbeat detection method targeted at noisy physiological signal as applied in Hsu *et al.'s* work [20] to resolve the issue.

Once we finish labeling the R-peaks of one patient, we chop down every ECG heartbeat into 1-

second long frame and concatenate the frames into a tensor. Every 1-second frame has the channel-wise R-peak located at the center. Supposed that N number of heartbeats is considered, then the tensor will have the dimension of $12 \times f_s \times N$, where f_s symbolizes the ECG sampling rate. To be more specific, we do not consider the head and the tail of the heartbeats into the tensor. Because the SNR is typically low at the endpoints of the signal and the duration of the ECG heartbeat are likely to be less than one second.

At the last step, we employ the clustering method and similarity metric to select the representative one-second ECG heartbeat. For each patient, we congregate the ECG frames into at most three groups and recognize the frame lying within the largest group as the representative.

The clustering approach is inspired by the cache updated rule. At the beginning, we construct a cache of three entries, and each entry contains five blocks. Next, we follow the least-recently-used rule to update our cache, which is a frequently utilized technique in computer architecture. We assign a newly visited ECG frame to an existing cache block if the ECG frame has sufficiently high similarity with the frames in the entry, or if there is an empty entry to be filled with; otherwise, we move on to the next ECG frame. Eventually, we select the block data that stores the most recent ECG frame in the largest group as the representation.

As for the similarity metric, we borrow the structural similarity index (SSIM) defined in Wang *et al.'s* study [109]. The SSIM expression is

$$SSIM(x,y) = \frac{(2\mu_x\mu_y + c_1)(2\sigma_{xy} + c_2)}{(\mu_x^2 + \mu_y^2 + c_1)(\sigma_x^2 + \sigma_y^2 + c_2)}, \tag{3.4}$$

where $c_1 = (0.01L)^2$, and $c_2 = (0.03L)^2$. Inputs x, y are the two ECG frames; μ_x, μ_y are the averages of the two input frames; σ_x, σ_y, and σ_{xy} are the variances of frame x, frame y, and the covariance of the two frames x, y. L is the range of the ECG voltage values. In this work, frames x and y represent the two

ECG frames to be compared with, and we empirically set the SSIM threshold as 0.3 to consider two ECG frames belonging to the same group.

Feature Map Generation

We invented a novel physiology-inspired feature generator that is able to efficiently produce the feature maps of an arbitrary ECG frame. We incorporate the knowledge of saliency into our feature generation model to quantify the P-wave, QRS-complex, and T-wave relevant geometry on two feature maps. One feature map renders the amplitude features, while the other characterizes the timing information. We present our amplitude and timing feature generation Algorithms [7,8] as follows:

Algorithm 7 Amplitude Feature Generation

Input: 1-second 12-Lead ECG Data, K
Output: Amplitude Feature Map Amp_Map

Initialize Amp_Map as a matrix of size $12 \times K$
for $ch = 1 \rightarrow 12$ **do**
  $x \leftarrow$ ECG data of channel ch
  $P \leftarrow \frac{dx}{dt} = 0$ // valleys and peaks in the data
  $Q \leftarrow$ array of size $|P| - 1$
  for $i = 1 \rightarrow |P| - 1$ **do**
    $Q[i] = P[i+1] - P[i]$
  end for
  $M \leftarrow |Q|$
  $I \leftarrow$ Indices of top K largest values in M
  // I is in non-decreasing order
  $Amp\_Map[ch, :] \leftarrow Q[I]$
end for

Algorithm 8 Timing Feature Generation

Input: 1-second 12-Lead ECG Data, f_s, K
Output: Timing Feature Map $Time\_Map$
Initialize $Time\_Map$ as a matrix of size $12 \times 2K$
for $ch = 1 \rightarrow 12$ **do**
  Same procedure as Algorithm 7 until obtaining I
  for $i = 1 \rightarrow K-1$ **do**
    $Time\_Map[ch, 2i-1] = I[i+1] - I[i]$
    $Time\_Map[ch, 2i] = k - I[i]$
    // $I[i] < k \leq I[i+1], k \leftarrow argmin\, P - I[i]$
  end for
  $Time\_Map[ch, 2K-1] = f_s - I[K]$
  $Time\_Map[ch, 2K] = k - I[K]$
  // $I[K] < k \leq f_s, k \leftarrow argmin\, f_s - I[i]$
end for
$Time\_Map \leftarrow Time\_Map / f_s$

Both amplitude and timing generation algorithms take the 1-second 12-Lead ECG and the assumed fiducial point number K as inputs, and output the feature maps of size $12 \times K$ and $12 \times 2K$, respectively. The algorithms compute the features of each channel independently, and then project them onto the output feature maps. For the amplitude map, the salient magnitudes are assessed; for the timing map, the durations between the salient points are taken into account. Under the assumption of existing P, Q, R, S, and T waves, we set $K = 10$ and exhibit an example in Figure 3.6.

Classifier Training

We treat solving the multi-label classification problem as training binary classifiers for each evaluated class. Our heuristics are that each arrhythmia type bears its own unique waveform and is reflected in our generated amplitude or timing maps. Based on the reasoning, we implement the following two experiments to train the binary classifiers for each evaluated class.

1. **Training Models:** Basic DL and ML models are the candidates. Regarding DL strategy, convolutional neural network (CNN) and recurrent neural network (RNN) models are nominated. Referring

to CNN, we borrow the AlexNet architecture with the input size being an image of 12 rows. As for RNN, we employ the long-short term memory units with inputs having a dimension of 12. Concerning ML methods, the models examined include support vector machine, logistic regression, boosting, k-nearest neighbor, decision tree, and random forest.

2. **Training Features:** Three experiments are carried out for feature selection. One includes only the amplitude feature in the model training. Another takes only the timing feature into consideration. To be more specific, we utilize not only the timing map but also the averaged heart rate and heart rate variation in this experiment. The other leverages both amplitude and timing feature maps for training.

To determine the best model for each evaluated class, we run the cross-validation tests on all the designed experiments. We split the data into 80% for training and 20% for testing. In addition, to address the issue of underrepresented classes, or named the imbalanced classes, we randomly pick the samples from the class that have larger sample size to match the size of the smaller group.

Arrhythmia Decision

We proposed a strategy to diagnose the arrhythmias of a patient that is adaptable to the ECG data length. If the given data length is shorter than 20s, then we construct one representative ECG following the procedure in 3.3.2, 3.3.2 and determine the existence of each arrhythmia type by running through the best trained binary classifiers of each class.

For data length exceeding 20s, we randomly select N number of data segments to quantify N representations. Given the original data length L in the unit of seconds, the number N is derived from the

proposed expression:

$$N = \begin{cases} \lceil \frac{L}{10} \rceil & if \quad \frac{L}{10} < 100, \\ 100 & if \quad \frac{L}{10} \geq 100. \end{cases}$$

For N representations, we compute the arrhythmia labels across all evaluated classes, and consider the scores of the classifier as the indicator. For each arrhythmia type, if the maximum score of these N representations is greater than 0.1, then we optimistically assume that the patient has the corresponding arrhythmia type diagnosed.

3.3.3 Experiment Results

We elaborate the outcomes of model training and feature selection experiments in 3.3.3 and display the scores of cross-validation and official tests in 3.3.3.

Training Experiments

From the results of our cross-validation tests, boosting classifiers have the most robust and top-notch performance for all the evaluated classes. The second place goes to the random forest method, whereas deep learning models are inclined to over-fitting.

With respect to the feature selection experiments, we discovered that the timing-deviated arrhythmia types showcase the best performance with solely the timing features. Also, we found that the abnormal waveform-based arrhythmias favor the amplitude feature maps. Combining amplitude and timing feature maps does not significantly improve the performance of the classifiers.

Scores

Table 3.4: Performance of the proposed model.

Dataset	Runtime (hour:minute:second)	Score
CPSC	≈0:20:00	0.455
CPSC_2	≈0:30:00	0.402
Georgia	≈1:00:00	0.456
PTB	≈0:10:00	-2.589
PTB-XL	≈ 1:30:00	0.173
St. Petersburg	≈ 0:30:00	0.340
Official	1:55:00	0.406

We exhibit the cross-validation results of each dataset and the current official score in Table 3.4. Judging from the runtime, we show that our proposed model is competitive (compared to other challengers' models). Assessing the scores, we believe that the proposed model has successfully learned the features since the weighting scores of the cross-validation tests is similar to the current official score.

3.3.4 Conclusions

Our team has delivered an interpretable multi-label arrhythmia classifier. The classifier is built of our devised 12-Lead ECG heartbeat segmentation and feature generation algorithms. We demonstrate that different types of arrhythmias favor the corresponding features, either the amplitude or the timing maps. For future work, we aim at optimizing the arrhythmia prediction and representation learning algorithms.

3.4 Acknowledgments

Chapter 3 contains reprints of P.-Y. Hsu, P.-H. Hsu, H.-L. Liu, C.-T. Lin, H.-T. Chou, Y.-F. Tseng, and T.-H. Lee, "Star-ECG: Visualization of Electrocardiograms for Arrhythmia and Heart Rate Variabil-

ity", *Annual International Conference of the IEEE Engineering in Medicine and Biology Society (EMBC)*, 2021; P.-Y. Hsu, P.-H. Hsu, T.-H. Lee, and H.-L. Liu, "Multi-label Arrhythmia Classification From 12-Lead Electrocardiograms", *IEEE Computing In Cardiology Conference*, 2020; and P.-Y. Hsu and C.-K. Cheng, "Arrhythmia classification using deep learning and machine learning with features extracted from waveform-based signal processing", *Annual International Conference of the IEEE Engineering in Medicine and Biology Society (EMBC)*, 2020.

I would like to thank my coauthors Chung-Kuan Cheng, Hung-Tao Chou, Po-Han Hsu, Tsung-Han Lee, Chi-Te Lin, Hsin-Li Liu, and Yu-Fang Tseng for their insightful suggestions and clarifications on our published works.

Chapter 4

Computational Methodologies for ECG and SCG Biometric Identification

This chapter presents three cardiac signal-based biometric identification systems. First, we demonstrate a competitive ECG identification system, which was built on the ECG data of 47 arrhythmia patients from the MIT-BIH database. Next, we showcase a promising SCG authentication system, which was tested on the SCG data of 20 subjects from the PhysioBank open dataset. Last, we demonstrate a motion artifact resilient SCG authentication system, which was constructed by using our own dataset of 20 healthy young individuals.

4.1 Challenge in Biometric Identification for ECG

In modern society, biometric systems have been widely applied to human identification to achieve high level security. A standard biometric system is illustrated in Figure 4.1. Typical biometric systems process the data, extract their features, and evaluate the matching score between the query and the database

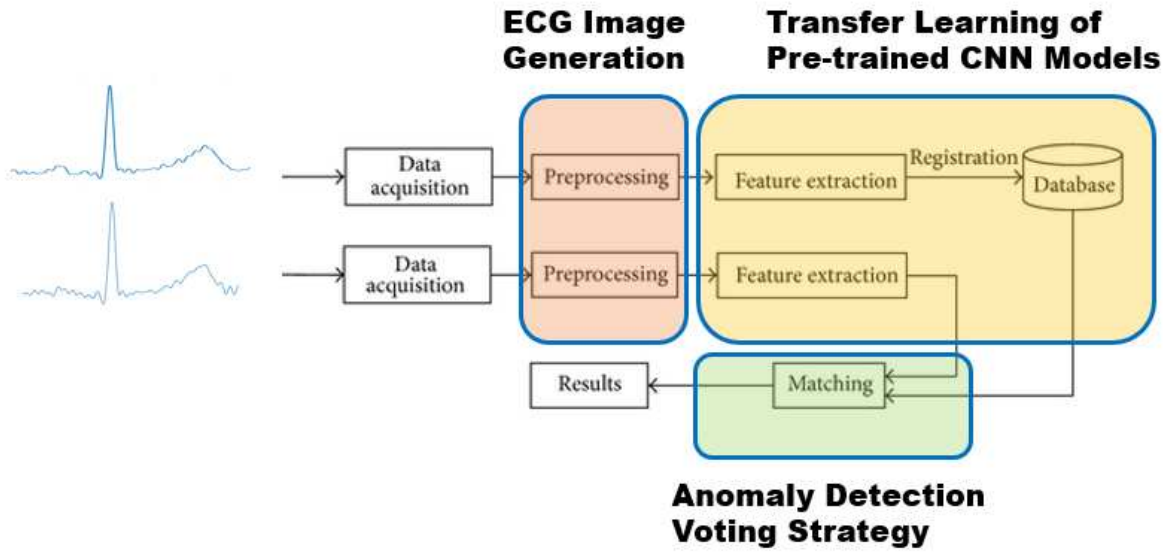

Figure 4.1: Schematics of a standard biometric system and our contributions.

to determine the subject's identity. Nowadays, fingerprint, face, and iris are commonly used biometrics [63]. However, all the aforementioned biometrics are vulnerable to spoofing attacks [119]. For example, fingerprints left on an object can be recreated with latex; iris images can be fooled with contact lenses; facial recognition can be cracked by high-resolution stolen photos.

To circumvent the intrinsic issues in external biometrics, electrocardiogram (ECG) has gained its popularity as a biometric in recent years. ECG is a continuous measure of electrical depolarization and repolarization throughout cardiac activities; moreover, quasi-periodicity is observable in ECG. An individual's ECG is influenced by that individual's cardiovascular system, and the uniqueness of ECG has been reported in several studies [18] [78]. ECG shows several advantages as a biometric: (1) difficult to be stolen; (2) able to indicate liveness; (3) easy to acquire.

Numerous feature extraction and pattern recognition techniques have been proposed for ECG,

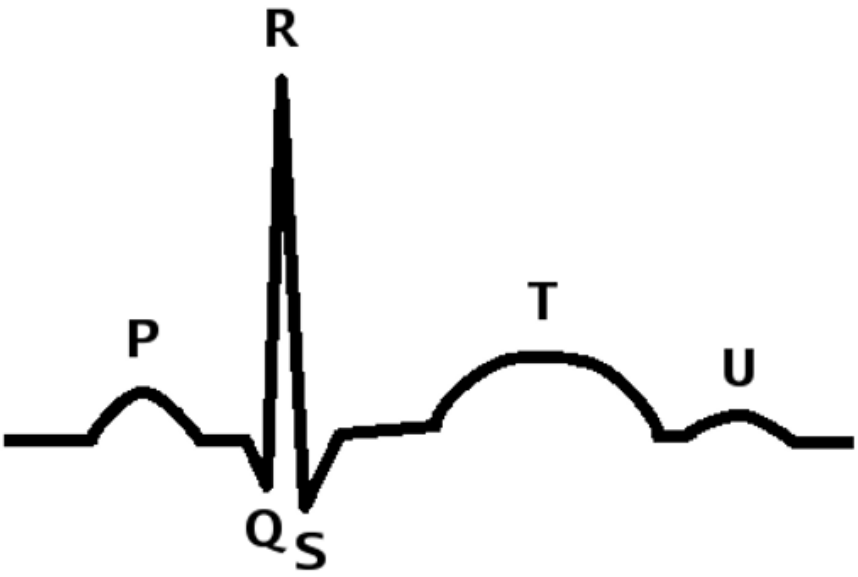

Figure 4.2: Illustration of a typical ECG waveform. P, Q, R, S, T, and U waves are fiducial points that are commonly observed in healthy subjects.

and they can be classified into two categories: fiducial and non-fiducial strategies.

1. **Fiducial Strategies:** Figure 4.2 shows that a typical ECG waveform contains fiducial points, namely, P, Q, R, S, T, and U waves. Based on the prior knowledge, researchers extract features such as the amplitude and the slope composed of these fiducial points [65] [94] [104]. The features selected from the QRS complex have been the most popular in the proposed ECG biometric systems because the QRS complex tends to be stable against physical and emotional variations [108]. The performance of fiducial methods depends on not only the existence but also the accurate acquisition of the fiducial points.

2. **Non-Fiducial Strategies:** To generalize the ECG identification models, researchers have suggested non-fiducial methods. Such techniques do not rely on the hand-crafted feature sets. Commonly used

approaches are automatic segmentation of ECG waveforms followed by a machine-learning (ML) or deep-learning (DL) model [98] [105].

Non-fiducial strategies have attracted attention recently since ML and DL have shown promising results in accomplishing identity and image recognition tasks [37] [42] [66].

Several non-fiducial methods have been proposed in literature. For example, one-dimensional convolution neural network (1D-CNN) models have been proposed by Chen and Chen [21], Wu *et al.* [111], and Zhang *et al.* [118]. Besides CNN, one-dimensional recurrent neural network (1D-RNN) models have also been proposed by a number of researchers, including Lynn *et al.* [72], and Salloum and Tsai [95]. Other ECG identification approaches include sparse representation method proposed by Li *et al.* [67] and 2D-CNN methods proposed by Ranjan [91] and Byeon *et al.* [16].

While the aforementioned methods present promising ECG identification systems, we discover two issues that could possibly lie in the proposed methods. First, the segmentation of ECG requires to be an empirically fixed number. For example, in Salloum and Tsai's work [95], the length of the ECG waveform is forced to be 251 samples for the MITDB dataset and 301 for the ECG-ID dataset; both require the R-peaks positioning at the center. Similar ECG segmentation procedure has been adopted by Lynn *et al.* [72], but they stack and concatenate ECG heartbeats. In Chens' work [21], 251 samples have to be acquired from one ECG beat with the R-peak standing at the 71^{th} position. Generally speaking, some one-dimensional neural network models can only handle data of fixed length and position, which might not be generalizable for extreme ECG data.

Another issue is pointed out by a comparative analysis of ECG biometric systems conducted by Odinaka *et al.* [81]. In their paper, the authors indicate that a reliable ECG identification model should be trained on past ECG data and perform identity testing on future ECG data, instead of training and testing the ECG data within the same period. To be more specific, one should build an ECG identification model

and conduct across-session tests instead of within-session tests. Some of the aforementioned works have reported within-session results [72] [95] [118], which could possibly bias the evaluation.

In this work, we address the two issues through a combination of approaches as shown in Figure 4.1. First, we propose an ECG image generation algorithm that is able to handle any specified number of ECG heartbeats. Such an algorithm uses detected R-peaks as folding points and projects ECG data onto a two-dimensional image, which overcomes the challenge of hardly-required fixed length and truncated ECG. Second, we perform across-session testing. We construct the ECG identification models by using the past ECG data and evaluate their performance on future ECG data. We leverage transfer learning of pre-trained CNN models to efficiently build the ECG biometric system. Furthermore, we develop a voting strategy that is able to detect anomaly ECG heartbeats.

The rest of the section is organized as follows. We first review the relevant literature in Section 4.1.1 and then present our ECG image identification models in Section 4.1.2. Subsequently, we describe the two public ECG datasets, MITDB and ECG-ID, which are used to evaluate the performance of the proposed identification models. Next, we present and discuss our experiments and results in Section 4.1.3. Finally, we conclude our work in Section 4.1.4.

4.1.1 Related Works

Numerous works have been proposed to recognize the patterns of ECG waveforms, and on a large scale, they can be classified by the approaches being either fiducial or non-fiducial.

For fiducial approaches, researchers first extract the features from ECG waveforms and then apply machine learning classifiers to accomplish ECG biometric tasks. The features are often extracted first by labeling the characteristic points (P, Q, R, S, T, and U waves depicted in Figure 4.2) and then computed based on the algorithms devised by the researchers. For instance, Biel *et al.* combine 10

fiducials together with PCA and use generative model classifier to perform ECG biometric tasks [13]. Biel *et al.*'s model demonstrates an identification rate of 100% on 20 subjects with ECG collected through multiple days. Shen extract 17 fiducials from ECG waveforms and apply k-nearest neighbor (kNN) classifier to do identity matching [99]. Shen reports an identification rate of 95.3% on 168 subjects with ECG data collected on a single day.

For non-fiducial methods, we can split the techniques into ML and DL. For ML tactics, researchers extract non-fiducial features first and then perform identity matching with ML algorithms. For DL strategies, researchers combine the feature extraction and matching score computation together in a neural network model; or, they may leverage DL model as a feature extractor and perform classification task with other ML/DL classifiers.

For ML example, Ye *et al.* extract non-fiducial features with independent component analysis and discrete wavelet transform and utilize support vector machine of radial basis kernel to classify the subjects [114]. An identification rate of $> 80\%$ has been reported by Ye *et al.* on 65 subjects with ECG data measured on the same day. Ghofrani and Bostani choose autocorrelation and period transform as their weapon to extract non-fiducial features [35]. Then, they complete ECG biometric tasks with kNN and achieve an identification rate of 100% on 12 subjects.

For DL example, Salloum and Tsai build one hidden layer 1D-RNN with different functional units and evaluate the performance of the models on the ECG-ID and MITDB datasets. Their best identification rate is 100% for both datasets with long short-term memory (LSTM) chosen, which outperforms gated recurrent units. Moreover, the sequence length is required to be nine consecutive heartbeats [95]. Wu *et al.* combine 1D-CNN and RNN together and demonstrate identification rates of 99.70% and 97.54% on the MITDB and ECG-ID datasets, respectively. Zhang *et al.* develop a multi-resolution 1D-CNN which has archietecture similar to AlexNet and achieve an identification rate of 91.1% on the MITDB dataset.

For fiducial methods, the identification rate is influenced by the accuracy of extracted fiducial features, and for non-fiducial methods, depends on the structure of learning models and ECG data representation. We aim at developing a non-fiducial ECG identification technique that can address the data segmentation issue.

4.1.2 Methodology

Using ECG image to identify humans

In this section, we present our ECG image identification system. There are four steps in building the whole system. First, we detect the R-peaks of ECG signals. Second, we generate a two-dimensional image for each segment of ECG signals. Third, we perform transfer learning to fine-tune the identification model parameters. Last, we use voting strategy to identify the subjects.

Detecting ECG R-peaks

Our first step is to detect each ECG beat from the raw signals. To complete this task, we use the Pan-Tompkins algorithm to detect the R-peaks of the raw signals [83]. Pan-Tompkins algorithm is a real-time and state of the art R-peaks detection method. It detects R-peaks by processing the raw signal through filtering and automatic thresholding. According to Pan and Tompkins's paper [83], the Pan-Tompkins algorithm can correctly detect 99.3% R-peaks in MITDB.

Generating 2D ECG Image

Figure 4.3 showcases the raw ECG signal and its generated ECG image. We develop an ECG image generation algorithm that can handle varying numbers of ECG beats. To explain the image generation procedure, we denote the detected R-peaks as R_i, where symbol i stands for the position of the R-peaks.

Given a sequence of N R-peaks $\{R_{i_1}, R_{i_2}, R_{i_3}, ..., R_{i_N}\}$ in ascending order, we compute the midpoints between each two consecutive R-peaks and create a new sequence $\{R_{j_1}, R_{j_2}, R_{j_3}, ..., R_{j_{N-1}}\}$, in which j_k is the midpoints of the k^{th} and $k+1^{th}$ R-peaks.

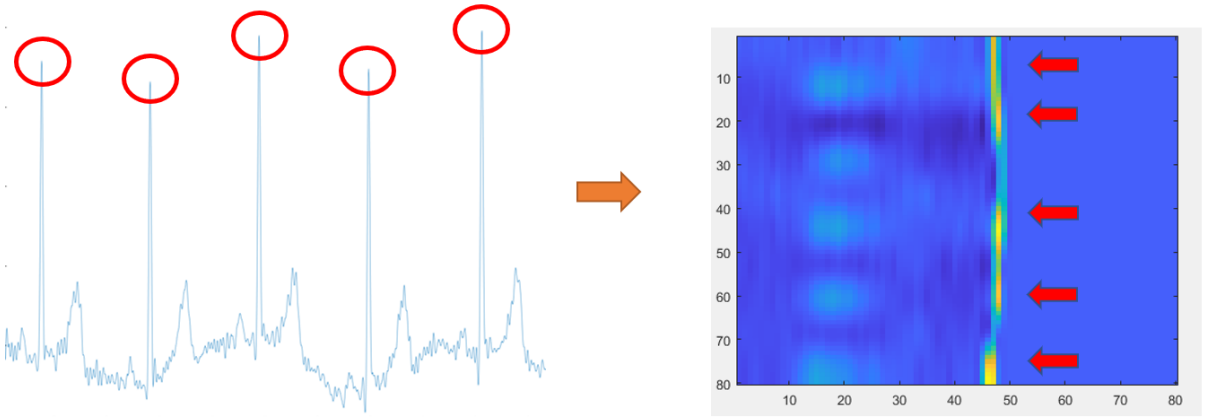

Figure 4.3: Demonstration of folding a raw signal into a two-dimensional ECG image. On the left, we present a raw ECG sample with five heartbeats; on the right, we draw the image of the ECG sample, which is generated by our folding approach. The five R-peaks are denoted in red circles and arrows on the left and right plots.

Once we have the R-peak and midpoint sequences, we generate the image in the following procedure:

$$X[k,:] = \begin{cases} D[R_{j_{\lceil k/2 \rceil}} : 1 : R_{i_{\lceil k/2 \rceil + 1}}], & \text{if } k\%2 = 1 \\ D[R_{j_{\lceil k/2 \rceil + 1}} : -1 : R_{i_{\lceil k/2 \rceil + 1}}], & \text{otherwise} \end{cases} \tag{4.1}$$

where $X[k,:]$ represents the k^{th} row of the generated image X, and D is the ECG data. For the odd number of row, we project the ECG data from the midpoint to the R-peak onto the row in sequential order; as for the even number of row, we project the ECG data from the R-peak to the next midpoint in reverse order. Here, we directly treat each pixel as one time-point, and the pixel's value represents the corresponding

ECG voltage. Since the period of heartbeats ranges from $0.5-2$ Hz, we guarantee the image size is bounded by $2(N-1)\times 2f_s$, where f_s is the data sampling rate and N being the number of the ECG beats.

Building ECG Identification Models

Unlike conventional biometric identification system, we combine feature extraction and matching distance evaluation together by using the pre-trained deep learning models. In this research, we select ResNet18 [38] and AlexNet [64] as our pre-trained networks to conduct transfer learning since they are known for the abilities to extract informative features from images. For each network, we change the input size to $M\times M\times 1$ and output size to C in which $M\times M$ is the size of the ECG image and C is the number of subjects to identify.

Table 4.1.2 displays all the models built in the current research. For each ECG sample, we are free to select the heartbeat number and generate the ECG image by using the approach introduced in 4.1.2. Therefore, for each given length (defined by heartbeat counts) of data sample, we trained an identification model. For example, X-HB model means an identification model for input images of X consecutive heartbeats. In this study, we built the models for sequence length varying from one to five for each dataset.

Voting for Identification

We adopt anomaly detection and majority vote in final identification decision. Suppose we trained 1-HB, 2-HB, and 3-HB models, for each testing heartbeat, we would have three identification results computed by each model, respectively. Then, we claim the testing heartbeat to be anomaly if any two results differ from each other. In other words, a heartbeat is valid only if it shows identical identity across all the identification models. For each recording, we first sift the valid heartbeats and then use majority

Table 4.1: Models Tested in this work.

Model	CNNs	Dataset	# ECG Beat
a	AlexNet	ECG-ID	1
b	AlexNet	ECG-ID	2
c	AlexNet	ECG-ID	3
d	AlexNet	ECG-ID	4
e	AlexNet	ECG-ID	5
f	AlexNet	MIT-DB	1
g	AlexNet	MIT-DB	2
h	AlexNet	MIT-DB	3
i	AlexNet	MIT-DB	4
j	AlexNet	MIT-DB	5
k	ResNet18	ECG-ID	1
l	ResNet18	ECG-ID	2
m	ResNet18	ECG-ID	3
n	ResNet18	ECG-ID	4
o	ResNet18	ECG-ID	5
p	ResNet18	MIT-DB	1
q	ResNet18	MIT-DB	2
r	ResNet18	MIT-DB	3
s	ResNet18	MIT-DB	4
t	ResNet18	MIT-DB	5

vote to determine the identity of the subject. The identification rate is calculated by the number of correct prediction made divided by total prediction number.

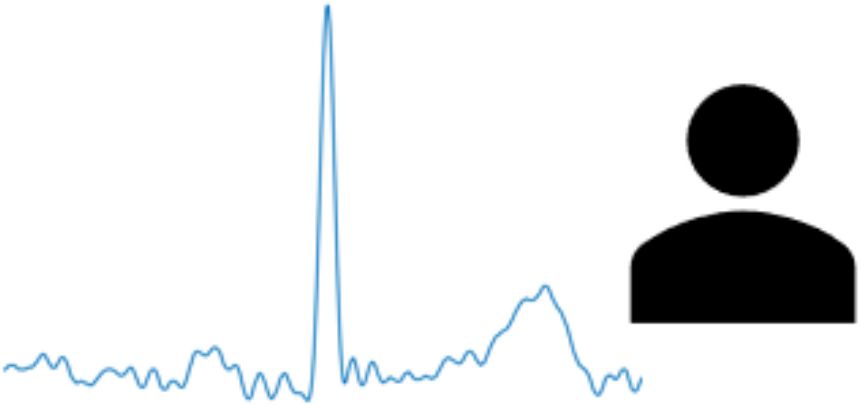

Model	Model Output	Result
1 Beat	Subject 1	Subject 1
2 Beats	Subject 1	Subject 1
3 Beats	Subject 2	Anomaly

Figure 4.4: Demonstration of the subject identification result of one ECG beat.

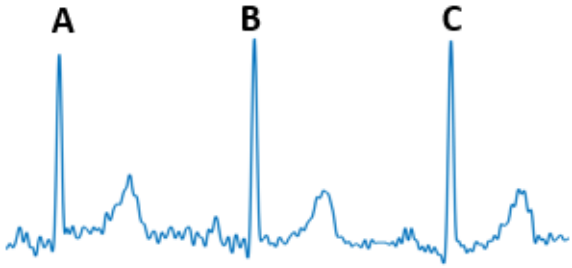

Model	Result of A	Result of B	Result of C	Voting
1 Beat	Subject 1	Subject 1	Subject 2	Subject 1
2 Beats	Subject 1	Subject 1	Anomaly	Subject 1
3 Beats	Anomaly	Subject 1	Anomaly	Subject 1

Figure 4.5: Demonstration of the subject identification result of three ECG beats using our voting strategy.

We provide an example to elucidate the introduced identity matching strategy in Figures 4.4 and 4.5. To simplify the explanation, we consider the case of ECG beats with models trained on sequence length varying from one to three. In Figure 4.4, we display the outputs and identity matching results of three models from the same ECG beat. If we identify the subject based on a single ECG beat, we only need to take the output of 1-HB model into account; if we identify the subject using two consecutive ECG beats, then we take outputs from 1-HB and 2-HB models into consideration. In Figure 4.4, both 1-HB and 2-HB generate the same identity output; therefore, the subject identity is matchable. Finally, if we recognize the subject with three consecutive ECG beats, then we take all three outputs into consideration. Since the output of the 3-HB model deviates from 1-HB and 2-HB models, we mark the ECG heartbeat as anomaly.

Following the anomaly detection of single ECG beat, we perform majority voting to finalize the

identity matching of the subject. In Figure 4.5, we consider a sequence of three ECG beats. For 1-HB model, we conduct majority vote without ambiguity. Considering the results of two consecutive ECG beats, we observe one anomaly and two identical matchings; as a result, we match the subject to subject 1. Finally, for three consecutive ECG beats, we arrive at two anomalies and one successful subject match. We still match the subject to subject 1 since we do not take anomalies into account when voting.

Datasets

We ran our identification models on two publicly available datasets that are often used for ECG biometric system evaluation: MITDB [79] and ECG-ID [71]. Both datasets are downloadable from PhysioNet database [36].

The MITDB dataset contains 48 two-channel 30-minute recordings of ECG measured from 47 subjects (25 male and 22 female) diagnosed of arrhythmia. Only one subject has two recordings. Every recording is sampled at a frequency of 360 Hz with 11-bit resolution over a 10 mV range.

The ECG-ID dataset contains 310 one-channel recordings of ECG obtained from 90 subjects (44 male and 46 female). Each subject has various number of recordings, which ranges from one to twenty. Some subjects have recordings collected on the same day, while the others have recordings measured over 6 months. All the recordings have length of 20 seconds sampled at 500 Hz with 12-bit resolution over 10 mV range. The ECG-ID is mentioned as a challenging dataset by several previous works [67] [91] [111].

4.1.3 Experimental Setup and Results

Experimental Setup and Implementation

We aim at using the past ECG to verify the identity of future ECG; as a result, we choose to follow the experiment settings in [111] for the MITDB dataset and [85] for the ECG-ID dataset. For the

MITDB dataset, we use the first 70% of heartbeats as training and the rest as testing for all 47 subjects. Concerning the ECG-ID dataset, we select the same 12 subjects (id: 3, 10, 24, 25, 30, 32, 34, 36, 52, 53, 59, 72) who have recordings collected on multiple days as Patro and Kumar did [85]. We train our identification models on the first two recordings and test them on the following three recordings.

We conduct all the experiments with MATLAB R2019B. For image generation, we set the image size as $2(N-1) \times f_s$ and resize the image to 80×80 to train the models. For training process, we use adam optimizer [61] with learning rate 0.0001. Based on the size of the two datasets, we set the mini-batch size to 20 for the ECG-ID dataset and 100 for the MIT-DB dataset. We found that 20 epochs were enough for the models to converge, so we set 20 as the number of the epoch for our experiments.

Identification of ECG Image

Table 4.2: Performance of the models in this work.

Model	Identification Rate
a	88.89%
a+b	83.33%
a+b+c	83.33%
a+b+c+d	91.7%
a+b+c+d+e	91.7%
f	100%
f+g	100%
f+g+h	100%
f+g+h+i	100%
f+g+h+i+j	100%
k	91.7%
k+l	88.9%
k+l+m	88.9%
k+l+m+n	91.7%
k+l+m+n+o	94.4%
p	100%
p+q	100%
p+q+r	100%
p+q+r+s	100%
p+q+r+s+t	100%

We show the performance of each model in Table 4.1.3, in which the plus sign stands for adopting the voting strategy introduced in 4.1.2. Considering the MITDB dataset, our model performs very well with an identification rate of 100% in all number of ECG. We think there are two reasons that can explain such good results. First, we have sufficiently large data sample during the training process for the MIT-DB dataset. Second, although we used the past ECG to predict the future, the recording is still

the same one for each individual. As for the ECG-ID dataset, interesting results have shown. Single beat and five consecutive beats produce the best results in both AlexNet and ResNet18 transfer learning models. In addition, ResNet18 trained with five consecutive beats achieves the best performance with an identification rate of **94.4%**. This indicates that two and three consecutive beats are prone to identity matching errors than single beat does. Such a phenomenon might be induced by short-term bad ECG data acquisition. Nevertheless, keep adding beat numbers on top of three consecutive beats pulls back to good results.

Comparison to the state of the art

Table 4.3: Comparison to the state of the art.

Model on MIT-DB	Identification Rate
1D-CNN + LSTM [111]	99.70%
Ours [AlexNet and ResNet18]	**100%**
Model on ECG-ID	**Identification Rate**
Fiducial [85]	88.9%
PCANet + SVM [107]	**94.4%**
Ours [ResNet18-5 beats]	**94.4%**

We compare the performance of our model to the state of the art in Table 4.1.3. Our model shows its competency in both datasets. In MIT-DB dataset, most published results demonstrate outstanding identification results. As to the ECG-ID results, it appears that non-fiducial methods such as ours and Wang *et al.* [107] are likely to explore the features for better identity matching. The reasons could be due to the short and varying states of the ECG data in the ECG-ID dataset. We investigate into the mis-classified subject and discover that both our model and Wang *et al.*'s falsify two recordings of subject 72 as subject 59. Given the fact that two models arrive at the same mis-classification, it seems reasonable to

conclude that the two recordings of subject 72 are susceptible to be categorized as subject 59.

Qualitative Results of ECG Image

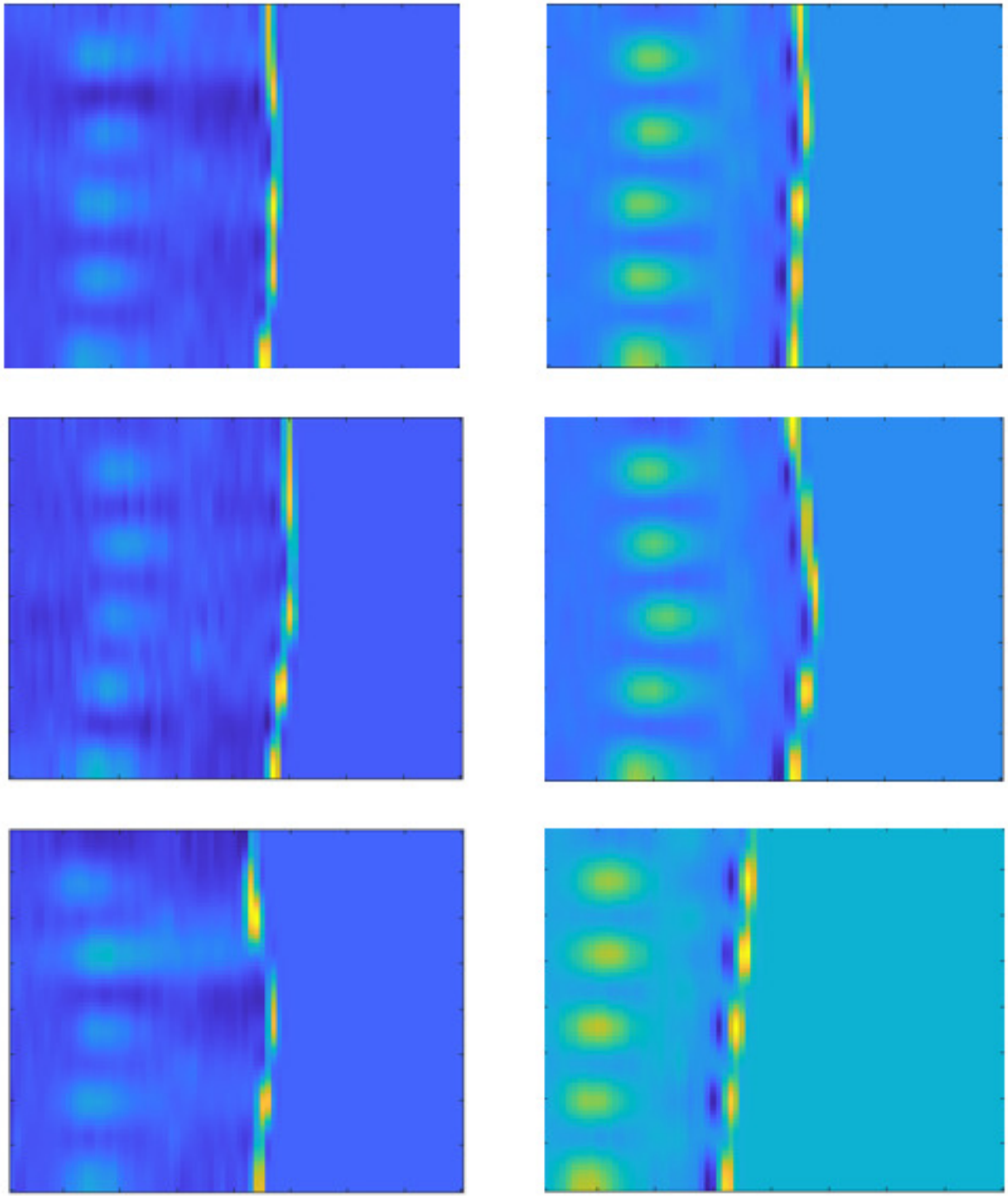

Figure 4.6: Demonstration of ECG image generated from two subjects in the ECG-ID dataset. Three figures on the left plot ECG image of subject 3, while three figures on the right plot ECG image of subject 72.

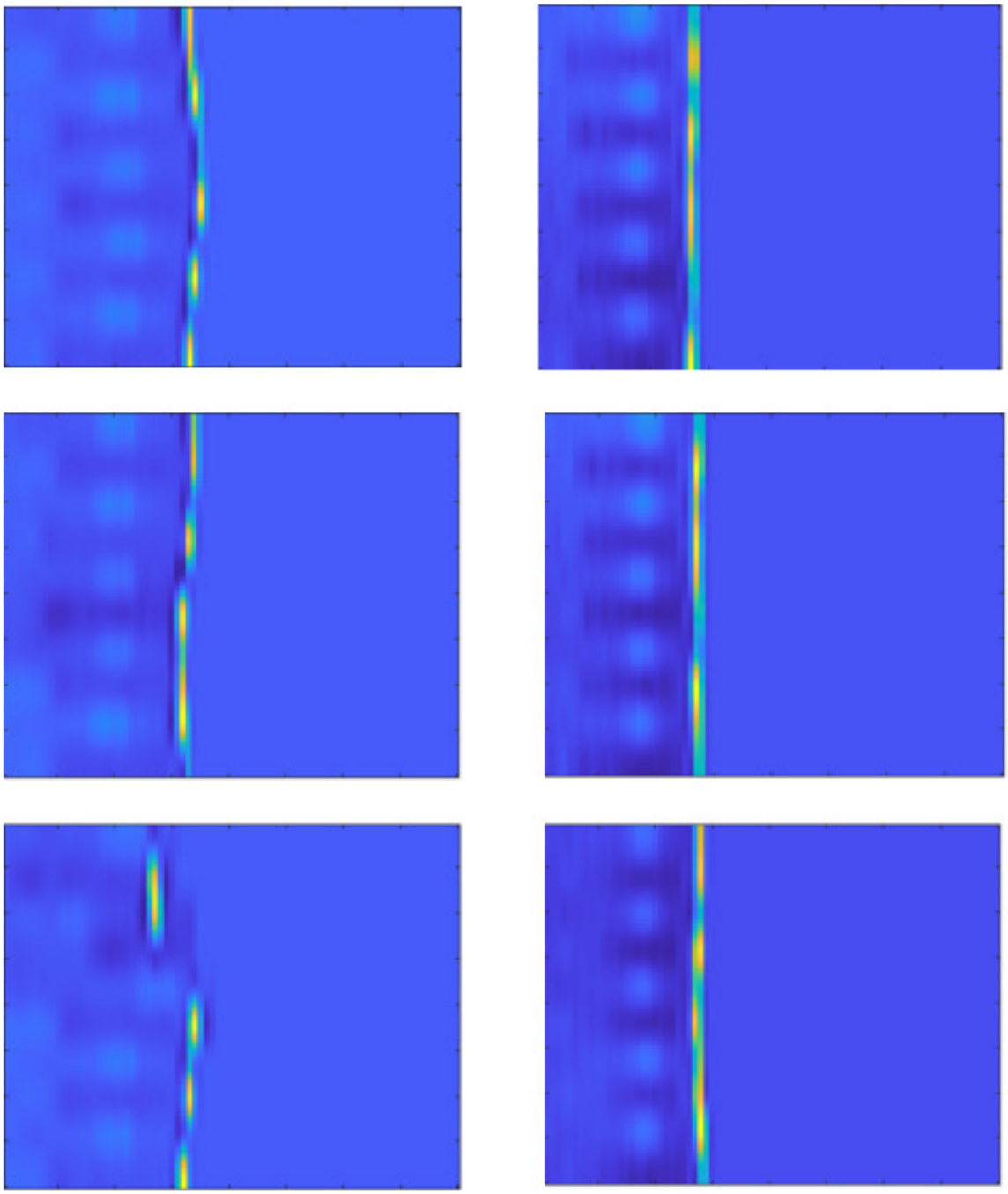

Figure 4.7: Demonstration of ECG image generated from two subjects in the MIT-DB dataset. Three figures on the left plot ECG image of subject 100, while three figures on the right plot ECG image of subject 234.

Figures 4.6 and 4.7 demonstrate the ECG images generated from two different subjects within the ECG-ID dataset and the MIT-DB dataset, respectively. We observe not only the perceptual difference between each two subjects but also the visual similarity between different recordings of the same subject. Focusing on the ECG-ID dataset, we are able to tell that subject 72 has either larger P wave or T wave compared to subject 3, whereas subject 3 has a sharper R-peak. In addition, the testing data of subject 2 differs from its training data more than subject 3 does. Shifting the attention to the MIT-DB dataset, we observe the differences of heart rate between subject 100 and subject 234. Subject 234 has a higher heart rate compared to subject 100 because it displays shorter folding segment. Furthermore, arrhythmic heart beats are clearly shown in the testing data of subject 100, in which the folding ECG segments have observable different lengths. In summary, the qualitative results showcase that ECG could be a promising biometric.

4.1.4 Conclusions

We contribute a novel ECG image generation approach that is able to generate competitive ECG biometric models by leveraging transfer learning method. Such approach has been evaluated on MIT-DB and ECG-ID datasets. We observe satisfiable results of the proposed models in both datasets: 100% on the MIT-DB and 94.4% on ECG-ID. In addition, qualitative results demonstrate the uniqueness of ECG in each subject. More importantly, our method also generate satisfying results by using a single ECG beat to conduct identity matching task.

4.2 Challenge in Biometric Identification for SCG

In recent years, biometric systems have been largely applied to human identity verification to perform high level security. An example of a standard biometric system is illustrated in Figure 4.8. Commonly used biometric systems consist of three functional blocks: 1) data processing, 2) features extraction, and 3) matching evaluation. The matching score will then be utilized to identify the subject. In modern society, iris, face, and fingerprint are commonly used biometrics [63]. However, every aforementioned biometric is susceptible to spoofing attacks [119]. For instance, fingerprints can be left on an object and recreated with latex; iris images can be cheated with colored contact lenses; facial recognition can be hacked by high-resolution substitutable photos.

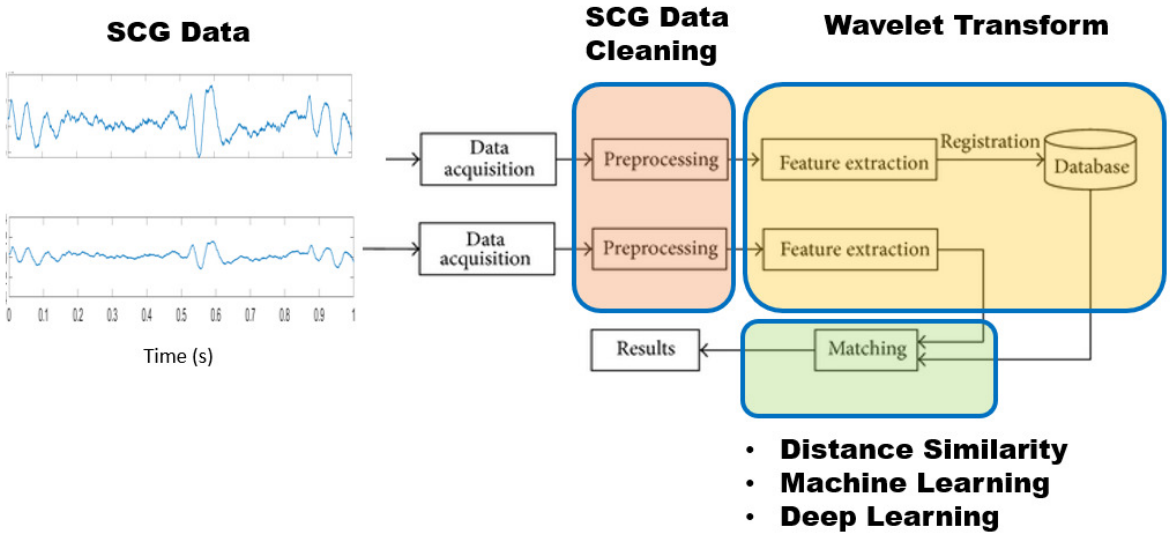

Figure 4.8: Schematics of the standard biometric system in conjunction with our contributions. Classic biometric systems process the data, extract the features, and compute the matching score between the query and the database to determine the subject's identity.

To circumvent the intrinsic issues in external biometrics, physiological signals such as electrocardiograms (ECG) and seismocardiograms (SCG) have attracted attention as a biometric in recent years. Both ECG and SCG are continuous measures and show quasi-periodicity in themselves. ECG measures electrical depolarization and repolarization throughout cardiac activities; SCG captures the chest's surface motion caused by the contraction of the heart [54]. An individual's cardiac signal reflects that individual's cardiovascular system, and physiological signals show several advantages as a biometric: (1) difficult to be stolen; (2) able to indicate liveness; (3) easy to acquire.

ECG biometric has been reported in several studies [18] [47] [78] [111], yet to the best of our knowledge, the uniqueness of SCG [15] has only been reported in one study conducted by Bui *et al.* [15]. In Bui *et al.*'s work, a 98.89% recognition rate has been reported by manipulating SCG data.

In this section, we propose different SCG biometric models, and we make contributions as follows:

- extracting SCG biometric features with continuous wavelet transform
- presenting state-of-the-art performance SCG biometric models
- demonstrating the efficacy of SCG biometric in both one-dimensional SCG data and time-frequency SCG patterns

The rest of the paper is organized as follows. We first review the relevant work in subsection 4.2.1 and then present our SCG models in subsection 4.2.2. Subsequently, in subsection 4.2.3, we describe the experimental design and discuss our experimental results. Finally, we make conclusions of this work in Section 4.2.4.

4.2.1 Related Work

In this subsection, SCG and related physiological biometric, ECG, are introduced. SCG is a measure of heart-induced motion, and it has been studied since the 1940s. During the 20^{th} century, measuring good quality SCG was difficult, let alone using SCG as a biometric. In the past decade, the study of SCG increases owing to the advance of sensor technology [54] [103].

The majority of researchers exploit SCG for heart rate computation, vital signs estimation, or motion activity detection [20] [34]. Regarding SCG analysis, multiresolution wavelet analysis is widely adopted, which is accomplished by passing SCG into a series of wavelet transforms [96]. Once wavelet transform is completed, researchers then analyze the relation between the transformed SCG and the target.

Viewing SCG as a biometric, Bui *et al.* performed principal component analysis to extract features from SCG and devised a probabilistic Euclidean distance metric to determine the SCG's identity [15]. Bui *et al.* show that such method achieves a 98.89% recognition rate, and they indicate that SCG could be a promising biometric.

Similar to SCG, ECG is also a signal generated by the heart. ECG records the electrical signal produced by the heart. Compared to SCG, which is sensitive to human's motion, ECG experiences less artifacts and technical difficulties to acquire [26]. Moreover, ECG has been known to differ from one individual to another based on the uniqueness of an individual's cardiovascular system [18].

ECG identification strategies are classified into two categories: fiducial and non-fiducial approaches. For fiducial approach, researchers first identify the fiducial points in ECG waveforms, and then extract the features from the selected fiducial points to perform ECG identification [94]. On the other hand, non-fiducial method does not require hand-crafted features extracted from the ECG waveforms. To generalize ECG identification, researchers have suggested adopting non-fiducial strategies such as machine learning or deep learning methods [37].

In recent ECG biometric research, state-of-the-art performance has been achieved using transformed two-dimensional ECG image along with deep neural networks [17] [47]. Byeon *et al.* perform continuous wavelet transform on ECG and train deep convolutional neural networks (CNN) on the scalograms of ECG signals for biometrics [17]. They showcase the efficacy of such method achieving 0% equal error rate (EER) on PTB-ECG database. Hsu *et al.* have proposed a 2D ECG image generation technique and also trained the deep CNN on the ECG image for biometrics [47]. They present the model achieving 0% EER on MIT Arrhythmia database.

In light of one-dimensional SCG being a potential biometric [15], we aim at developing a two-dimensional SCG biometric model. Based on the promising results shown in transformed 2D ECG biometric model [17] [47], we hypothesized that the proposed 2D SCG biometric model would outperform 1D SCG biometric model. In this study, we perform continuous wavelet transforms to generate 2D SCG data, which is similar to Bui *et al.*'s study. Furthermore, we experiment with different mother wavelets, signal processing, and biometric matching methods other than deep CNN models, which to the best of our knowledge, has never been performed on SCG biometrics.

4.2.2 Methodology

Proposed Methods

In this section, we present our SCG biometric system as illustrated in Fig. 4.8. There are three steps in building the whole system: signal processing, wavelet transform, and model training.

Signal Processing

We clean the raw SCG signals and segment each SCG into 1 second long data in signal processing procedure. Fig. 4.9 displays raw electrocardiogram (ECG), raw SCG, and the processed SCG.

The raw SCG signals contain noise; therefore, we process the raw SCG signals first to acquire clean SCG waveforms. To complete this task, we perform filtering and detrending. First, we filter the raw signal with a third order Savitzky-Golay filter with 0.01s time span. Next, we remove baseline wandering through detrending (the default *detrend* command in MATLAB).

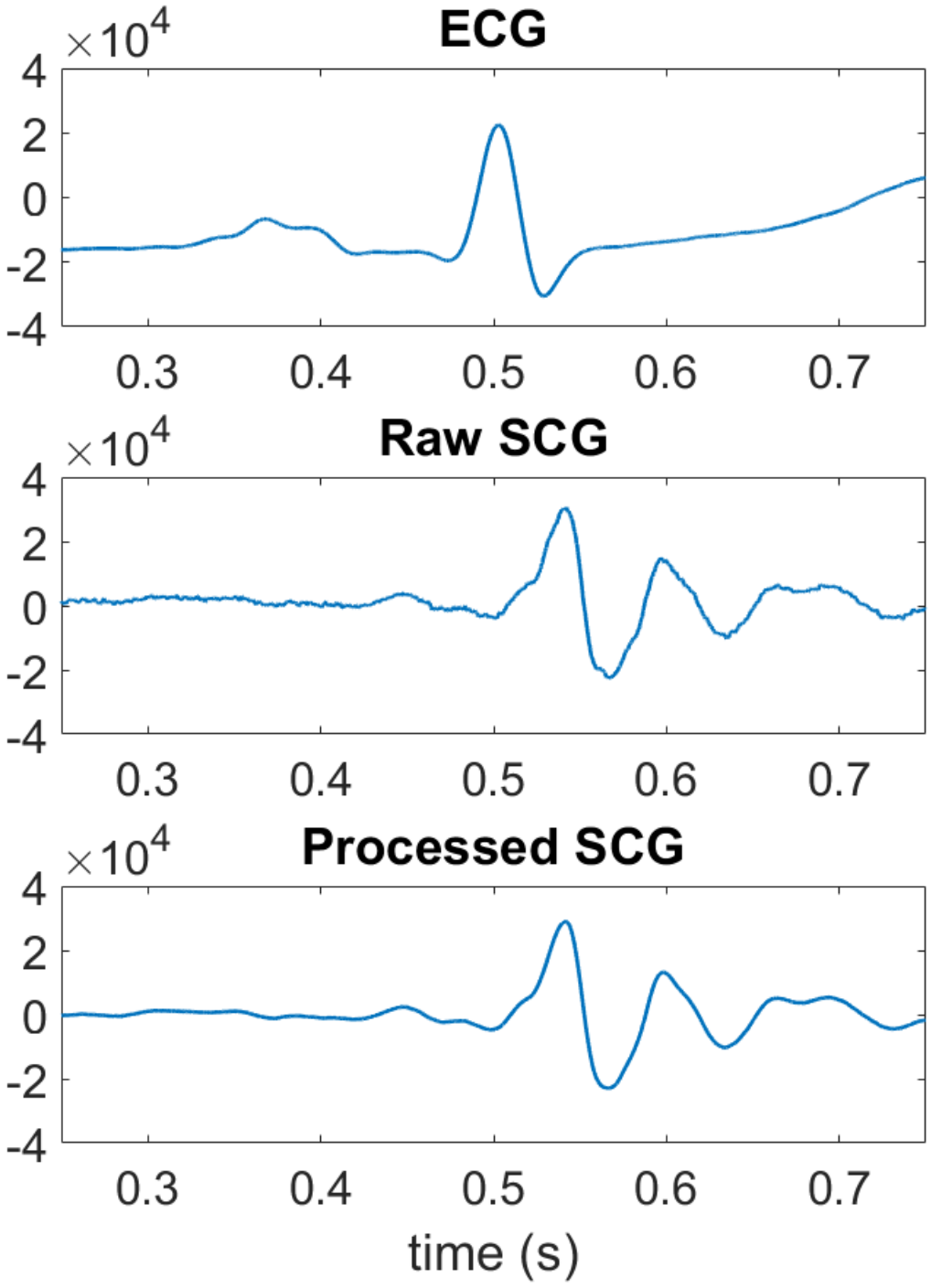

Figure 4.9: Demonstration of 0.5 second raw electrocardiogram, raw seismocardiogram, and processed seismocardiogram. In processed SCG, high frequency noise is smoothed out by the Savitzky-Golay filter.

To segment SCG signals, we utilize both ECG and SCG signals in our implementation. First, we run the Pan-Tompkins algorithm to identify ECG R-peaks [83], which is a widely adopted approach to search for the ECG R-peaks. Second, we locate the aortic valve opening (AO) peak in each SCG by finding the maximum peak that is nearest to the corresponding ECG R-peak. Last, we extract the 1 second SCG data by taking the signal from 0.5 second prior to the SCG AO peak to 0.5 second posterior to it.

Wavelet Transform

We perform continuous wavelet transform on each 1 second SCG data to acquire time-frequency pattern for the biometric matching. The continuous wavelet transform is defined as

$$X_{\omega}(a,b) = \frac{1}{|a|^{1/2}} \int_{-\infty}^{\infty} x(t)\overline{\psi}(\frac{t-b}{a}), \tag{4.2}$$

in which $x(t)$ is our 1 second SCG data, function ψ is the mother wavelet, and parameters a, b are the scaling factor and the translation value, respectively. The mother wavelets experimented in this study are Morse, Gabor, and Bump. The three wavelet functions embed different temporal structures, and Fig. 4.10 displays the waveforms of Morse, Gabor, and Bump wavelets. Morse wavelets are defined in Lilly *et al.*'s work [69] as

$$\psi_{\beta,\gamma}(\omega) = U(\omega)\alpha_{\beta,\gamma}\omega^{\beta}e^{-\omega^{\gamma}}. \tag{4.3}$$

Function $U(\omega)$ is the heaviside function. Parameters β and γ determine the shape of the wavelet functions, and α is a normalizing constant. Gabor wavelet is expressed as

$$\psi(s\omega) = U(s\omega)\pi^{-1/4}e^{-(s\omega-6)^2/2}, \tag{4.4}$$

and the expression of Bump wavelet is

$$\psi(s\omega) = e^{1-\frac{1}{1-(s\omega-5)^2/0.36}} \mathbf{1}_{[4.4/s,5.6/s]}. \tag{4.5}$$

The s parameter represents the scaling factor in both equations (4.4) and (4.5). Symbol $\mathbf{1}_{[4.4/s,5.6/s]}$ stands for the indicator function in the interval of [4.4/s , 5.6/s].

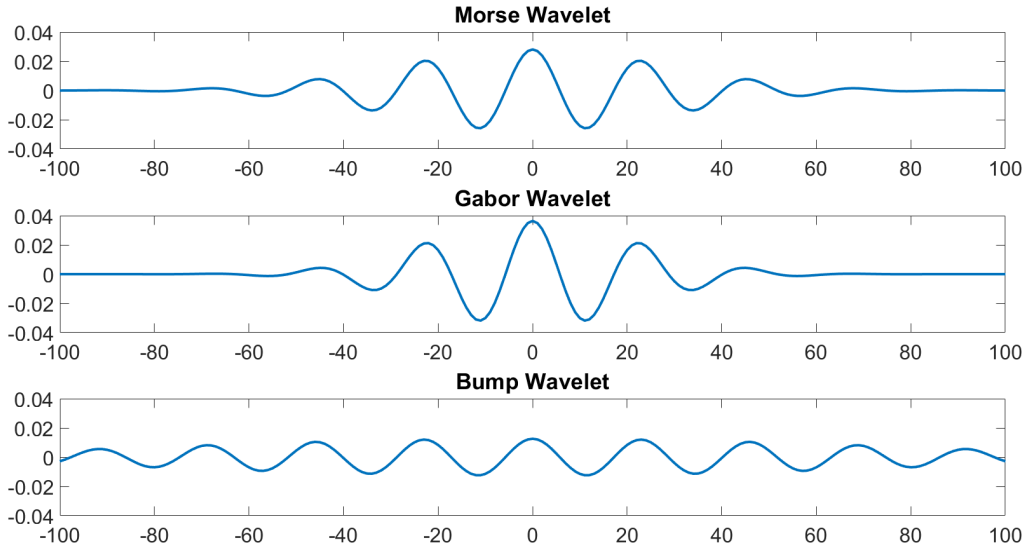

Figure 4.10: Display of Morse, Gabor, and Bump wavelets.

Biometric Matching Model

We build our biometric matching models with distance metrics, baseline machine learning algorithms, and well-known deep learning architectures. For distance metric approach, we compute the average of the training data of the same subject and treat the averaged result as the representative of that subject. During the identification stage, we recognize the subject by matching the SCG pattern to the person with the maximum similarity index in the database. As for machine and deep learning techniques, we train the models with the training data as input and evaluate the performance of the biometric system

on the testing data.

The selected distance metrics are Minkowski distance of orders 1, 2, ∞, and the structural similarity metric. Minkowski distance has been renowned for measuring the similarity between two vectors [50], and the definition can be expressed as

$$D(x,y) = (\sum_{i=1}^{n} |x_i - y_i|^p)^{\frac{1}{p}}, \tag{4.6}$$

where x and y are the two vectors to be compared with and subscript i stands for the i^{th} point in the vector. Symbol p represents the order of the Minkowski distance. Typically used metrics are Euclidean distance and Manhattan distance, in which $p = 2$ is the case for the former and $p = 1$ for the latter. Furthermore, when p approaches infinity, the metric is known as the Chebyshev distance, and is defined as

$$\lim_{p \to +\infty} D(x,y) = max(|x_i - y_i|). \tag{4.7}$$

In this study, Manhattan distance, Euclidean distance, and Chebyshev distance are explored, and given the inputs being the wavelet transformed 2D scalograms, we flatten the 2D matrix into a 1D vector to accommodate with Minkowski distances.

The structural similarity metric is defined in Wang *et al.*'s research work [109] as

$$SSIM(x,y) = \frac{(2\mu_x\mu_y + c_1)(2\sigma_{xy} + c_2)}{(\mu_x^2 + \mu_y^2 + c_1)(\sigma_x^2 + \sigma_y^2 + c_2)}, \tag{4.8}$$

where

$$c_1 = (0.01L)^2,$$

$$c_2 = (0.03L)^2.$$

Inputs x, y are two images; μ_x, μ_y are the averages of the two input images; σ_x, σ_y, and σ_{xy} are the variances of image x and image y and the covariance of the two images x, y. L is the range of the pixel values. In this work, images x and y represent the two SCG patterns to be compared with.

The experimented ML algorithms include k-nearest neighbor (KNN) [59], support vector machine (SVM) [101], decision tree [12], random forest (RF) [68], AdaBoost [32], and naive Bayes [92]. KNN utilizes similarity measure to cluster the data and identifies the wavelet pattern as the subject with the nearest pattern. SVM leverages a combination of hyper-planes to identify the regions of each subject's SCG pattern. Decision trees learn the SCG pattern of each subject through recursive partitioning of the data. RF consists of an ensemble of decision trees. Each individual tree predicts the subject's identity, and the result is generated through the majority voting process. AdaBoost is one of the boosting algorithms, which predicts the subject identity through a combination of weak learners. Naive Bayes assumes the independency between each subject's SCG pattern and constructs the biometric system probabilistically.

The chosen deep learning models are the renowned AlexNet [64] and ResNet-50 [38] architectures. Both networks have outstanding performance in image classification. AlexNet consists of 5 convolutional layers and 3 fully connected (FC) layers with some operations involved between the layers. The involved operations contain ReLU right after every convolutional and FC layer and dropout layers before the first two FC layers. ResNet-50 is a 50 layer neural network model containing residual blocks. The 50 layers are composed of one layer of convolutional neural network (CNN), four stages of stacking

CNN blocks, and one softmax layer. In addition, ResNet-50 also contains activation, pooling, and batch normalization functions.

4.2.3 Experimental Setup and Results

Dataset

The dataset used in this study is the combined ECG and SCG measurement data [34] from the publicly available PhysioNet database [36]. The dataset includes SCG, ECG, and breathing data from 20 presumed healthy subjects. The data were acquired using a Biopac MP36 data acquisition system, and the data sampling rate is 5k Hz. During the measurement, the 20 subjects were asked to be very still in supine position and stay awake. Their data were collected for a total of one hour, including the first 5 minute, the next 50 minutes, and the last 5 minutes. During the middle 50 minutes, the subjects listened to classical music.

Experimental Setting

Training and Testing Datasets

We use the first five minute SCG data as training dataset and the last five minute SCG data as testing dataset. After cleaning and segmenting the SCG data, we arrive at a total of 6835 training data samples and 6862 testing data samples.

Design

We set up different experiments to explore the efficacy of wavelet transform together with deep CNN models for SCG biometrics. For SCG biometric model construction, the experiment consists of either 1D or 2D SCG being utilized to build biometric models with distance metric strategies, baseline machine learning algorithms, or deep learning architectures. For the relation between wavelet features

and subject identity, we visualize the wavelet transformed SCG and the activations of deep CNN model by following the method used in Byeon *et al.*'s study [17]. More specifically, we carry out the following five comparison experiments:

- **Comparison of different mother wavelets:** SCG data are continuously transformed with Morse, Gabor, or Bump mother wavelets.
- **Comparison of different biometric matching models:** SCG biometric matching methods are experimented with distance metrics, ML algorithms, and deep CNN models. Distance metrics are composed of Euclidean distance, Manhattan distance, Chebyshev distance, and structural similarity metric. ML algorithms include k-nearest neighbor, support vector machine, random forest, AdaBoosting, decision tree, and naive Bayes. Deep CNN models consist of AlexNet and ResNet-50.
- **Comparison of raw and processed SCG:** To evaluate the effect of signal pre-processing, we perform SCG identification on both pre-processed and raw SCG signals.
- **Comparison of wavelet transformed data in different subjects:** We conduct qualitative analysis on the Morse wavelet transformed SCG data to identify whether visible difference can be observed among different subjects.
- **Comparison of extracted wavelet features from deep learning models:** We visualize the activations of the first convolution layer of the ResNet-50 model on scalograms to perceive the features extracted from each mother wavelet.

Implementation

We ran all the experiments on MATLAB 2019B. To reasonably reduce the computation complexity, we compress the wavelet transformed SCG image to a size of 80×80. For machine learning

classifiers, we set the classification number to 20 since we have 20 subjects. All the machine learning classifiers were built by using the default parameters in MATLAB 2019B. For training process of deep learning, we use adam optimizer [61] with learning rate 0.0001. Based on the size of the SCG dataset, we set the mini-batch size to 50. We found that 20 epochs were enough for the models to converge, so we set 20 as the number of the epoch for our experiments.

Evaluation Metric

For identification problem, we use the recognition rate as the evaluation metric. The recognition rate is the percentage of the correctly identified testing sequences. For authentication issue, we assess the performance of the model with the equal error rate (EER), which is the threshold value of false acceptance rate and false rejection rate.

Quantitative Results

Table 4.4: Performance of the proposed seismocardiogram biometric models on raw data

Method	1-D SCG		Morse Wavelet		Gabor Wavelet		Bump Wavelet	
	Recognition Rate (%)	Equal Error Rate (%)	Recognition Rate (%)	Equal Error Rate (%)	Recognition Rate (%)	Equal Error Rate (%)	Recognition Rate (%)	Equal Error Rate (%)
Structural Similarity	96.8	2.56	99.8	0.012	99.8	0.012	99.4	0.27
Euclidean Distance	99.8	0.01	98.5	1.25	98.6	1.25	97.4	2.63
Manhattan Distance	99.7	0.26	98.8	1.24	98.9	1.24	97.9	1.67
Chebyshev Distance	93.7	5.3	94.4	5.22	94	5.22	89.1	9.27
kNN	99.9	0.005	99.7	0.016	99.7	0.015	99.2	0.27
SVM	99.9	0.002	90.8	7.25	90	7.76	71.9	16.5
Decision Tree	96.2	2.73	95.1	1.82	95.5	1.94	98.2	1.5
RF	99.4	0.53	99.4	0.24	98.6	0.31	99.4	0.26
AdaBoost	99.4	0.78	98.1	1.4	98.8	1.32	99.5	0.52
Naive Bayes	99.2	0.51	94.9	2.53	94.9	2.33	94.8	2.57
AlexNet	99.7	0.25	97.4	1.87	94.8	2.83	96.6	2.3
ResNet-50	87.6	7.52	99.8	0.008	99.8	0.008	**100**	**0**

Table 4.5: Performance of the proposed seismocardiogram biometric models on pre-processed data

Method	1-D SCG		Morse Wavelet		Gabor Wavelet		Bump Wavelet	
	Recognition Rate (%)	Equal Error Rate (%)	Recognition Rate (%)	Equal Error Rate (%)	Recognition Rate (%)	Equal Error Rate (%)	Recognition Rate (%)	Equal Error Rate (%)
Structural Similarity	96.9	2.45	99.8	0.22	99.8	0.015	99	0.55
Euclidean Distance	99.8	0.01	98.5	1.25	98.5	1.25	96.7	3.14
Manhattan Distance	99.7	0.26	98.6	1.23	98.7	1.23	97.5	1.67
Chebyshev Distance	93.8	5.32	94.3	5.22	94	5.22	89.2	9.28
kNN	99.9	0.005	99.7	0.017	99.7	0.015	99.2	0.27
SVM	99.8	0.008	92.2	6.37	90.2	7.07	77.3	15.1
Decision Tree	96.8	2.45	94.9	1.6	95.3	1.77	96.1	1.98
RF	99.7	0.25	99.8	0.24	99.2	0.28	99.9	0.24
AdaBoost	99.5	0.52	98.6	1.33	98.7	1.32	99.6	0.52
Naive Bayes	99.2	0.51	94.9	2.33	94.9	2.33	94.8	2.57
AlexNet	99.8	0.24	94.2	2.85	95.7	3.95	94.3	3.81
ResNet-50	86.2	5.25	99.9	0.004	99.2	0.54	99.3	0.53

We show the recognition rate and EER of each model in Tables 4.6 and 4.7. Table 4.6 presents the performance of biometric matching models built on raw one-dimensional SCG data and wavelet transformed SCG data without signal pre-processing. Table 4.7 exhibits similar results as Table 4.6 does, but different from Table 4.6, both one-dimensional and wavelet transformed SCG data have gone through the signal processing step.

Judging from the EER presented in the two tables, we show that our best SCG biometric model has 0% equal error rate and 100% recognition rate, which is produced by the Bump wavelet transformed pattern along with the ResNet-50 model. Considering one-dimensional SCG case, we observe that SVM and kNN generate the best results with a recognition rate of $\approx 99.9\%$ and an EER of $\approx 0.005\%$, no matter the one-dimensional SCG data is processed or not. Regarding the wavelet transformed time-frequency pattern, ResNet-50, structural similarity, and kNN models excel with consistently over 99% recognition rate and $< 0.3\%$ EER. Focusing on the performance of the three wavelet functions in average, we see that Morse wavelet has high recognition rate, and Bump wavelet favors the decision tree and AdaBoost algorithms.

Examining the effect of signal processing, we observe that data processing generally elevates the performance of one-dimensional SCG biometric and machine-learning based biometric matching models. On the basis of the EER of one-dimensional SCG biometric models, we notice that processed SCG favors all the models except a slightly higher EER in Chebyshev distance and SVM models. With respect to wavelet transformed time-frequency patterns, we infer from Tables 4.6 and 4.7 that signal processing basically improves the machine learning-based biometric models, especially SVM models. Conversely, deep learning and distance metrics do not seem to benefit from signal processing. We discover that all distance similarity approaches have either equal or higher EER in processed wavelet transformed SCG data. Referring to deep learning technique, we spot that only Morse wavelet transform gains slight advantage from signal processing, while Gabor and Bump wavelets do not.

Qualitative Results

We show the recognition rate and EER of each model in Tables 4.6 and 4.7. Table 4.6 presents the performance of biometric matching models built on raw one-dimensional SCG data and wavelet transformed SCG data without signal pre-processing. Table 4.7 exhibits similar results as Table 4.6 does, but different from Table 4.6, both one-dimensional and wavelet transformed SCG data have gone through the signal processing step.

Judging from the EER presented in the two tables, we show that our best SCG biometric model has 0% equal error rate and 100% recognition rate, which is produced by the Bump wavelet transformed pattern along with the ResNet-50 model. Considering one-dimensional SCG case, we observe that SVM and kNN generate the best results with a recognition rate of $\approx 99.9\%$ and an EER of $\approx 0.005\%$, no matter the one-dimensional SCG data is processed or not. Regarding the wavelet transformed time-frequency pattern, ResNet-50, structural similarity, and kNN models excel with consistently over 99% recognition

Table 4.6: Performance of the proposed seismocardiogram biometric models on raw data

Method	1-D SCG		Morse Wavelet		Gabor Wavelet		Bump Wavelet	
	Recognition Rate (%)	Equal Error Rate (%)	Recognition Rate (%)	Equal Error Rate (%)	Recognition Rate (%)	Equal Error Rate (%)	Recognition Rate (%)	Equal Error Rate (%)
Structural Similarity	96.8	2.56	99.8	0.012	99.8	0.012	99.4	0.27
Euclidean Distance	99.8	0.01	98.5	1.25	98.6	1.25	97.4	2.63
Manhattan Distance	99.7	0.26	98.8	1.24	98.9	1.24	97.9	1.67
Chebyshev Distance	93.7	5.3	94.4	5.22	94	5.22	89.1	9.27
kNN	99.9	0.005	99.7	0.016	99.7	0.015	99.2	0.27
SVM	99.9	0.002	90.8	7.25	90	7.76	71.9	16.5
Decision Tree	96.2	2.73	95.1	1.82	95.5	1.94	98.2	1.5
RF	99.4	0.53	99.4	0.24	98.6	0.31	99.4	0.26
AdaBoost	99.4	0.78	98.1	1.4	98.8	1.32	99.5	0.52
Naive Bayes	99.2	0.51	94.9	2.53	94.9	2.33	94.8	2.57
AlexNet	99.7	0.25	97.4	1.87	94.8	2.83	96.6	2.3
ResNet-50	87.6	7.52	99.8	0.008	99.8	0.008	**100**	**0**

rate and $< 0.3\%$ EER. Focusing on the performance of the three wavelet functions in average, we see that Morse wavelet has high recognition rate, and Bump wavelet favors the decision tree and AdaBoost algorithms.

Examining the effect of signal processing, we observe that data processing generally elevates the performance of one-dimensional SCG biometric and machine-learning based biometric matching models. On the basis of the EER of one-dimensional SCG biometric models, we notice that processed SCG favors all the models except a slightly higher EER in Chebyshev distance and SVM models. With respect to wavelet transformed time-frequency patterns, we infer from Tables 4.6 and 4.7 that signal processing basically improves the machine learning-based biometric models, especially SVM models. Conversely, deep learning and distance metrics do not seem to benefit from signal processing. We discover that all distance similarity approaches have either equal or higher EER in processed wavelet transformed

Table 4.7: Performance of the proposed seismocardiogram biometric models on pre-processed data

Method	1-D SCG		Morse Wavelet		Gabor Wavelet		Bump Wavelet	
	Recognition Rate (%)	Equal Error Rate (%)	Recognition Rate (%)	Equal Error Rate (%)	Recognition Rate (%)	Equal Error Rate (%)	Recognition Rate (%)	Equal Error Rate (%)
Structural Similarity	96.9	2.45	99.8	0.22	99.8	0.015	99	0.55
Euclidean Distance	99.8	0.01	98.5	1.25	98.5	1.25	96.7	3.14
Manhattan Distance	99.7	0.26	98.6	1.23	98.7	1.23	97.5	1.67
Chebyshev Distance	93.8	5.32	94.3	5.22	94	5.22	89.2	9.28
kNN	99.9	0.005	99.7	0.017	99.7	0.015	99.2	0.27
SVM	99.8	0.008	92.2	6.37	90.2	7.07	77.3	15.1
Decision Tree	96.8	2.45	94.9	1.6	95.3	1.77	96.1	1.98
RF	99.7	0.25	99.8	0.24	99.2	0.28	99.9	0.24
AdaBoost	99.5	0.52	98.6	1.33	98.7	1.32	99.6	0.52
Naive Bayes	99.2	0.51	94.9	2.33	94.9	2.33	94.8	2.57
AlexNet	99.8	0.24	94.2	2.85	95.7	3.95	94.3	3.81
ResNet-50	86.2	5.25	99.9	0.004	99.2	0.54	99.3	0.53

SCG data. Referring to deep learning technique, we spot that only Morse wavelet transform gains slight advantage from signal processing, while Gabor and Bump wavelets do not.

Qualitative Results

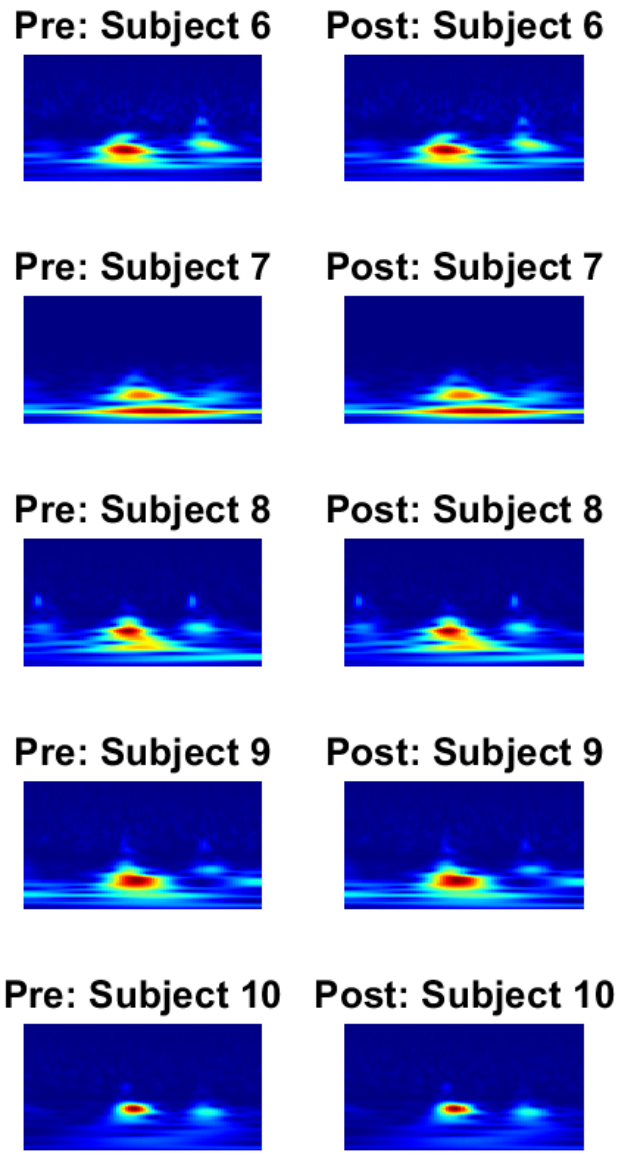

Figure 4.11: Demonstration of Morse wavelet transformed SCG from 5 subjects. The left column shows the SCG before listening to the music; the right column displays the SCG after listening to the music. The horizontal axis represents time of one second length, whereas the vertical axis stands for the frequency.

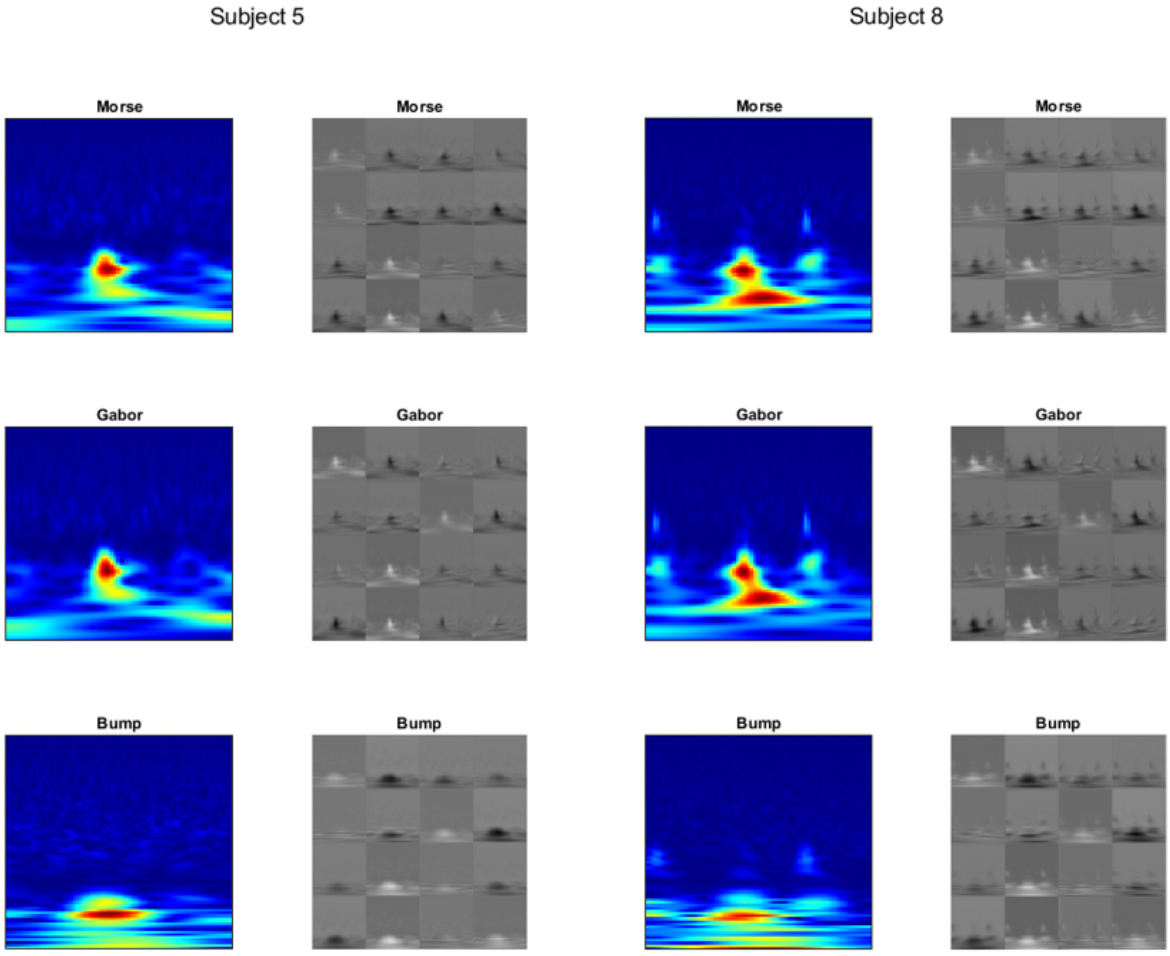

Figure 4.12: Comparison of the activations of the first convolution layer in ResNet-50 between two subjects. The left subplots display the scalograms and activations of subject 5, whereas the right subplots showcase the data from subject 8.

To further validate the high recognition rate achieved, we conduct qualitative analysis including the Morse wavelet transformed SCG as shown in Fig. 4.11 and ResNet-50 first convolution layer activations as displayed in Fig. 4.12. In Fig. 4.11, we observe not only the perceptual difference between each two subjects but also the visual similarity between different SCG data of the same subject. For example, subject 10 has relatively narrow frequency band, while subject 7 has wider frequency span. Such observation is made from focal circle in subject 10's SCG pattern and wider colorful shapes exhibited in subject 7. Another example is the difference observed between subject 8 and subject 9. From a global view,

subject 9 has a relatively focal pattern in comparison with subject 8, which can be claimed from some focal patterns in subject 9 versus the mixture of several frequencies spanning over 1 second in subject 8. Considering the pattern similarity of the same subject, we observe high time-frequency consistency in the occurrence of SCG peak and its neighboring components.

In Fig. 4.12, we showcase the neural network activations of two subjects to visualize the wavelet features extracted by the ResNet-50 model. Comparing the features of the three wavelets, we observe that Bump wavelet captures narrower frequencies with longer duration, whereas Morse and Gabor wavelets obtain features with wider frequency bands and shorter periods. Such observation is logical since the amplitude of Morse and Gabor wavelets decay faster than Bump wavelet does (see Fig. 4.10). In addition, we perceive various kinds of patterns learned in ResNet-50. For instance, we identify low frequency components acquired near the center of SCG, high frequency patterns activated in the upper part of SCG, and several complex edges learned by the deep CNN model.

Comparison with State-of-the-art

Table 4.8: Comparison to the State-of-the-art

Subject Number	SCG Length	Method	Recognition Rate (%)	Equal Error Rate (%)
20	Unmentioned	[15]	98.89	Unmentioned
20	Single SCG, 1s	ours	**100**	**0**

We compare our best SCG biometric model to the existing SCG biometric models in Table 4.8, and our results outperform the state-of-the-art. In Bui *et al.*'s work [15], principal component analysis is employed to achieve satisfying SCG identification. In this study, we show that combining continuous wavelet transform and deep learning model, or even processed SCG signal in conjunction with machine learning classifiers, can improve the SCG biometric recognition rate by at least 1%.

Apart from the recognition rate and EER, we consider the results comparable since both Bui *et al.*'s and our models are built on the SCG data collected from 20 healthy subjects. Furthermore, we demonstrate that our SCG biometric model requires only one SCG in each sequence to accomplish biometric verification.

4.2.4 Conclusions

In this study, we demonstrate that seismocardiogram could be a promising biometric. Applying wavelet transform to SCG signals, we show that ResNet-50 model fulfills 100% recognition rate performance and structural similarity approach presents larger than 99% recognition rate. In addition, we exhibit that kNN and SVM biometric models achieve 99.9% recognition rate and $< 0.01\%$ EER on cleaned one-dimensional SCG data. In our qualitative results, the individual difference of SCG is reasonably perceivable, and the complex wavelet features are learned by the deep CNN models. Based on our findings, we believe that SCG biometric is worth exploring, and we are eager to identify the characteristic points in SCG that distinguish between individuals in the future.

4.3 Challenge in Biometric Identification for Motion Artifact Resilient SCG

Today, biometric authentication systems have been widely applied to human identity verification to perform high level security. We illustrate a standard structure in Figure 4.13. Typical biometric authentication systems consist of three functional blocks: data cleaning, features processing, and matching evaluation. The matching score will then be utilized to identify the subject's identity. In modern society, face and fingerprint are commonly used biometrics [63]. However, such external biometrics are susceptible to spoofing attacks [119]. For instance, fingerprints are easily left on an object and recreated with latex; facial recognition can be hacked by high-resolution modified photos.

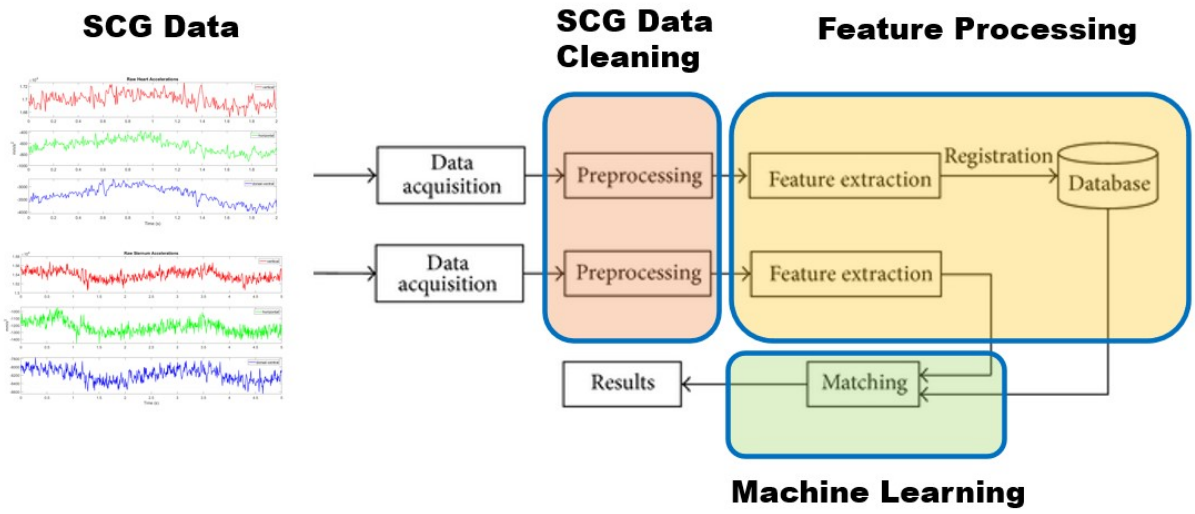

Figure 4.13: Schematics of the standard biometric system in conjunction with our contributions. Red box represents our SCG data cleaning technique. Yellow box stands for extracting features. Green box stands for our pattern matching strategies, which include distance similarity and machine learning approaches.

In this paper, we propose different SCG biometric authentication models adjustable to a person's

posture, and we make contributions as follows:

- generate robust SCG biometrics with the devised signal processing procedure
- present state-of-the-art performance motion artifact resilient SCG biometric models

The rest of the section is organized as follows. We describe the experimental design and SCG model construction in subsection 4.3.2. Subsequently, we present the performance of each proposed SCG biometric authentication model and discuss our experimental results in subsection 4.3.3. Finally, we make conclusions of this work in subsection 4.3.4.

4.3.1 Related Works

To circumvent the issues in external biometrics, physiological signals such as electrocardiograms (ECG) or seismocardiograms (SCG) has attracted attention as a biometric recently. Both ECG and SCG are continuous measures and reveal quasi-periodic cardiac morphology. ECG measures electrical depolarization and repolarization throughout cardiac activities; SCG captures the chest's surface motion caused by the contraction of the heart [54]. Physiological signals are able to reflect the functioning of an individual's cardiovascular system; furthermore, they show several advantages as a biometric [47]: (1) indicate liveness; 2) difficult to be stolen; (3) easy to acquire with wearable sensors.

ECG has been reported as a promising biometric in several studies [78] [111], yet to the best of our knowledge, the uniqueness of SCG [15] has only been reported in two studies: one is conducted by Bui *et al.* [15], and the other is by Hsu *et al.* [46]. In Bui *et al.*'s work, a 98.89% recognition rate has been reported by manipulating SCG data, but the authentication issue is untouched. In Hsu *et al.*'s study, state-of-the-art SCG biometric performance has been presented, however, it is only adaptable for SCG measured at supine positions.

4.3.2 Methodology and Experimental Design

We first introduce our experiment design. Following that, we describe the signal processing strategy of the sensor data. Next, we propose our SCG-based biometric models. Last, we specify the performance quantification of the proposed biometric authentication model.

Experiment Design

This study was approved by the Jen-Ai Hospital-Joint Institutional Review Board. We recruited 20 young healthy volunteer to undergo the data acquisition process. All 20 subjects voluntarily provided the written informed consent to participate in the study. The age of the participants are $25-32$ years, and the gender distribution is 6 females and 14 males.

Table 4.9: Design of Experiments

Activities	sitting, standing, walking, sitting after walking
Duration	each activity lasts for 3 minutes
Sensor Placements	left/right wrists, heart, sternum, neck near left carotid artery
Description	participants wear the sensors throughout the whole experiment
Sensor	three-axis accelerometers
Measurements	accelerations

We summarize the experimental design in Table 4.9. All the participants went through the four activities: sitting still, standing still, walking at normal pace, and sitting right after walking. For each activity, the participant performs either the same posture or consistent motion (walking) for three minutes with the wearable sensors placed on the body.

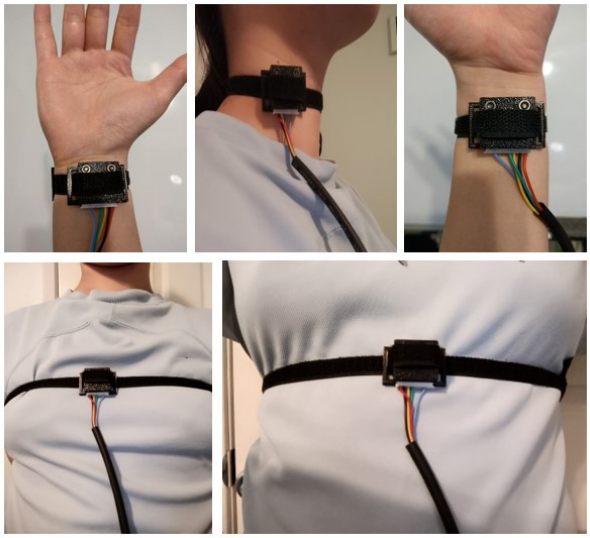

Figure 4.14: Demonstration of the sensor placements.

The collected data are body acceleration measured by the wearable sensors. Throughout the whole experiment, the acceleration data are measured with the sensors placed on the participant's heart, sternum, left carotid, and bilateral wrists (as shown in Fig. 4.14). These body parts are chosen since it is very likely to measure the heart-induced signals at these locations [103]. The acceleration sensors are MPU-6050, and the data sampling rate is set to 150Hz in our experiment. All the data acquisition was completed by the same person; moreover, before the start of each activity, the person inspected all the sensors to be well-functioning and properly leveled.

Data Processing

We transform the raw acceleration signals into data samples for biometric model construction in five steps: 1) data normalization, 2) low-frequency noise removal, 3) high-frequency noise removal, 4) data smoothing, and 5) heartbeat peak detection. To be more specific, the whole signal processing procedure is applied to each dimensional acceleration independently. In the first step, we compute the average of each dimensional acceleration and subtract the raw signal by this average so as to remove

the gravity effect and other constant acceleration factor, which is known as common average referencing (CAR) and was adopted in [20]. In the second step, we make use of the third order Savitzky-Golay filter to clean the unwanted low-frequency signal. Such approach has been shown effective in removing motion artifact in [84]. In the third step, we remove the high-frequency noise with a sixth-order Butterworth lowpass filter. In the fourth step, we smooth the data through interpolating the processed signal with spline cubic curves at 750Hz. We portrait the raw and processed acceleration signals of the sensor located on top of the heart in Figures 4.15 and 4.16. In the final step, we borrow the heartbeat detection technique used in [20] to label the heart pumping peaks in SCG. Herein, the SCGs measured on the heart are employed. Moreover, we chunk the acceleration data into 1-second long SCG centered at the labeled heartbeat peak to standardize the data samples.

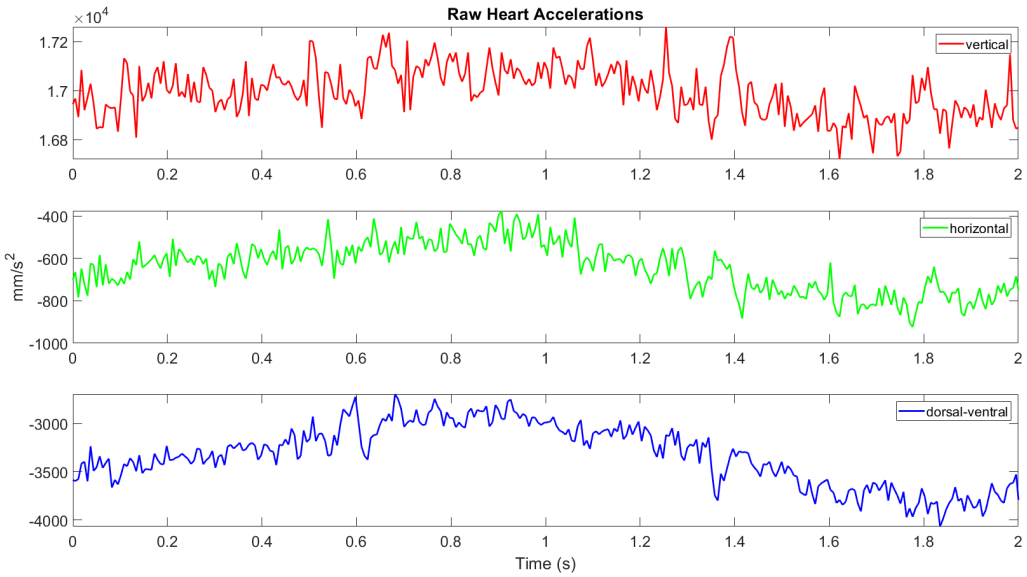

Figure 4.15: Demonstration of the two-second raw and processed SCG data. Red: Vertical; Green: Horizontal; Blue: Dorsal-ventral.

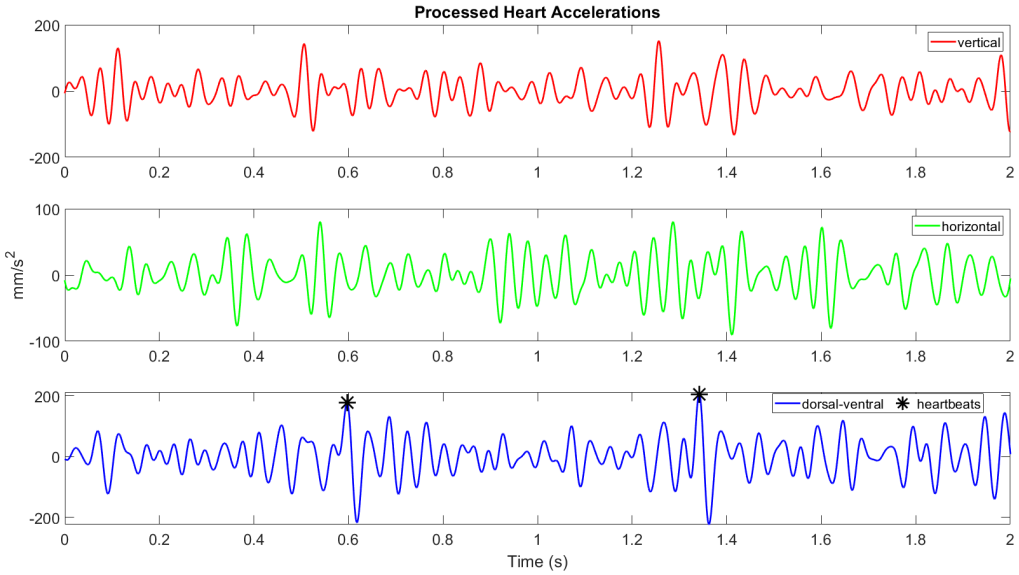

Figure 4.16: Demonstration of the two-second processed SCG data. Red: Vertical; Green: Horizontal; Blue: Dorsal-ventral.

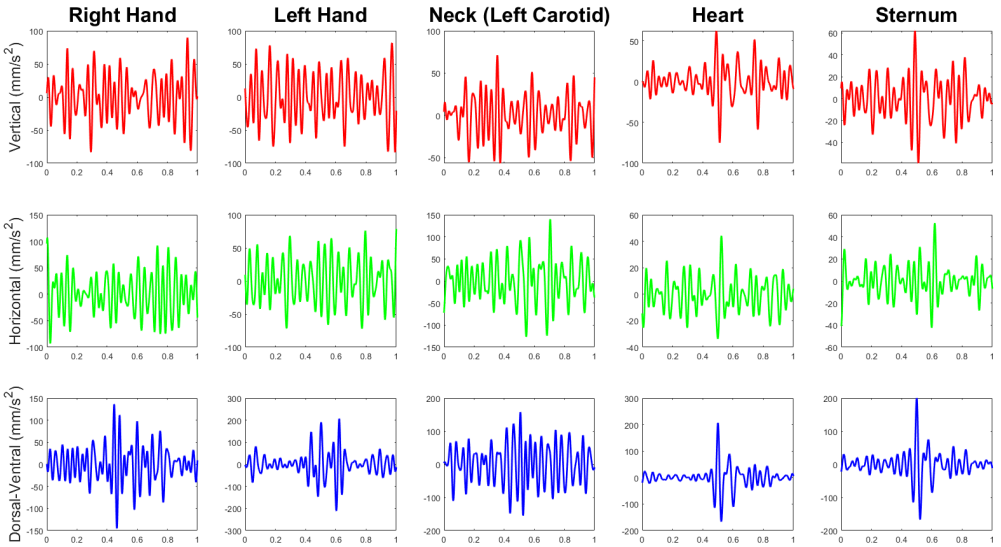

Figure 4.17: Demonstration of the 1-second ensemble average SCG waveforms.

Biometric Authentication Model

We devise the SCG-based biometric authentication models considering the following four factors: (1) orientation of the acceleration, (2) locations of the sensor, (3) posture of the human subject, and (4) resilience against motion artifact. For (1), we have 3-axis accelerations for each sensor. Regarding (2), we place 5 sensors on different body parts. As for (3), the participants perform 4 different activities, ranging from small movement to large motion. Concerning (4), we leverage the ensemble average trick applied in other SCG studies [53] [54]. To be more specific, instead of using the data sample directly, we remove the motion artifact through averaging five consecutive data samples and build the biometric models using the averaged data. We display the averaged acceleration for building the biometric authentication models in Fig. 4.17. Consequently, we build a total of 120 models, in which $120 = 3 \times 5 \times 4 \times 2$.

For each model, we adopt support vector machine, a well-known machine learning approach, to learn classifying the twenty subjects' identity based on their processed acceleration data. In our training-testing data segregation, we randomly shuffle the samples and then assign the first 70% as the training dataset with the rest 30% as the testing dataset.

Performance Evaluation

For authentication, we assess the performance of the model with the equal error rate (EER), which is the threshold value of false acceptance rate and false rejection rate. EER has been widely known as a standard for the authentication issue.

4.3.3 Experiment Results

We exhibit the EER of each experiment in Table 4.10, and we showcase the competitiveness of the proposed SCG biometric authentication systems in Table 4.11. Our best SCG biometric model is the

robust standing heart dorsal-ventral acceleration, which has an EER less than 0.1%. We also plot the training and testing SCG of two subjects in Fig. 4.18. From the plot, we can clearly perceive the high SCG consistency of the same human participant and dissimilarity of SCG between different people.

Table 4.10: equal error rate of the SCG-based biometric models

Sensor Location & Acceleration Axis	Sit EER	Resilient Sit EER	Stand EER	Resilient Stand EER	Walk EER	Resilient Walk	Post-exercise EER	Resilient Post-exercise EER
Right Hand Vertical	0.45	0.14	0.47	0.15	0.35	0.25	0.45	0.20
Right Hand Horizontal	0.49	0.17	0.47	0.19	0.50	0.29	0.48	0.19
Right Hand Dorsal-Ventral	0.49	0.18	0.47	0.15	0.52	0.23	0.49	0.18
Left Hand Vertical	0.47	0.16	0.47	0.13	0.52	0.26	0.47	0.13
Left Hand Horizontal	0.48	0.17	0.48	0.18	0.51	0.29	0.48	0.19
Left Hand Dorsal-Ventral	0.46	0.13	0.47	0.20	0.48	0.21	0.47	0.20
Left Carotid Vertical	0.43	0.09	0.40	0.06	0.49	0.19	0.41	0.09
Left Carotid Horizontal	0.43	0.13	0.47	0.15	0.49	0.25	0.45	0.12
Left Carotid Dorsal-Ventral	0.46	0.12	0.45	0.14	0.49	0.23	0.48	0.11
Heart Vertical	0.28	0.01	0.28	0.01	0.44	0.06	0.30	<0.001
Heart Horizontal	0.37	0.05	0.35	0.003	0.45	0.13	0.37	0.02
Heart Dorsal-Ventral	0.33	0.02	0.26	<0.001	0.41	0.06	0.31	0.02
Sternum Vertical	0.27	0.01	0.28	0.003	0.45	0.06	0.31	<0.001
Sternum Horizontal	0.36	0.04	0.33	0.006	0.43	0.14	0.36	0.02
Sternum Dorsal-Ventral	0.32	0.01	0.28	0.003	0.41	0.04	0.31	0.01

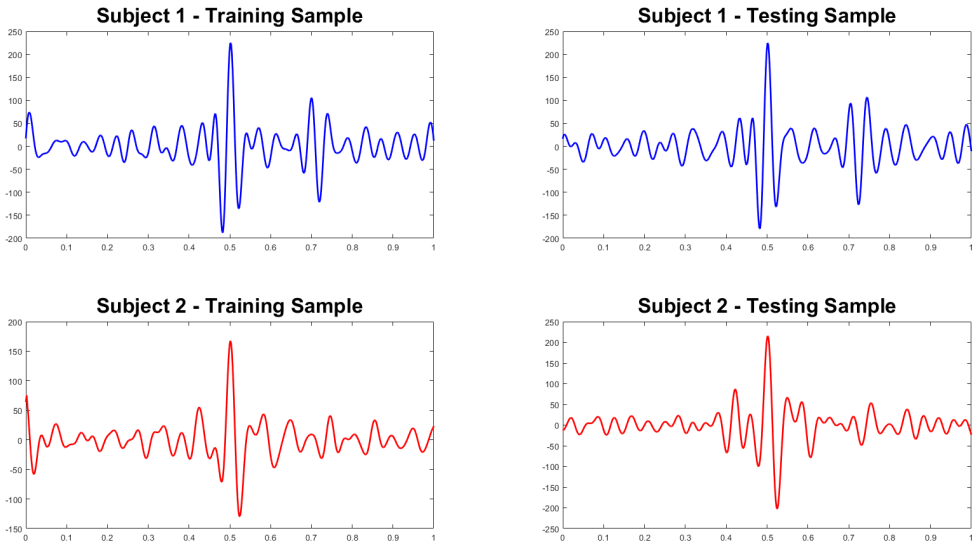

Figure 4.18: Demonstration of training and testing samples from two subjects.

Best Sensor Location

Judging from the EER of the same posture and signal processing method, we discover that either the heart or the sternum is the most appropriate location to place the accelerometer for authentication. Moreover, the vertical and dorsal-ventral accelerations are more reliable than the horizontal orientation. Ranking afterwards is the left carotid, at which the vertical acceleration appears to be the most suitable biometric. Placing the sensor on the wrists gives rise to the worst authentication performance. Nevertheless, in the walking motion without robust signal processing, we notice that the vertical acceleration from the right hand wrist shows the lowest EER compared to all other accelerations. This could possibly imply that the walking pattern is recognized in the hand waving movement.

Best Posture

Among the four activities, standing results into the optimal posture for authentication, following by post-exercise, sitting, and walking. The lowest EER for each of these activities are 0.01%, 0.02%, 0.98%, and 4.18%, respectively. The results could probably imply that both large and restricted motions like walking and sitting would lead to worse authentication models. On the contrary, standing normally and sitting post-exercise are relatively natural posture for the human participants. Therefore, we spot better SCG-based biometric authentication models in these two postures.

Efficacy of the Motion Artifact Resilient Method

Owing to the fact that SCG is susceptible to motion artifact [20] [103], we propose the motion artifact removal strategy and showcase its efficacy in Table 4.10. For all the experiments, the robustness enhanced biometric authentication models are favored.

Table 4.11: comparison of SCG EER to state of the art

Method	EER (%)	Posture
PCA on SCG [15]	not reported	unmentioned
Wavelet Transform SCG [46]	< 0.01	supine
Ours - vertical SCG	0.98	Sitting
Ours - dorsal-ventral SCG	0.01	Standing
Ours - sternum dorsal-ventral SCG	4.18	Walking
Ours - sternum vertical SCG	0.02	Post-exercise

Comparison with the State-of-the-Art Works

We compare our SCG-based biometric authentication models with other existing studies in Table 4.11. We display the competency of the proposed models in allowing the motions generated by the human

body. Although the EER is not lower than the supine SCG, we still present $< 1\%$ EER in sitting, post-exercise sitting, and standing positions. Furthermore, we demonstrate that our model is able to handle walking SCG and leverage it as a biometric.

4.3.4 Conclusions

We demonstrate that seismocardiogram could be a promising biometric even with a person in motions. Through the exploration of tri-axial accelerations of different body parts, we reveal that placing the accelerometer near the heart or the sternum produces robust signals for biometric authentication. Moreover, we exhibit that standing is the most appropriate posture for biometric authentication compared to sitting and walking. Based on our findings, we believe that SCG biometric is worth exploring, and we are eager to identify the characteristic points in SCG under motion that distinguish between individuals in the future.

4.4 Acknowledgments

Chapter 4 contains reprints of P.-Y. Hsu, P.-H. Hsu, and H.-L. Liu, “Fold Electrocardiogram Into a Fingerprint.”, *Proc. IEEE/CVF Conference on Computer Vision and Pattern Recognition Workshops*, 2020., P.-Y. Hsu, P.-H. Hsu, and H.-L. Liu, “Exploring Seismocardiogram Biometrics with Wavelet Transform”, *IEEE International Conference on Pattern Recognition*, 2021; and P.-Y. Hsu, P.-H. Hsu, T.-H. Lee, and H.-L. Liu, “Motion Artifact Resilient SCG-based Biometric Authentication Using Machine Learning”, *Annual International Conference of the IEEE Engineering in Medicine and Biology Society (EMBC)*, 2021;

I would like to thank my coauthors Po-Han Hsu, Tsung-Han Lee, and Hsin-Li Liu for their insightful suggestions on our published works.

Chapter 5

Computational Methodologies for Continuous Blood Pressure Estimation

This chapter presents a motion artifact resilient cuff-less blood pressure monitoring system, which leverages SCG measured by the wearable sensors. The efficacy of this system was validated on 20 healthy young adults.

5.1 Challenge in Continuous Blood Pressure Monitoring

Blood pressure (BP) is a pivotal indicator of the cardiovascular health status of a person. A large number of cardiovascular diseases is substantially related to abnormal BP values. Therefore, wearable BP monitors are in highly requirement to raise early awareness of hypertension and hypotension [5].

In this chapter, we propose a motion artifact resilient BP monitoring model using a fusion of wearable accelerometers. We demonstrate the efficacy of the BP models in 20 young healthy adults. We contribute to:

- building a cuff-less BP monitoring model that fulfills the Association for the Advancement of Medical Instrumentation (AAMI) standard and British Hypertension Society protocol
- achieving motion artifact resilient BP monitoring
- devising robust SCG features for BP monitoring

5.2 Related Works

Nowadays, the frequently adopted techniques include auscultation [86], volume clamping [52], oscillometry [8], and applanation tonometry [27]. All the aforementioned methods require the usage of an inflatable cuff and the person staying still, which indicates the need of improvements in the current techniques.

Some cuff-less BP monitoring approaches have been proposed [20] [60] [88] [120]. According to Chang et al. [20] and Kim *et al.* [60], features extracted from seismocardiography (SCG) and ballistocardiography (BCG) can be employed to monitor BP. In Poon *et al.* 's [88] and Zheng *et al.*'s [120] studies, pulse transit time (PTT) is derived from electrocardiogram (ECG) and photoplethysmography (PPG) to compute BP. Although optimistic results are reported in these studies, the suggested strategies are prone to motion artifacts in the signals and some require further calibrations.

5.3 Methodology and Experimental Design

We first describe the data acquisition method and experimental design. Next, we elaborate on the sensor data processing step. Subsequently, we present the feature extraction approach and the construction of motion artifact resilient blood pressure monitoring model. Last, we specify how we quantify the performance of the proposed model compared to other existing methodology.

5.3.1 Data Acquisition

The current study was approved by the Jen-Ai Hospital-Joint Institutional Review Board. In this study, we recruited 20 young healthy volunteer to undergo the data acquisition process. All 20 subjects willingly provided the written informed consent to participate in the study. The age of the participants lies within $25-32$ years, and the gender distribution is 6 females and 14 males.

Table 5.1: Design of Experiments

Activities	sitting, standing, walking, sitting after walking
Duration	each activity lasts for 3 minutes
Sensor Placements	left/right wrists, heart, sternum, neck near left carotid artery
Description	participants wear the sensors throughout the whole experiment
Sensor	tri-axial accelerometers
Measurements	accelerations and blood pressure

We summarize the experimental design in Table 5.1. All the participants went through the four activities: sitting still, standing still, walking at normal pace, and sitting right after walking. For each activity, the participant performs either the same posture or consistent motion (walking) for three minutes with the wearable sensors placed on the body.

The collected data include body acceleration, systolic blood pressure (SBP), and diastolic blood pressure (DBP). Throughout the whole experiment, the acceleration data are measured with the sensors placed on the participant's heart, sternum, left carotid, and bilateral wrists (as shown in Fig. 4.14). These body parts are chosen since it is very likely to measure the heart-induced signals at these locations. The acceleration sensors are MPU-6050, and the data sampling rate is set to 150Hz in our experiment. During the two sitting activities, the SBP and DBP data are collected using Rossmax MG150f. This blood

pressure monitor was certified by European Society of Hypertension and clinically validated by British Hypertension Society with an A/A grade. All the data acquisition was completed by the same person, who was well trained by an experienced registered nurse to perform blood pressure measuring. Moreover, before the start of each activity, the person inspected all the sensors to be well-functioning and properly leveled. In the experiment, one subject's BP monitoring varies larger than 40 mmHg, and we remove this subject's data from BP model construction.

5.3.2 Signal Processing

We process the raw acceleration signals in four steps: 1) data normalization, 2) low-frequency noise removal, 3) high-frequency noise removal, and 4) data smoothing. To be more specific, the whole signal processing procedure is applied to each dimensional acceleration independently. In the first step, we compute the average of each dimensional acceleration and subtract the raw signal by this average so as to remove the gravity effect and other constant acceleration factor. This strategy was also adopted in [20]. In the second step, we make use of the third order Savitzky-Golay filter to clean the unwanted low-frequency signal. Such approach has been shown effective in removing motion artifact in [84]. In the third step, we remove the high-frequency noise with a sixth-order Butterworth lowpass filter. In the final step, we smooth the data through interpolating the processed signal with spline cubic curves at 750Hz. We portrait the raw and processed acceleration signals of the sensor located on top of the heart in Figures 5.1 and 5.2.

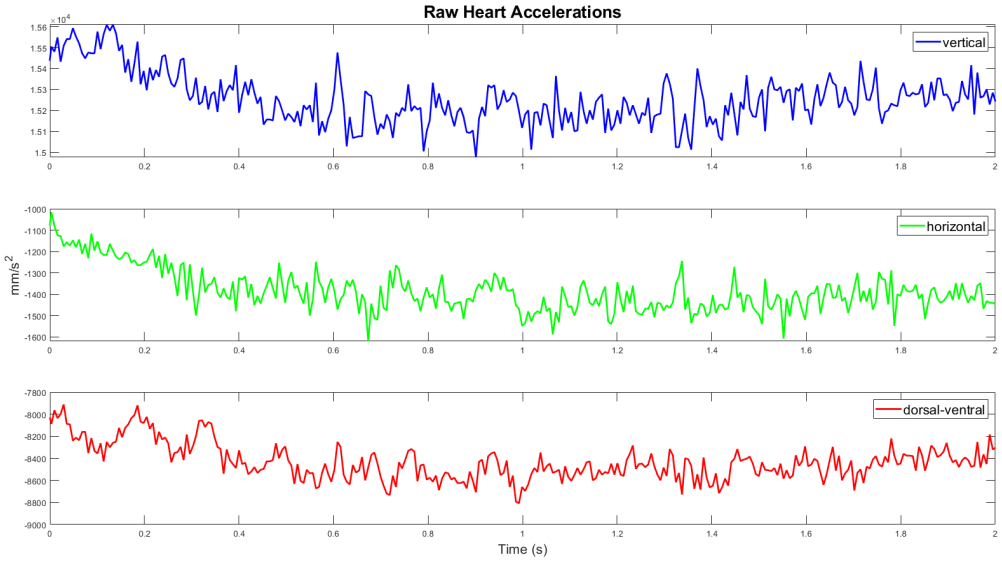

Figure 5.1: Demonstration of the raw data.

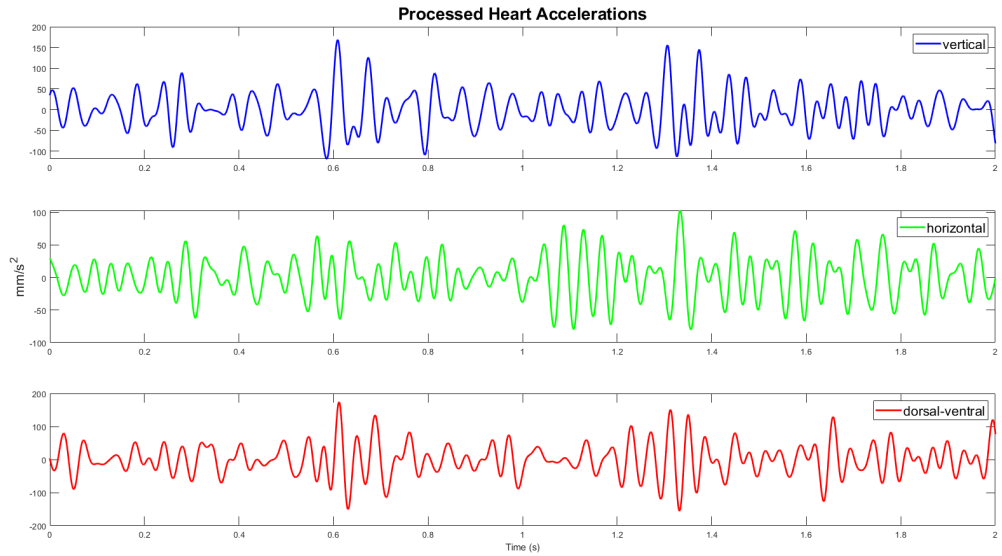

Figure 5.2: Demonstration of the processed data.

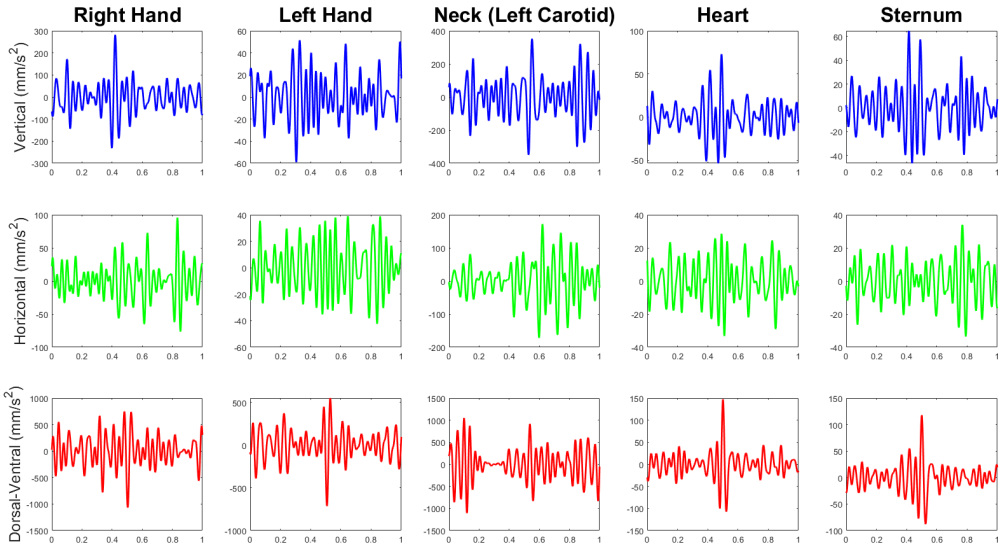

Figure 5.3: Demonstration of the ensemble average acceleration waveforms.

5.3.3 Feature Extraction

Our proposed feature extraction methodology is composed of two major pieces. One is heartbeat identification, and the other is feature construction. For the completion of the first piece, we leverage the methods used in [20] and [41] through a sophisticated combination of the two. In the primary step, we borrow the peak detection method applied in [20]. We select the valid heartbeats where the peaks are observed in both the vertical and dorsal-ventral accelerations with a tolerance of 10ms. Next, we derive the envelope of the dorsal-ventral acceleration and perform the waveform-based heartbeat detection as suggested in [41]. The envelope is constructed using spline interpolation over local maxima separated by at least 200ms, and each envelope packet is expected to enclose one heartbeat. Subsequently, we conduct a false positive removal and search-back for the missing heartbeats through the heartbeat period estimation method detailed in [41].

For feature extraction, we generate the representative waveform first and manipulate the fiducial

point method to construct the feature space. As reported in several SCG related studies [20] [53] [54], due to the body motion artifacts, the SCG varies from heartbeat to heartbeat. Therefore, we strategically align five one-second consecutive acceleration waveform along the heartbeat peaks and treat the ensemble average of the five waveforms as the representative. We demonstrate the representative waveforms of each axial acceleration in Fig. 5.3.

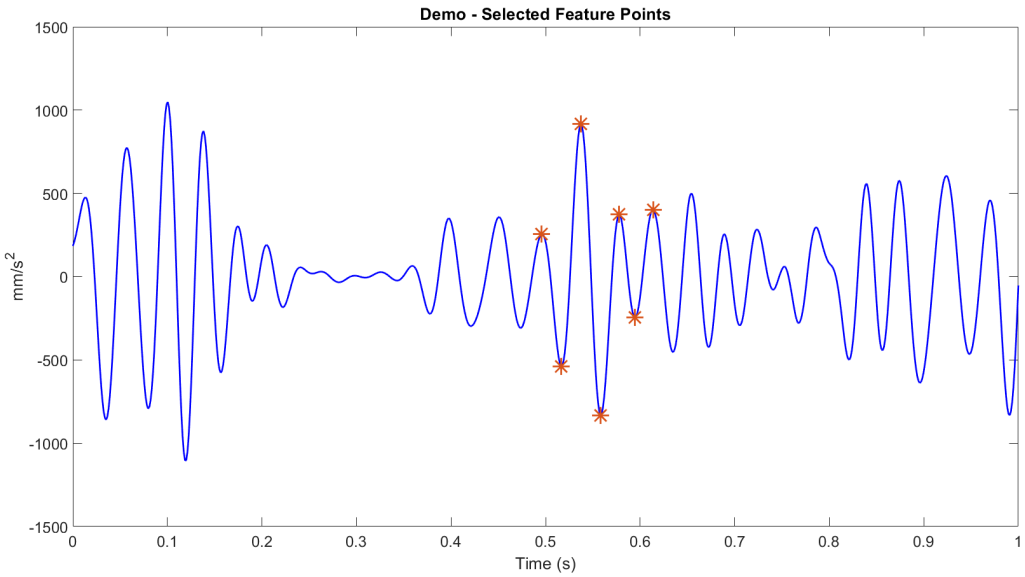

Figure 5.4: Illustration of the selected fiducial points. The candidate features are the temporal duration and magnitude ratio between each two fiducial points.

After generating the representations, we search the peaks and valleys close to the heartbeat peak and specify them as the fiducial points. Next, we empirically select seven fiducial points as illustrated in Fig. 5.4. Such selection strategy is based on the physiology of SCG/BCG curves, which usually contain the fiducial points H, I, J, K, L, M, N waves [60]. The heartbeat peak is chosen along with the preceding valley and peak and the two succeeding ones.

Last, we construct the feature space using the time interval and magnitude ratio between each pair of the fiducial points. Let's denote the time and the magnitude of the i^{th} and the j^{th} fiducial points

as t_i, t_j and a_i, a_j. Then, we define our timing feature space as $t_j - t_i$ for all $j > i$, and we specify our magnitude feature space as $\frac{|a_i - a_j|}{M}$, where M is the largest magnitude of all pairs of fiducial points ($M := max(|a_i - a_j|) \forall i, j$). Given the fact that the acceleration magnitude varies drastically due to motions, we choose the magnitude ratio instead of the numerical value of the magnitude as our features.

5.3.4 Model Construction

We employ stepwise regression to build the proposed motion artifact resilient BP estimation model. Such model construction takes two steps to accomplish. Initially, we apply stepwise regression method to select the features that best estimate the BP for each dimensional acceleration. More specifically, only the accelerations from sitting activities are employed, and we construct two different models for systolic and diastolic blood pressures, respectively. Next, we utilize the ensemble of the chosen features from each acceleration together with the height and weight of the subjects as the predictors in the ultimate BP estimation model. Such BP estimation model is also established using stepwise regression and is regarded as the motion artifact resilient BP estimation model.

5.3.5 Performance Evaluation

We evaluate the model's performance by computing the difference errors (DE), mean absolute difference errors (MADE), and root-mean-square errors (RMSE). Furthermore, we conduct correlation analysis between the estimated and the measured BP.

For estimated BP in standing and walking activities, we compare the estimations with the averaged BP in the sitting activity through feeding the motion artifact resilient BP model with the standing and walking features.

5.4 Experiment Results

We showcase the competitiveness of the proposed blood pressure estimation models in Table 5.2, briefly discuss the DBP and SBP models subsequently, and last present the potential blood pressure monitoring system for human subjects during walking motion.

Table 5.2: Evaluation of the Proposed Acceleration-based BP Monitoring Technique

	Diastolic Pressure	
Approach	M $\pm$ STD, RMSE, MADE	Correlation
Ours - sitting	0.09 ± 4.10 , 3.93, 3.62	$r = 0.80$
Ours - standing	0.93 ± 4.53 , 4.51, 3.30	$r = 0.72$
Ours - walking	1.15 ± 4.47 , 4.50, 3.36	$r = 0.59$
Tri-axial SCG [20]	-0.02 ± 3.82 , 3.82, –	$r = 0.97$
BCG-based [60]	–, 5.7, –	$r = 0.80$
PTT-based [88]	0.9 ± 5.6, – , –	–
	Systolic Pressure	
Ours - sitting	-0.25 ± 5.45 , 5.17, 4.73	$r = 0.81$
Ours - standing	-0.36 ± 6.26 , 6.11, 4.98	$r = 0.72$
Ours - walking	-0.38 ± 6.67 , 6.51, 5.07	$r = 0.70$
Tri-axial SCG [20]	-0.59 ± 7.46 , 5.57, –	$r = 0.96$
BCG-based [60]	–, 7.3, –	$r = 0.78$
PTT-based [88]	0.6 ± 9.8, – , –	–
PTT-based [120]	2.8 ± 8.2, – , –	–

*Note: DE, RMSE, and MADE have units in mmHg; – means not reported.

5.4.1 Efficacy of the Diastolic Pressure Estimation Model

Comparing our sitting DBP estimation results with other state-of-the-art, we achieve satisfying results. More importantly, our model meets both the AAMI standard and British Hypertension Society protocol [80]. Judging from the DE, both the mean and STD are less than 5 mmHg; considering MADE,

the number 3.62 mmHg is smaller than 5 mmHg. The difference error distribution is displayed in Fig. 5.5. Furthermore, the proposed DBP monitoring method outperforms [88] in DE and [60] in RMSE. Concerning the correlation, our model displays high correlation ($r = 0.8$) as visualized in Fig. 5.6. Our correlation is the same as [60] but not as high as [20]. Nevertheless, our subject number is 19, which is at least twice more than the 8 subjects in [20]. This indicates that our model could be more reliable than Chang *et al.*'s [20].

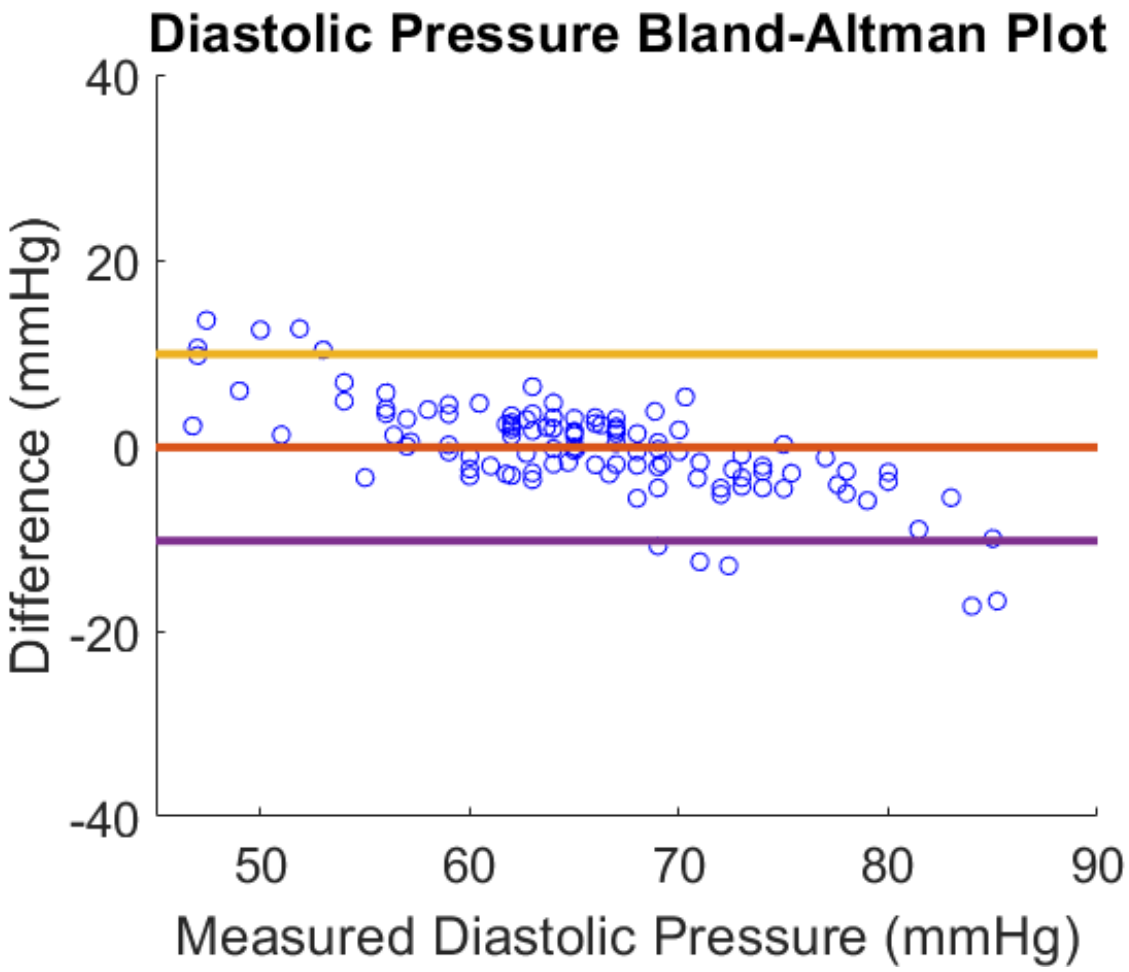

Figure 5.5: Bland-Altman plot of the estimated DBP errors.

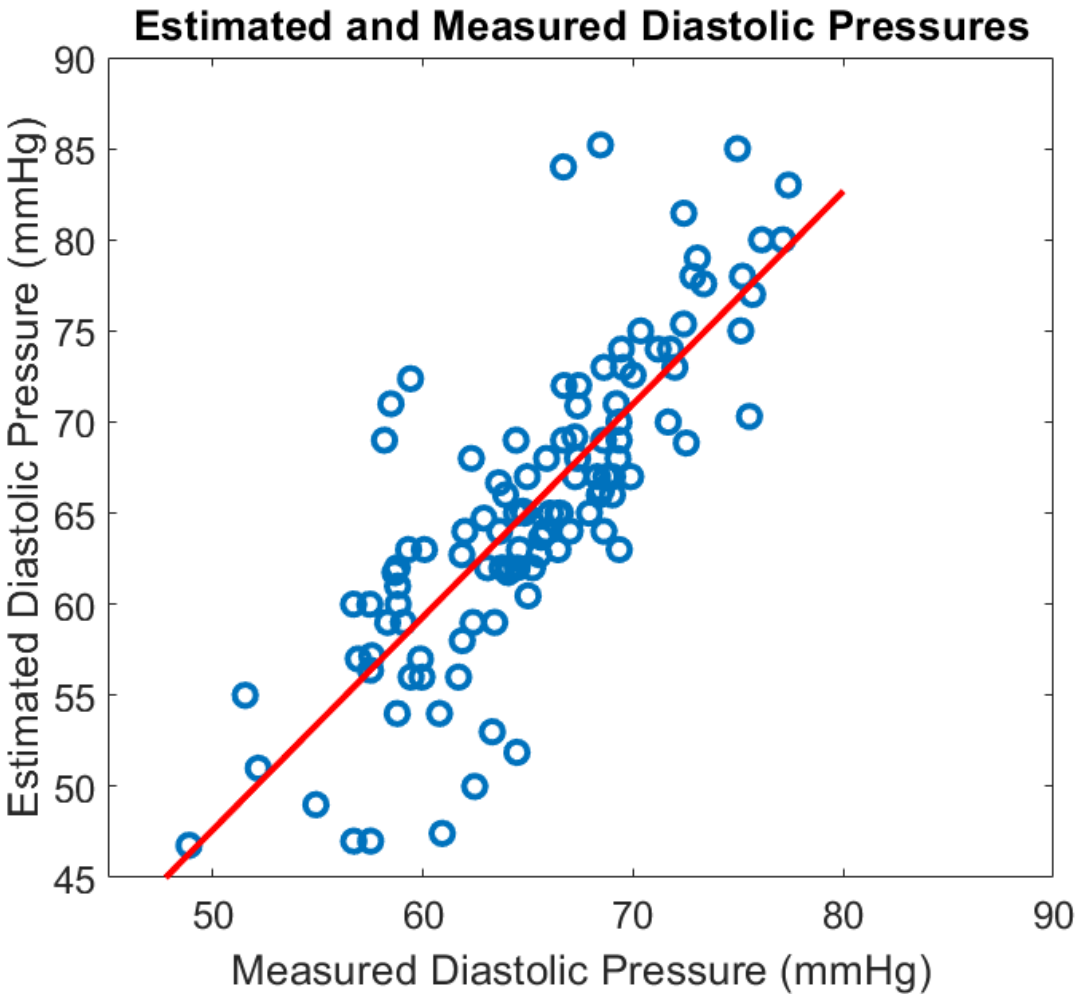

Figure 5.6: Demonstration of measured versus estimated DBP.

Six features are selected from the fusion sensors in the final DBP estimation model. They are height, time interval of H-L waves in left carotid horizontal acceleration, time interval of H-J waves in right hand dorsal-ventral acceleration, time interval of J-K waves in right hand dorsal-ventral acceleration, time interval of L-M waves in sternum horizontal acceleration, and magnitude ratio of M-N waves in sternum horizontal acceleration. The linear combinations of the six aforementioned features compose the best DBP estimation model in this study.

5.4.2 Efficacy of the Systolic Pressure Estimation Model

Judging the performance of the sitting SBP estimation models, we accomplish meeting both the AAMI standard and British Hypertension Society protocol [80]. For the DE, both the mean and STD are less than 8 mmHg; considering MADE, 4.73 mmHg is smaller than 5 mmHg. The difference error distribution is displayed in Fig. 5.7. Furthermore, the proposed SBP monitoring method beats [20] [88] [120] in DE and [20] [60] in RMSE. Concerning the correlation, our model displays high correlation ($r = 0.81$) as demonstrated in Fig. 5.8. Our correlation is slightly higher than [60] but not as high as [20], which might be caused by different human subject numbers.

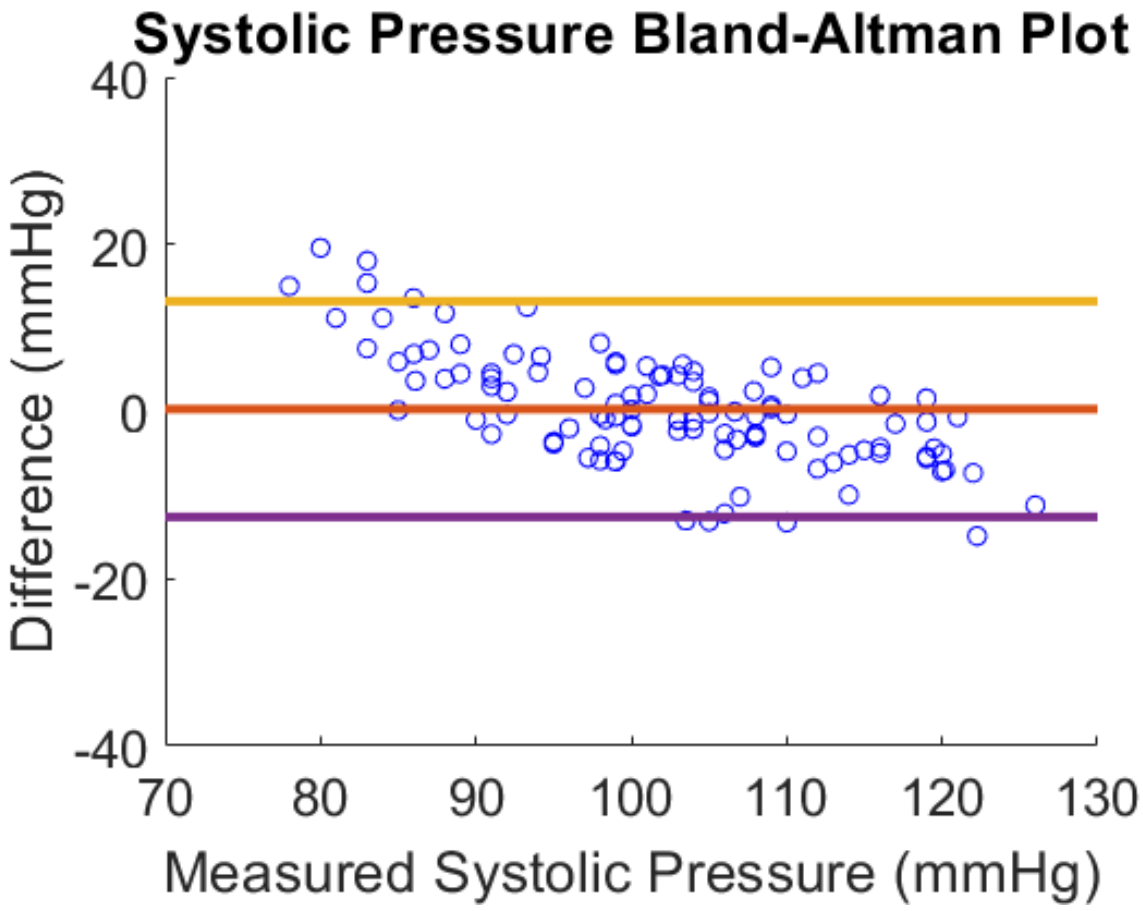

Figure 5.7: Bland-Altman plot of the estimated SBP errors.

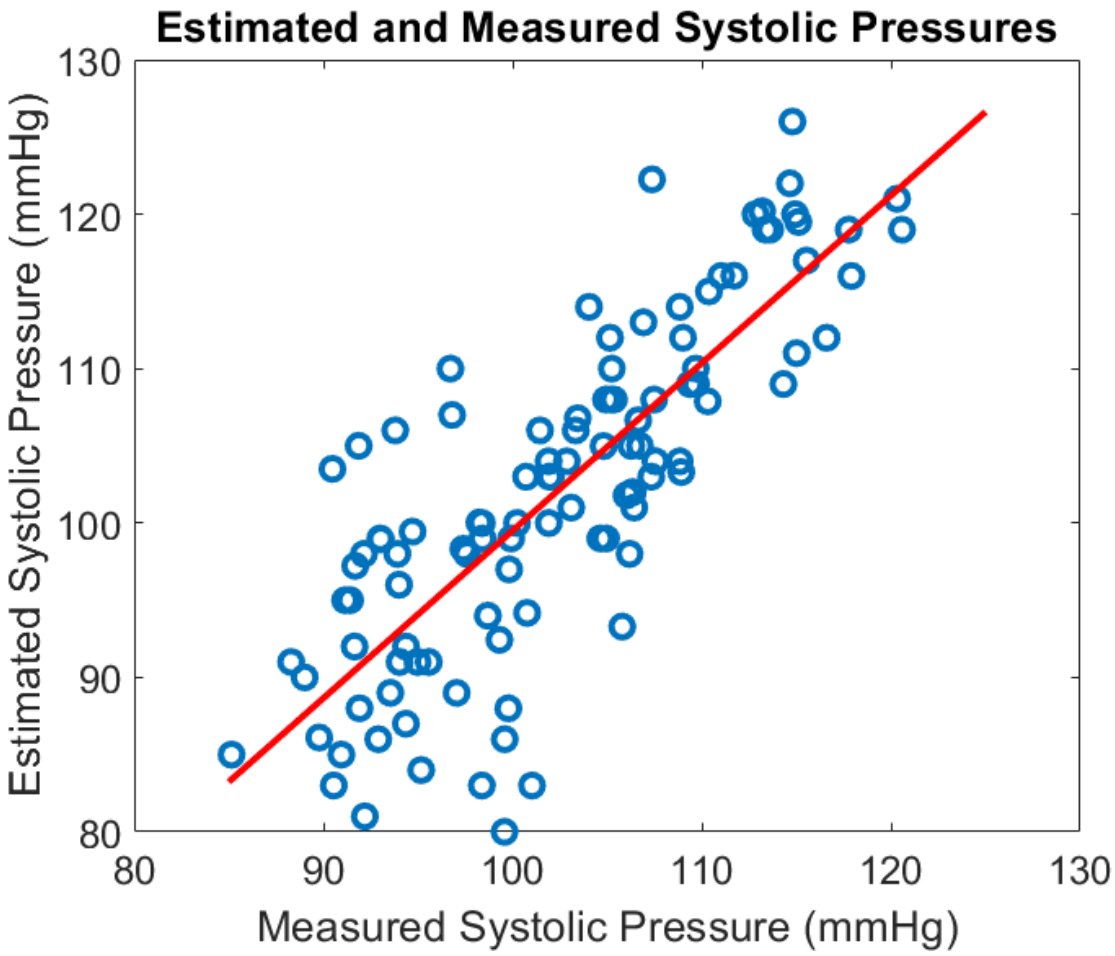

Figure 5.8: Demonstration of measured versus estimated SBP.

Five features are chosen from the fusion sensors in the final SBP estimation model. They are height, time interval of K-L waves in sternum horizontal acceleration, time interval of H-L waves in heart horizontal acceleration, time interval of H-J waves in left carotid horizontal acceleration, and time interval of K-M waves in left carotid dorsal-ventral acceleration. The linear combinations of these five features build the best SBP estimation model.

5.4.3 Potential of Motion Artifact Resilient Blood Pressure Monitoring

We demonstrate the promising results of motion artifact resilient BP estimation models in Table 5.2, Fig. 5.9 and Fig. 5.10. Based on the comparable DE, RMSE, and MADE in standing and walking activities, we could reasonably deduce that robust features have been employed to establish the BP monitoring systems. From the figures, we can clearly observe the logical trends of the BP. Participants with high BP in sitting also have high BP in standing and walking, and vice versa. Future work is encouraged to discover the association between the underlying physiology and the selected robust features.

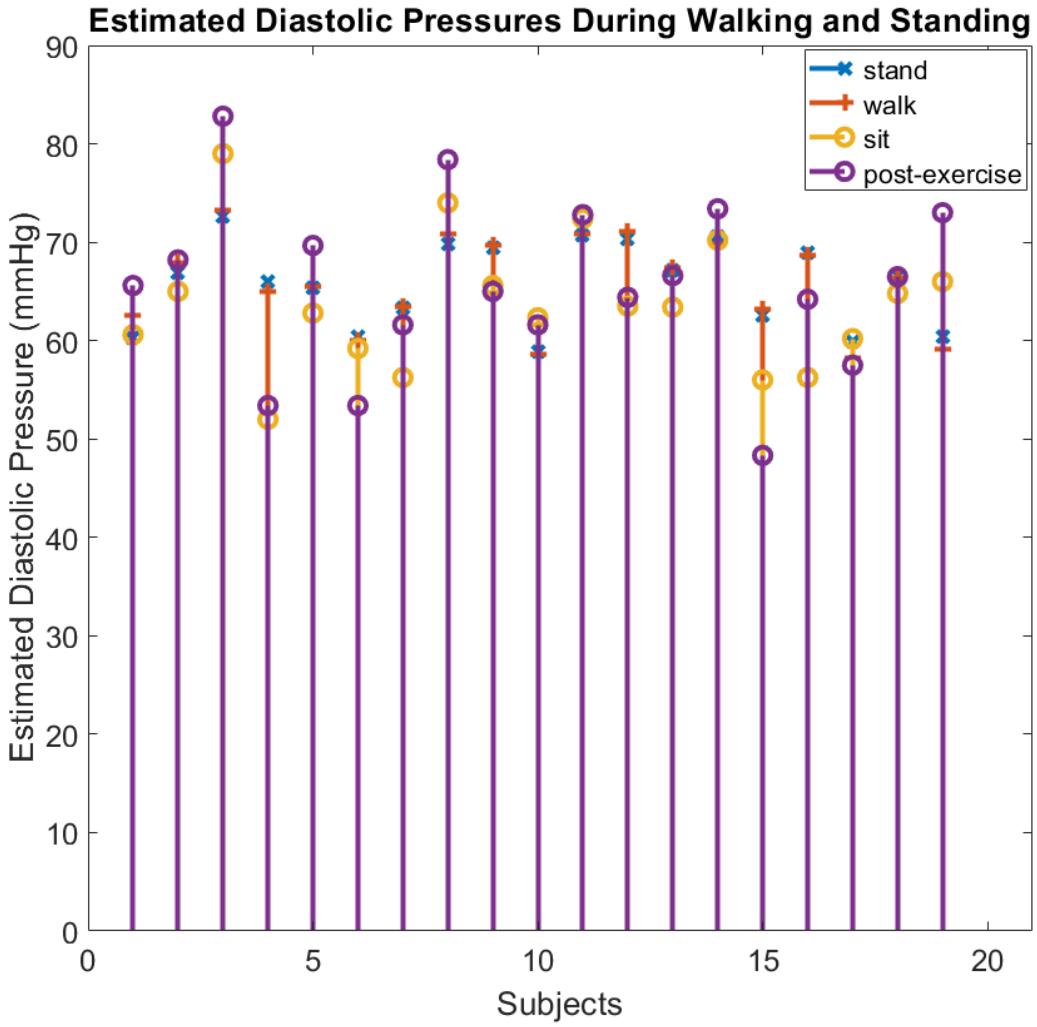

Figure 5.9: Demonstration of estimated DBP during motions.

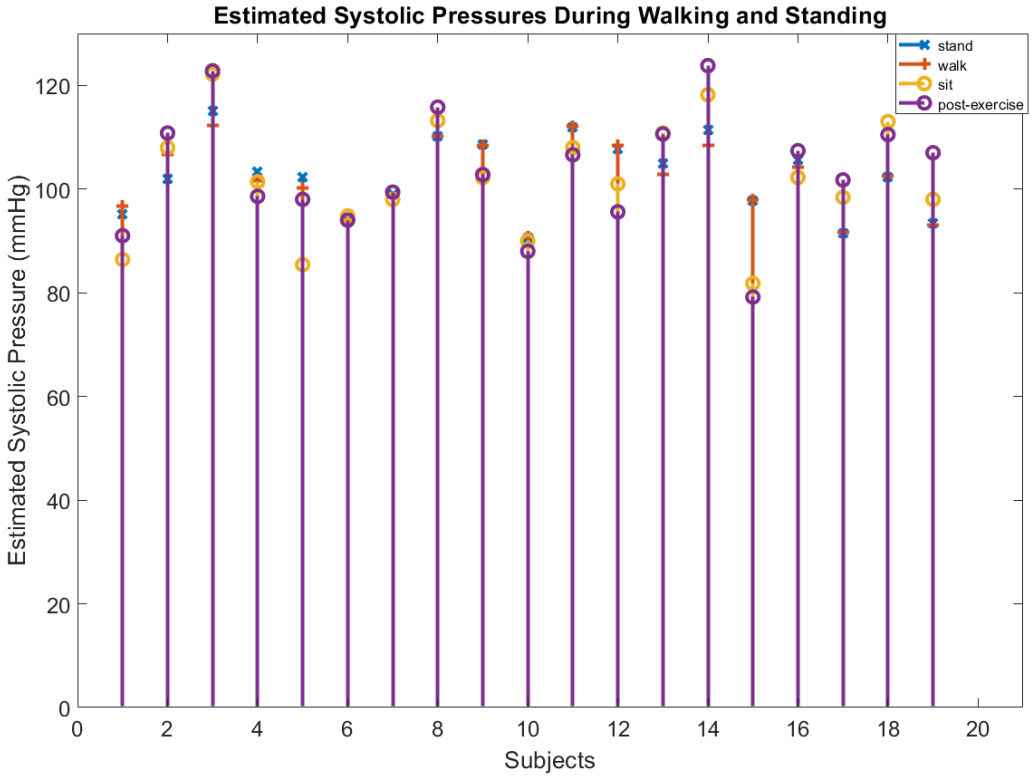

Figure 5.10: Demonstration of estimated SBP during motions.

5.5 Conclusions

We present a motion artifact resilient monitoring system for both systolic and diastolic blood pressures. The model fulfills both the AAMI standard and British Hypertension Society protocol. Moreover, we demonstrate that the devised approach is low-cost and convenient. Based on the promising results, we suggest applying the proposed technique in medical usage such as hypertension monitoring and blood pressure variation quantification for targeted diseases.

5.6 Acknowledgments

Chapter 5 contains a reprint of P.-Y. Hsu, P.-H. Hsu, H.-L. Liu, K.-Y. Lin, and T.-H. Lee, "Motion Artifact Resilient Cuff-Less Blood Pressure Monitoring Using a Fusion of Multi-Dimensional Seismocardiograms", *Annual International Conference of the IEEE Engineering in Medicine and Biology Society (EMBC)*, 2021.

I would like to thank my coauthors Po-Han Hsu, Tsung-Han Lee, Kuan-Yu Lin, and Hsin-Li Liu for their help on the internal review board documentation and insightful suggestions on our published work.

Chapter 6

Conclusion and Future Directions

This dissertation presents several promising techniques for the emerging challenges in computing cardiology. The analyzed problems address the latest trend projected by the research community of biomedical engineering and computational cardiology.

Chapter 2 presents two different methodologies for ECG heartbeat detection and one for SCG. We propose leveraging the physiological information from the ECG waveform to achieve the state-of-the-art performance. Moreover, we develop a novel ECG heartbeat visualization tool, *Star-ECG*, which enables the non-experts to easily capture the heartbeat, heart rate, and heart rate variability. For SCG, we devise a signal processing strategy to denoise SCG and a cardiac waveform-based heartbeat detection algorithm. We show that our algorithm performs competitively without requiring the individual to take SCG measurement in a supine position.

Chapter 3 provides three ECG arrhythmia classification programs, two for single lead and one for 12-lead ECG. We demonstrate incorporating the biologically interpretable features into the machine learning models can not only accomplish state of the art performance but also encourage the cardiologists to deploy the developed programs in clinic practice.

Chapter 4 explores leveraging the cardiac signal biometrics. We investigate both the electrical and mechanical heart-induced signals to serve as biometric authentication systems. Our results indicate that combining cardiac signal processing methods together with the machine learning techniques can potentially fulfill the challenges.

Chapter 5 proposes a motion artifact resilient cuff-less blood pressure monitoring technology. We demonstrate the efficacy of our blood pressure monitoring technique on 20 healthy individuals, and such technique also fulfills the AAMI standard of a commercial blood pressure monitor.

Looking beyond this dissertation, future directions and ongoing works include the following.

- **Integration of Expert Auxiliary:** The fully automated programs may accelerate early diagnosis of cardiovascular diseases. Nevertheless, a system that is able to handle experts' intervention can further improve the healthcare environment.

- **Correlation between Cardiac Signal and Body Information:** The proposed solutions rely heavily on the heart-induced signals, and considering other body information such as organs' well-functioning and daily routine can further enhance the power of the models.

- **Advanced Sensor Technology:** With the thrive in sensor technology, wearable sensors have come into various appearances with lower cost. This potentially suggests advantageous methodologies to be derived from conducting experiments with multi-modal sensors and different sensor placements.

Bibliography

[1] U. R. Acharya, P. S. Bhat, and U. C. Niranjan, "Comprehensive visualization of cardiac health using electrocardiograms", *Computers in biology and medicine 32, no. 1*, 2002, pp. 49-54.

[2] U. R. Acharya, S. L. Oh, Y. Hagiwara, J. H. Tan, M. Adam, A. Gertych, and R. S. Tan, "A deep convolutional neural network model to classify heartbeats", *Computers in biology and medicine 89*, 2017, pp. 389-396.

[3] R. J. Adams, "Improving health outcomes with better patient understanding and education", *Risk management and healthcare policy, vol. 3*, 2010, pp. 61.

[4] P. S. Addison, "Wavelet transforms and the ECG: a review", *Physiological Measurement 26, no. 5*, 2005, pp. 155.

[5] A. J. Adler, D. Prabhakaran, P. Bovet, D. S. Kazi, G. Mancia, V. Mungal-Singh, and N. Poulter, "Reducing cardiovascular mortality through prevention and management of raised blood pressure", *Global Heart 10, no. 2*, 2015, pp. 111-122.

[6] Er. A. P. Alday, A. Gu, A. J. Shah, C. Robichaux, A.-K. I. Wong, C. Liu, F. Liu, A.B. Rad, A. Elola, S. Seyedi, and Q. Li, "Classification of 12-lead ecgs: the physionet/computing in cardiology challenge 2020", *Physiological Measurement 41, no. 12*, 2020, pp. 124003.

[7] J. Allen and A. Murray, "Assessing ECG signal quality on a coronary care unit", *Physiological Measurement 17, no. 4*, 1996, pp. 249.

[8] B. S. Alpert, D. Quinn, and D. Gallick, "Oscillometric blood pressure: a review for clinicians." *Journal of the American Society of Hypertension 8, no. 12*, 2014, pp. 930-938.

[9] American Heart Association and others, "Heart Disease, stroke and research statistics at-a-glance" author=American Heart Association and others, *Internet*, 2015.

[10] Association for the Advancement of Medical Instrumentation, "Testing and reporting performance results of cardiac rhythm and ST segment measurement algorithms", *ANSI/AAMI EC38*, 1998.

[11] E. J. Benjamin, P. Muntner, A. Alonso, M. S. Bittencourt, C. W. Callaway, A. P. Carson, and A. M. Chamberlain, "Heart disease and stroke statistics—2019 update: a report from the American Heart Association", *Circulation 139, no. 10*, 2019, pp. 56-528.

[12] J. L. Bentley, "Multidimensional binary search trees used for associative searching", *Communications of the ACM 18, no. 9*, 1975, pp. 509-517.

[13] L. Biel, O. Pettersson, L. Philipson, and P. Wide, "ECG analysis: a new approach in human identification", *IEEE Transactions on Instrumentation and Measurement 50, no. 3*, 2001, pp. 808-812.

[14] D. E. Bloom, E. Cafiero, E. Jané-Llopis, S. Abrahams-Gessel, L. R. Bloom, S. Fathima, A. B. Feigl, "The global economic burden of noncommunicable diseases", *Program on the Global Demography of Aging No. 8712.* , 2012.

[15] A. A. Bui, Z. Yu, and F. M. Bui, "A biometric modality based on the seismocardiogram (SCG)", *IEEE International Conference and Workshop on Computing and Communication (IEMCON)*, 2015, pp. 1-7.

[16] Y.-H. Byeon and K.-C. Kwak, "Pre-configured deep convolutional neural networks with various time-frequency representations for biometrics from ECG signals", *Applied Sciences 9, no. 22*, 2019, pp. 4810.

[17] Y.-H. Byeon, S.-B. Pan, and K.-C. Kwak, "Intelligent deep models based on scalograms of electrocardiogram signals for biometrics", *Sensors 19, no. 4*, 2019, pp. 935.

[18] C. Carreiras, A. Lourenço, H. Silva, A. Fred, and R. Ferreira, "Evaluating template uniqueness in ECG biometrics", *Springer Informatics in Control, Automation and Robotics*, 2016, pp. 111-123.

[19] H. L. Chan, G. U. Chen, M. A. Lin, and S. C. Fang, "Heartbeat detection using energy thresholding and template match", *Annual International Conference of the IEEE Engineering in Medicine and Biology Society (EMBC)*, 2006, pp. 6668-6670.

[20] E. Chang, C.-K. Cheng, A. Gupta, P.-H. Hsu, P.-Y. Hsu*, H.-L. Liu, A. Moffitt, A. Ren, I. Tsaur, and S. Wang, "Cuff-Less Blood Pressure Monitoring with a 3-Axis Accelerometer", *Annual International Conference of the IEEE Engineering in Medicine and Biology Society (EMBC)*, 2019, pp. 6834-6837.

[21] Y. Chen and W. Chen, "Finger ECG based two-phase authentication using 1D convolutional neural networks", *Annual International Conference of the IEEE Engineering in Medicine and Biology Society (EMBC)*, 2018, pp. 336-339.

[22] I. I. Christov, "Real time electrocardiogram QRS detection using combined adaptive threshold" *Biomedical engineering online 3, no. 1*, 2004, pp. 1-9.

[23] C. Crema, A. Depari, A. Flammini, and A. Vezzoli, "Efficient R-peak detection algorithm for real-time analysis of ECG in portable devices", *IEEE Sensors Applications Symposium*, 2016, pp. 1-6.

[24] Y. D'Mello, J. Skoric, S. Xu, P. J. Roche, M. Lortie, S. Gagnon, and D. V. Plant, "Real-time cardiac beat detection and heart rate monitoring from combined seismocardiography and gyrocardiography", *Sensors 19, no. 16*, 2019, pp. 3472.

[25] P. De Chazal, M. O'Dwyer, and R. B. Reilly, "Automatic classification of heartbeats using ECG morphology and heartbeat interval features", *IEEE Transactions on Biomedical Engineering 51, no. 7*, 2004, pp. 1196-1206.

[26] A. Dinh, “Design of a seismocardiography using tri-axial accelerometer embedded with electrocardiogram”, *Proc. of the world congress on engineering and computer science, vol. 2*, 2011, pp. 19-22.

[27] G. M. Drzewiecki, J. Melbin, and A. Noordergraaf, “DEFORMATIONAL FORCES IN ARTERIAL TONOMETRY”, 1984.

[28] EcgSoft, “Ecgsoft homewpage”, “http://www.ecg-soft.com/.”, 2008.

[29] M. Elgendi, M. Jonkman, and F. D. Boer, “Frequency Bands Effects on QRS Detection”, *BIOSIGNALS*, 2010, pp. 2002.

[30] J. Y. A. Foo and S. J. Wilson, “A computational system to optimise noise rejection in photoplethysmography signals during motion or poor perfusion states”, *Medical and Biological Engineering and Computing 44, no. 1*, 2006, pp. 140-145.

[31] E. Frank, “An accurate, clinically practical system for spatial vectorcardiography”, *Circulation 13, no. 5*, 1956, pp. 737-749.

[32] Y. Freund and L. Mason, “The alternating decision tree learning algorithm”, *ICML, vol. 99*, 1999, pp. 124-133.

[33] T. Fujii, M. Nakano, K. Yamashita, T. Konishi, S. Izumi, H. Kawaguchi, and M. Yoshimoto, “Noise-tolerant instantaneous heart rate and R-peak detection using short-term autocorrelation for wearable healthcare systems”, *Annual International Conference of the IEEE Engineering in Medicine and Biology Society (EMBC)*, 2013, pp. 7330-7333.

[34] M. A. García-González, A. Argelagós-Palau, M. Fernández-Chimeno, and J. Ramos-Castro, “A comparison of heartbeat detectors for the seismocardiogram”, *IEEE Computing In Cardiology Conference* 2013, pp. 461-464.

[35] N. Ghofrani and R. Bostani, “Reliable features for an ECG-based biometric system”, *Iranian Conference of Biomedical Engineering (ICBME)*, 2010, pp. 1-5.

[36] A. L. Goldberger, L. A. Amaral, L. Glass, J. M. Hausdorff, P. C. Ivanov, R. G. Mark, J. E. Mietus, G. B. Moody, C.-K. Peng, and H. E. Stanley, “PhysioBank, PhysioToolkit, and PhysioNet: components of a new research resource for complex physiologic signals”, *Circulation 101, no. 23*, 2000, pp. 215-220.

[37] I. Goodfellow, Y. Bengio, and A. Courville, “Deep learning”, *MIT press*, 2016.

[38] K. He, X. Zhang, S. Ren, and J. Sun, “Deep residual learning for image recognition”, *IEEE Proc. of the conference on computer vision and pattern recognition*, 2016, pp. 770-778.

[39] S. Hong, Y. Zhou, J. Shang, C. Xiao, and J. Sun, “Opportunities and challenges of deep learning methods for electrocardiogram data: A systematic review”, *Computers in Biology and Medicine 122*, 2020, pp. 103801.

[40] P.-Y. Hsu and C.-K. Cheng, “Arrhythmia classification using deep learning and machine learning with features extracted from waveform-based signal processing”, *Annual International Conference of the IEEE Engineering in Medicine and Biology Society (EMBC)*, 2020, pp. 292-295.

[41] P.-Y. Hsu and C.-K. Cheng, "R-peak Detection Using a Hybrid of Gaussian and Threshold Sensitivity", *Annual International Conference of the IEEE Engineering in Medicine and Biology Society (EMBC)*, 2020, pp. 4470-4474.

[42] P.-Y. Hsu, and C. Holtz, "A Comparison of Machine Learning Tools for Early Prediction of Sepsis from ICU Data", *IEEE Computing In Cardiology Conference*, 2020, pp. 1-4.

[43] P.-Y. Hsu, P.-H. Hsu, T.-H. Lee, and H.-L. Liu, "Multi-label Arrhythmia Classification From 12-Lead Electrocardiograms", *IEEE Computing In Cardiology Conference*, 2020, pp. 1-4.

[44] P.-Y. Hsu, P.-H. Hsu, T.-H. Lee, and H.-L. Liu, "Heart Rate and Respiratory Rate Monitoring Using Seismocardiography", *Annual International Conference of the IEEE Engineering in Medicine and Biology Society (EMBC)*, 2021.

[45] P.-Y. Hsu, P.-H. Hsu, T.-H. Lee, and H.-L. Liu, "Motion Artifact Resilient SCG-based Biometric Authentication Using Machine Learning", *Annual International Conference of the IEEE Engineering in Medicine and Biology Society (EMBC)*, 2021.

[46] P.-Y. Hsu, P.-H. Hsu, and H.-L. Liu, "Exploring Seismocardiogram Biometrics with Wavelet Transform", *IEEE International Conference on Pattern Recognition*, 2021, pp. 4450-4457.

[47] P.-Y. Hsu, P.-H. Hsu, and H.-L. Liu, "Fold Electrocardiogram Into a Fingerprint", *Proc. IEEE/CVF Conference on Computer Vision and Pattern Recognition Workshops*, 2020, pp. 828-829.

[48] P.-Y. Hsu, P.-H. Hsu, H.-L. Liu, C.-T. Lin, H.-T. Chou, Y.-F. Tseng, and T.-H. Lee, "Star-ECG: Visualization of Electrocardiograms for Arrhythmia and Heart Rate Variability", *Annual International Conference of the IEEE Engineering in Medicine and Biology Society (EMBC)*, 2021.

[49] P.-Y. Hsu, P.-H. Hsu, H.-L. Liu, K.-Y. Lin, and T.-H. Lee, "Motion Artifact Resilient Cuff-Less Blood Pressure Monitoring Using a Fusion of Multi-Dimensional Seismocardiograms", *Annual International Conference of the IEEE Engineering in Medicine and Biology Society (EMBC)*, 2021.

[50] M. Ichino and H. Yaguchi, "Generalized Minkowski metrics for mixed feature-type data analysis", *IEEE Transactions on Systems, Man, and Cybernetics 24, no. 4*, 1994, pp. 698-708.

[51] A. Illanes-Manriquez, R. Jiménez, G. Dinamarca, C. Jiménez, and E. Lecannelier, "Visualizing the electrocardiogram through orbital transform", *Annual International Conference of the IEEE Engineering in Medicine and Biology Society (EMBC)*, 2010, pp. 5290-5293.

[52] B. Imholz, W. Wieling, G. A. Montfrans, and K. H. Wesseling, "Fifteen years experience with finger arterial pressure monitoring: assessment of the technology." *Cardiovascular research 38, no. 3*, 1998, pp. 605-616.

[53] O. T. Inan, M. Etemadi, R. M. Wiard, L. Giovangrandi, and G. T. A. Kovacs, "Robust ballistocardiogram acquisition for home monitoring", *Physiological Measurement 30, no. 2*, 2009, pp. 169.

[54] O. T. Inan, P. Migeotte, K.-S. Park, M. Etemadi, K. Tavakolian, R. Casanella, J. Zanetti, "Ballistocardiography and seismocardiography: A review of recent advances." *IEEE journal of biomedical and health informatics 19, no. 4*, 2014, pp. 1414-1427.

[55] S. Jakob, I. Korhonen, E. Ruokonen, T. Virtanen, A. Kogan, and J. Takala, "Detection of artifacts in monitored trends in intensive care" *Computer methods and programs in biomedicine 63, no. 3*, 2000, pp. 203-209.

[56] P. Jevon, "An introduction to electrocardiogram monitoring", *Nursing in critical care, vol. 15, no. 1*, 2010, pp. 34–38.

[57] V. Kalidas and L. Tamil, "Real-time QRS detector using stationary wavelet transform for automated ECG analysis", *IEEE International Conference on Bioinformatics and Bioengineering (BIBE)*, 2017, pp. 457-461.

[58] M. V. Kamath, and E. L. Fallen, "Power spectral analysis of heart rate variability: a noninvasive signature of cardiac autonomic function", *Critical reviews in biomedical engineering 21, no. 3*, 1993, pp. 245-311.

[59] J. M. Keller, M. R. Gray, and J. A. Givens, "A fuzzy k-nearest neighbor algorithm", *IEEE Transactions on systems, man, and cybernetics 4*, 1985, pp. 580-585.

[60] C.-S. Kim, A. M. Carek, O. T. Inan, R. Mukkamala, and J.-O. Hahn, "Ballistocardiogram-based approach to cuffless blood pressure monitoring: Proof of concept and potential challenges", *IEEE Transactions on Biomedical Engineering 65, no. 11*, 2018, pp. 2384-2391.

[61] D. P. Kingma and J. Ba, "Adam: A method for stochastic optimization", *arXiv*, 2014, 1412.6980.

[62] P. Kligfield, L. S. Gettes, J. J. Bailey, R. Childers, B. J. Deal, E. W. Hancock, G. V. Herpen, "Recommendations for the standardization and interpretation of the electrocardiogram: part I: the electrocardiogram and its technology a scientific statement from the American Heart Association Electrocardiography and Arrhythmias Committee, Council on Clinical Cardiology; the American College of Cardiology Foundation; and the Heart Rhythm Society endorsed by the International Society for Computerized Electrocardiology", *Journal of the American College of Cardiology 49, no. 10*, 2007, pp. 1109-1127.

[63] T. Ko, "Multimodal biometric identification for large user population using fingerprint, face and iris recognition", *IEEE Applied Imagery and Pattern Recognition Workshop (AIPR)*, 2005, pp. 6.

[64] Krizhevsky, Alex, Ilya Sutskever, and Geoffrey E. Hinton. "Imagenet classification with deep convolutional neural networks." Advances in neural information processing systems 25 (2012): 1097-1105.

[65] N. Laplante, P. A. Laplante, and J. Voas, "Caring: An Undiscovered "Super-ility" of Smart Healthcare", *IEEE software 33, no. 6*, 2016, pp. 16-19.

[66] Y. LeCun, Y. Bengio, and G. Hinton, "Deep learning", *Nature 521, no. 7553*, 2015, pp. 436-444.

[67] R. Li, G. Yang, K. Wang, Y. Huang, F. Yuan, and Y. Yin, "Robust ECG biometrics using GNMF and sparse representation", *Pattern Recognition Letters 129*, 2020, pp. 70-76.

[68] A. Liaw and M. Wiener, "Classification and regression by randomForest", *R news 2, no. 3*, 2002, pp. 18-22.

[69] J. M. Lilly and S. C. Olhede, "Higher-order properties of analytic wavelets", *IEEE Transactions on Signal Processing 57, no. 1*, 2008, pp. 146-160.

[70] A. Lourenço, H. Silva, P. Leite, R. Lourenço, and A. L. Fred, "Real Time Electrocardiogram Segmentation for Finger based ECG Biometrics", *Biosignals*, 2012, pp. 49-54.

[71] T. S. Lugovaya, Tatiana S, "Biometric human identification based on ECG", *PhysioNet*, 2005.

[72] H. M. Lynn, S. B. Pan, and P. Kim, "A deep bidirectional GRU network model for biometric electrocardiogram classification based on recurrent neural networks", *IEEE Access 7*, 2019, pp. 145395-145405.

[73] F. Magrabi, N. H. Lovell, and B. G. Celler, "A web-based approach for electrocardiogram monitoring in the home", *International Journal of Medical Informatics 54, no. 2*, 1999, pp. 145-153.

[74] J. Malmivuo and R. Plonsey, "Bioelectromagnetism: principles and applications of bioelectric and biomagnetic fields", *Oxford University Press, USA*, 1995.

[75] R. J. Martis, U. R. Acharya, and H. Adeli, "Current methods in electrocardiogram characterization", *Computers in biology and medicine 48*, 2014, pp. 133-149.

[76] R. J. Martis, U. R. Acharya, C. M. Lim, K. M. Mandana, A. K. Ray, and C. Chakraborty, "Application of higher order cumulant features for cardiac health diagnosis using ECG signals." *International journal of neural systems 23, no. 04*, 2013, pp. 1350014.

[77] P. E. McSharry, G. D. Clifford, L. Tarassenko, and Leonard A. Smith, "A dynamical model for generating synthetic electrocardiogram signals", *IEEE Transactions on Biomedical Engineering 50, no. 3*, 2003, pp. 289-294.

[78] M. Merone, P. Soda, M. Sansone, and C. Sansone, "ECG databases for biometric systems: A systematic review", *Expert Systems with Applications 67*, 2017, pp. 189-202.

[79] G. B. Moody and R. G. Mark, "The impact of the MIT-BIH arrhythmia database", *IEEE Engineering in Medicine and Biology Magazine 20, no. 3*, 2001, pp. 45-50.

[80] E. O'brien, B. Waeber, G. Parati, J. Staessen, and M. G. Myers, "Blood pressure measuring devices: recommendations of the European Society of Hypertension", *BMJ 322, no. 7285*, 2001, pp. 531-536.

[81] I. Odinaka, P.-H. Lai, A. D. Kaplan, J. A. O'Sullivan, E. J. Sirevaag, and J. W. Rohrbaugh, "ECG biometric recognition: A comparative analysis", *IEEE Transactions on Information Forensics and Security 7, no. 6*, 2012, pp. 1812-1824.

[82] M. Oefinger, W. Zong, M. Krieger, and R. G. Mark, "An interactive web-based tool for multiscale physiological data visualization", *IEEE Computing In Cardiology Conference*, 2004, pp. 569-571.

[83] J. Pan and W. J. Tompkins, "A real-time QRS detection algorithm", *IEEE Transactions on Biomedical Engineering 3*, 1985, pp. 230-236.

[84] K. Pandia, S. Ravindran, R. Cole, G. Kovacs, and L. Giovangrandi, "Motion artifact cancellation to obtain heart sounds from a single chest-worn accelerometer", *IEEE International Conference on Acoustics, Speech and Signal Processing*, 2010, pp. 590-593.

[85] K. K. Patro and P. R. Kumar, "Effective feature extraction of ECG for biometric application", *Procedia computer science 115*, 2017, pp. 296-306.

[86] D. Perloff, C. Grim, J. Flack, E. D. Frohlich, M. Hill, M. McDonald, and B. Z. Morgenstern, "Human blood pressure determination by sphygmomanometry", *Circulation 88, no. 5*, 1993, pp. 2460-2470.

[87] J. R. Pinto, J. S. Cardoso, and A. Lourenço. "Evolution, current challenges, and future possibilities in ECG biometrics", *IEEE Access 6*, 2018, pp. 34746-34776.

[88] C. C. Y. Poon and Y. T. Zhang. "Cuff-less and noninvasive measurements of arterial blood pressure by pulse transit time", *Annual International Conference of the IEEE Engineering in Medicine and Biology Society (EMBC)*, 2006, pp. 5877-5880.

[89] B. Porr and L. Howell, "R-peak detector stress test with a new noisy ECG database reveals significant performance differences amongst popular detectors", *BioRxiv*, 2019, 722397.

[90] P. Rajpurkar, A. Y. Hannun, M. Haghpanahi, C. Bourn, and A. Y. Ng, "Cardiologist-level arrhythmia detection with convolutional neural networks", *arXiv*, 2017, 1707.01836.

[91] A. Ranjan, "Permanence of ecg biometric: Experiments using convolutional neural networks", *IEEE International Conference on Biometrics (ICB)*, 2019, pp. 1-6.

[92] I. Rish, "An empirical study of the naive Bayes classifier", *IJCAI workshop on empirical methods in artificial intelligence, vol. 3, no. 22*, 2001, pp. 41-46.

[93] P. Rubel, B. Ayad, J. L. Willems, J. H. Van Bemmel, and C. Zywietz, "The true boundary recognition power of multidimensional detection functions. An optimal comparison", *North-Holland Pub. Comp.*, 1986, pp. 97-103.

[94] S. I. Safie, J. J. Soraghan, and L. Petropoulakis, "ECG biometric authentication using Pulse Active Width (PAW)", *IEEE workshop on biometric measurements and systems for security and medical applications (BIOMS)*, 2011, pp. 1-6.

[95] R. Salloum and C.-C. J. Kuo, "ECG-based biometrics using recurrent neural networks", *IEEE International Conference on Acoustics, Speech and Signal Processing (ICASSP)*, 2017, pp. 2062-2066.

[96] W. Sandham, D. Hamilton, A. Fisher, W. Xu, and M. Conway, "Multiresolution wavelet decomposition of the seismocardiogram", *IEEE transactions on signal processing 46, no. 9*, 1998, pp. 2541-2543.

[97] F. Shaffer and J. P. Ginsberg, "An overview of heart rate variability metrics and norms", *Frontiers in public health*, 2017, pp. 258.

[98] L. N. Sharma, R. K. Tripathy, and S. Dandapat, "Multiscale energy and eigenspace approach to detection and localization of myocardial infarction", *IEEE Transactions on Biomedical Engineering 62, no. 7*, 2015, pp. 1827-1837.

[99] T.-W. D. Shen, W. J. Tompkins, and Y. H. Hu, "Implementation of a one-lead ECG human identification system on a normal population", *Journal of Engineering and Computer Innovations 2, no. 1*, 2010, pp. 12-21.

[100] M. Stridh, L. Sornmo, C. J. Meurling, and S. B. Olsson, "Sequential characterization of atrial tachyarrhythmias based on ECG time-frequency analysis", *IEEE Transactions on Biomedical Engineering 51, no. 1*, 2004, pp. 100-114.

[101] J. A. Suykens and J. Vandewalle, "Least squares support vector machine classifiers", *Neural processing letters 9, no. 3*, 1999, pp. 293-300.

[102] M. J. Tadi, E. Lehtonen, T. Hurnanen, J. Koskinen, J. Eriksson, M. Pänkäälä, M. Teräs, and T. Koivisto, "A real-time approach for heart rate monitoring using a Hilbert transform in seismocardiograms", *Physiological Measurement 37, no. 11*, 2016, pp. 1885.

[103] A. Taebi, B. E. Solar, A. J. Bomar, R. H. Sandler, and H. A. Mansy, "Recent advances in seismocardiography", *Vibration 2, no. 1*, 2019, pp. 64-86.

[104] X. Tang and L. Shu, "Classification of electrocardiogram signals with RS and quantum neural networks", *International Journal of Multimedia and Ubiquitous Engineering 9, no. 2*, 2014, pp. 363-372.

[105] M. Tantawi, K. Revett, A.-B. Salem, and M. F. Tolba, "ECG based biometric recognition using wavelets and RBF neural network", *Proc. 7th Eur. Comput. Conf.(ECC)*, 2013, pp. 100-105.

[106] J. Wahlström, I. Skog, P. Händel, F. Khosrow-Khavar, K. Tavakolian, P. K. Stein, and A. Nehorai, "A hidden markov model for seismocardiography", *IEEE Transactions on Biomedical Engineering 64, no. 10*, 2017, pp. 2361-2372.

[107] D. Wang, Y. Si, W. Yang, G. Zhang, and T. Liu, "A novel heart rate robust method for short-term electrocardiogram biometric identification", *Applied Sciences 9, no. 1*, 2019, pp. 201.

[108] Y. Wang, F. Agrafioti, D. Hatzinakos, and K. N. Plataniotis, "Analysis of human electrocardiogram for biometric recognition", *EURASIP journal on Advances in Signal Processing 2008*, 2007, pp. 1-11.

[109] Z. Wang, A. C. Bovik, H. R. Sheikh, and E. P. Simoncelli, "Image quality assessment: from error visibility to structural similarity", *IEEE Transactions on image processing 13, no. 4*, 2004, pp. 600-612.

[110] W. D. Weaver, "Heart disease: a textbook of cardiovascular medicine", *Circulation 96, no. 7*, 1997, pp. 2465-2466.

[111] B. Wu, G. Yang, L. Yang, and Y. Yin, "Robust ecg biometrics using two-stage model", *IEEE International Conference on Pattern Recognition*, 2018, pp. 1062-1067.

[112] K. Xu, S. Guo, N. Cao, D. Gotz, A. Xu, H. Qu, Z. Yao, and Y. Chen, "Ecglens: Interactive visual exploration of large scale ecg data for arrhythmia detection", *Proc. of the CHI Conference on Human Factors in Computing Systems*, 2018, pp. 1-12.

[113] W. Yang, Y. Si, D. Wang, and B. Guo, "Automatic recognition of arrhythmia based on principal component analysis network and linear support vector machine", *Computers in biology and medicine 101*, 2018, pp. 22-32.

[114] C. Ye, M. T. Coimbra, and B. V. Kumar, "Investigation of human identification using two-lead electrocardiogram (ECG) signals", *IEEE International Conference on Biometrics: Theory, Applications and Systems (BTAS)*, 2010, pp. 1-8.

[115] C. Ye, B. V. Kumar, and M. T. Coimbra, "Combining general multi-class and specific two-class classifiers for improved customized ECG heartbeat classification", *IEEE International Conference on Pattern Recognition*, 2012, pp. 2428-2431.

[116] C. Ye, B. V. Kumar, and M. T. Coimbra, "Heartbeat classification using morphological and dynamic features of ECG signals" *IEEE Transactions on Biomedical Engineering 59, no. 10*, 2012, pp. 2930-2941.

[117] O. Yıldırım, P. Pławiak, R.-S. Tan, and U. R. Acharya, "Arrhythmia detection using deep convolutional neural network with long duration ECG signals", *Computers in biology and medicine 102*, 2018, pp. 411-420.

[118] Q. Zhang, D. Zhou, and X. Zeng, "HeartID: A multiresolution convolutional neural network for ECG-based biometric human identification in smart health applications", *IEEE Access 5*, 2017, pp. 11805-11816.

[119] Z. Zhao, Y. Zhang, Y. Deng, and X. Zhang, "ECG authentication system design incorporating a convolutional neural network and generalized S-Transformation", *Computers in biology and medicine 102*, 2018, pp. 168-179.

[120] Y.-L. Zheng, B. P. Yan, Y.-T. Zhang, and C. C. Y. Poon, "An armband wearable device for overnight and cuff-less blood pressure measurement." *IEEE Transactions on Biomedical Engineering 61, no. 7*, 2014, pp. 2179-2186.

[121] *AMPS*
`www.amps-llc.com/Home.php`, 2008.

[122] *OFFIS*
urlhttp://forum.dcmtk.org/2011, 2011.